UAB
Universitat Autònoma de Barcelona

Electrospray-based microelectromechanical systems for small spacecraft propulsion

Raúl Ramos-Tomás

INSTITUTO DE MICROELECTRÓNICA DE BARCELONA (IMB-CNM,CSIC)

IENAI SPACE

UNIVERSITAT AUTÒNOMA DE BARCELONA

Doctor of Philosophy in Electrical and Telecommunications Engineering

Electrospray-based microelectromechanical systems for small spacecraft propulsion

by

Raúl Ramos-Tomás

Author:

Raúl Ramos-Tomás

Directors:

Dr. Borja Sepúlveda

Dr. Javier Cruz

- June 2025 -

The following PhD thesis entitled **Electrospray-based microelectromechanical systems for small spacecraft propulsion** is presented by **Raúl Ramos-Tomás** as partial fulfillment of the requirements to obtain the title of industrial Doctor of Philosophy by the Universitat Autònoma de Barcelona and the Agència de Gestió d'Ajuts Universitaris i de Recerca (AGAUR) in the Electronics and Telecommunication Engineering PhD program.

This thesis was performed at the Instituto de Microelectrónica de Barcelona (IMB-CNM-CSIC) and IENAI SPACE, under the supervision of Dr. Borja Sepúlveda and Dr. Javier Cruz. Supervised by Dr. Maria Aránzazu Uranga del Monte.

Approved by:

Dr. Borja Sepúlveda as supervisor.

Dr. Javier Cruz as supervisor.

Dra. Maria Aránzazu Uranga del Monte as tutor.

A mis padres, Lumi y Carlos,

a mi hermano, Adán,

y a mi prometida, Maria.

Por vuestro apoyo incondicional a lo largo de este camino.

Raúl

Some people want it to happen,
some wish it would happen,
others make it happen.

Michael Jordan

One of the basic rules of the universe is that nothing is perfect.
Perfection simply doesn't exist.
Without imperfection, neither you nor I would exist.

Dr. Stephen Hawking

Only those who attempt the absurd can achieve the impossible.

Dr. Albert Einstein

Don't just learn, go and do something with it.

Dr. Richard P. Feynman

Abstract

The rapid emergence of CubeSats and nanosatellites has driven a paradigm shift in the space sector, enabling cost-effective missions for Earth observation, telecommunications, and scientific research. However, their compact size severely limits the integration of conventional propulsion systems, restricting autonomous maneuvering, collision avoidance, constellation management, and responsible end-of-life disposal. This propulsion gap is a major bottleneck for the operational maturity of small satellite platforms.

This doctoral thesis explores the development of an advanced propulsion solution tailored for these platforms: a silicon-based electrospray microelectromechanical system (MEMS) thruster. Electrospray propulsion stands out among electric propulsion technologies due to its intrinsic scalability, low power needs, high specific impulse, and minimal system complexity. It generates charged particle beams directly from ionic liquids using micro- or nanoscale emitters under high electric fields, removing the need for complex ionization subsystems and enabling high thrust-to-power ratios in a miniaturized form.

The core contribution of this research was the design, fabrication, and characterization of an externally wetted MEMS-based electrospray emitter array integrated into the ATHENA (Adaptable Thruster based on Electrospray for NAnosatellites) platform. Emitters were engineered as sharp microneedle arrays coated with dense silicon nanowires, fabricated using an innovative hybrid microfabrication process combining photolithography, reactive ion etching (RIE), and colloidal lithography. This design allows passive, capillary-driven propellant transport without internal channels, crucial for preventing clogging and ensuring long-term stability in space.

A comprehensive experimental analysis studied tip geometry, emission patterns, and efficiency, evaluating metrics such as emission current, angular beam distribution, and thrust-to-power efficiency. Results showed that extremely sharp microneedles (20º tip angle) caused high off-axis emission due to intense electric fields and premature ionic liq-

uid emission before reaching the tip. This was supported by theoretical analyses of emission trajectories from different points on the tip. Conversely, microneedles with larger tip angles (30–35º) achieved narrow Gaussian emission profiles with preferential forward emission and higher efficiency. Preliminary studies also revealed the impact of hydraulic resistance by adjusting nanostructure surface density, indicating improved emission patterns for higher resistances. Additionally, degradation mechanisms, including material erosion and electrochemical wear, were examined via scanning electron microscopy and long-duration emission tests. Protective coatings and emitter geometries were optimized to enhance operational lifetime and device robustness.

The results demonstrated the electrospray system's compatibility with CubeSat constraints: low power consumption and minimal volume. The ATHENA platform's modularity supports thrust scalability and adaptability to various mission profiles.

In conclusion, this thesis validates a technological pathway for integrating MEMS-based electrospray propulsion into next-generation small spacecraft. It bridges fundamental electrospray physics, advanced microfabrication, and practical in-space propulsion, advancing more autonomous, sustainable, and mission-capable nanosatellite platforms.

Resumen

La rápida aparición de los CubeSats y nanosatélites ha impulsado un cambio de paradigma en el sector espacial, permitiendo misiones económicas de observación terrestre, telecomunicaciones y experimentación científica. No obstante, su reducido tamaño limita la integración de sistemas de propulsión convencionales, restringiendo su capacidad para maniobras autónomas, evitación de colisiones, gestión de constelaciones y una disposición responsable al final de su vida útil. Esta carencia de propulsión representa hoy uno de los principales obstáculos para la madurez operativa de estas plataformas.

Esta tesis doctoral aborda el desarrollo de una solución de propulsión avanzada diseñada específicamente para estos satélites: un propulsor electrospray de silicio basado en tecnología MEMS (sistemas microelectromecánicos). Esta tecnología de propulsión eléctrica destaca por su escalabilidad, bajo consumo energético, elevado impulso específico y baja complejidad. Funciona generando haces de partículas cargadas directamente desde líquidos iónicos mediante emisores a micro o nanoescala sometidos a altos campos eléctricos, sin necesidad de subsistemas complejos de ionización, lo que permite obtener relaciones empuje/potencia elevadas en un formato compacto.

La principal contribución de esta investigación fue el diseño, fabricación y caracterización de una matriz de emisores electrospray de mojado externo, integrada en la plataforma ATHENA (Adaptable Thruster based on Electrospray for NAnosatellites). Los emisores se fabricaron como arreglos de microneedles afiladas recubiertas de nanohilos de silicio, mediante un proceso híbrido que combina fotolitografía, grabado iónico reactivo (RIE) y litografía coloidal. Esta arquitectura permite un transporte pasivo del propulsor por acción capilar, sin canales internos, lo cual previene obstrucciones y asegura estabilidad en el entorno espacial.

Se realizó un análisis experimental detallado de la geometría de las puntas y de los patrones de emisión, evaluando parámetros clave como la corriente de emisión, la dis-

tribución angular del haz y la eficiencia empuje/potencia. Se observó que microneedles con ángulos de punta muy agudos (20º) generaban emisiones desviadas, debido a campos eléctricos intensos y a la emisión prematura del líquido iónico. En cambio, microneedles con ángulos mayores (30–35º) mostraron una emisión más colimada y eficiente. También se identificó que una mayor resistencia hidráulica —lograda mediante el ajuste de la densidad de las nanoestructuras— mejora la calidad del patrón de emisión.

Adicionalmente, se estudiaron los mecanismos de degradación del sistema, como la erosión del material y el desgaste electroquímico, utilizando microscopía electrónica de barrido y pruebas prolongadas de emisión. Se implementaron recubrimientos protectores y ajustes en la geometría de los emisores para aumentar la durabilidad y robustez del dispositivo.

Los resultados demostraron que el sistema electrospray desarrollado es compatible con las exigencias de los CubeSats: requiere poca energía, ocupa poco volumen y permite modular el empuje según la misión. La arquitectura de ATHENA ofrece escalabilidad y adaptabilidad para distintas aplicaciones.

En conclusión, esta tesis presenta una solución tecnológica viable para integrar propulsión electrospray MEMS en futuras generaciones de nanosatélites, conectando los fundamentos físicos de la tecnología con su aplicación práctica en el espacio. Esta contribución representa un paso importante hacia plataformas más autónomas, sostenibles y funcionales en el ámbito de los pequeños satélites.

Acknowledgements

As I reach the conclusion of this doctoral thesis, I would like to express my deepest gratitude to everyone who has been part of this journey.

First and foremost, I want to sincerely thank my family for their unwavering support—not only during the good times, when I came home excited with new results, but also during the difficult moments, when frustration or discouragement took over. Thank you for always encouraging me and making this challenging path more bearable. Your unconditional love, patience, and motivation have been my greatest source of strength.

I am also profoundly grateful to my second family—my lifelong friends from my hometown—for making the bad days a little less bad and reminding me that life extends beyond work, salaries, or professional status. Your friendship has been a constant refuge, bringing laughter and perspective when I needed it most.

A heartfelt thank you as well to my office colleagues, who have become true friends beyond the professional environment. Thank you for sharing the daily experiences, frustrations, joys, and misfortunes with me, turning them into moments we could laugh about together. This journey would not have been the same without you.

I extend my sincere appreciation to my thesis advisors, Borja and Javi, for their guidance, trust, support, and the freedom they have given me throughout these years. Their expertise and dedication have been fundamental to the development of this research.

Finally, I want to thank myself—for taking on the challenge of pursuing a PhD, for believing in my own abilities, and for realizing that I am even more capable than I once thought. This journey has been a true rollercoaster, one that has allowed me to understand myself better, to recognize my strengths, and to reaffirm that, no matter what others may say, no one knows my potential better than I do.

Additionally, I would like to express my gratitude to the IMB-CNM staff for their support whenever I needed it, to IENAI SPACE for giving me the opportunity to pursue this PhD, and to AGAUR for the financial backing that made this research possible.

To all of you, thank you—this PhD belongs to you as much as it does to me!

Nomenclature

ALD	*Atomic Layer Deposition*
ATHENA	*Adaptable THruster based on Electrospray for NAnosatellites*
BCl_3	*Boron trichloride*
BOE	*Buffered Oxide Etchant*
C_4F_8	*Octafluorocyclobutane*
CAD	*Computer-Aided Design*
CF_4	*Tetrafluoromethane*
CHF_3	*Trifluoromethane*
Cl_2	*Chlorine*
COTS	*Commercial Off-The-Shelf*
CPD	*Critical Point Dryer*
DC	*Direct Current*
DRIE	*Deep Reactive Ion Etching*
EDX	*Energy Dispersive X-ray analysis*
EMI-BF_4	*1-Ethyl-3-methylimidazolium tetrafluoroborate*
EMI-DCA	*1-Ethyl-3-methylimidazolium dicyanamide*
EMI-$EtOSO_3$	*1-ethyl-3-methylimidazolium ethyl sulfate*
EMI-Im	*1-ethyl-3-methylimidazolium bis(triflouromethylsulfonyl)amide*
ESA	*European Space Agency*
FEEP	*Field Emission Electric Propulsion*
FIB	*Focused Ion Beam*
FWHM	*Full-Width Half Maximum*
GIT	*Gridded Ion Thrusters*
H_2O_2	*Hydrogen Peroxide*
H_2SO_4	*Sulfuric acid*
HCl	*Hydrochloric acid*
HF	*Hydrofluoric acid*
ICP	*Inductively Coupled Plasma*

ILs *Ionic Liquids*

IPA *2-Propanol*

IoT *Internet of Things*

KOH *Potassium Hydroxide*

MEMS *Microelectromechanical Systems*

MPD *Magneto-Plasma-Dynamics*

NASA *National Aeronautics and Space Administration*

NH_4OH *Ammonium hydroxide*

NWs *Nanowires*

PCB *Printed Circuit Board*

PDMS *Polydimethylsiloxane*

PECVD *Plasma Enhanced Chemical Vapor Deposition*

PIR *Pure Ionic Regime*

PMU *Propellant Management Unit*

PR *Photoresist*

PPTs *Pulsed Plasma Thrusters*

PVD *Physical Vapor Deposition*

RCA *Radio Corporation of America*

RF *Radio Frequency*

RIE *Reactive Ion Etching*

RT *Room Temperature*

SC *Standard Cleaning*

SEM *Scanning Electron Microscopy*

SF_6 *Sulfur hexafluoride*

Si_3N_4 *Silicon Nitride*

SiF_4 *Silicon tetrafluoride*

SiO_2 *Silicon Oxide*

SLM *Selective Laser Melting*

UHV *Ultra High Vaccum*

UV *Ultraviolet*

Contents

Chapter 1

1 Introduction

Throughout history, humanity's curiosity about space has served as a driving force for exploration and comprehension of the cosmos. From the ancient Mesopotamian and Egyptian civilizations, who utilized celestial bodies for navigation, to contemporary achievements such as capturing images of a black hole, our fascination motivated us to unveil the universe.

The progression of the scientific understanding of space has been closely intertwined to the development of instruments that expand our observational capabilities. Among these instruments, the astrolabe stands out as one of the earliest tools for determining the positions of the stars over the horizon. However, the advent of the telescope, notably championed by Galileo Galilei, represented a significant leap forward. Galileo's observations not only enriched astronomical knowledge but also provided evidence for the heliocentric model of the solar system. It marked a significant turning point in the history of astronomy, ushering in an era of optical exploration of celestial phenomena.
Over time, telescopes have undergone remarkable advancements in design, technology and functionality, enabling astronomers to delve deeper into the complexities of the universe.

Although telescopes enable unravelling certain details of the universe, their effectiveness was hindered by Earth's atmosphere. The emergence of rocket technologies revolutionized space exploration by enabling the deployment of payloads beyond Earth's atmosphere, including observation instruments. However, it was the launch of the Sputnik 1 in 1957 that truly inaugurated the age of space exploration, symbolizing humanity's first foray into the universe beyond our planet's confines.

In this introduction, the evolution from early satellites to contemporary CubeSats is explored, highlighting the necessity of on-board propulsion systems to mitigate inherent drawbacks in these spacecrafts. Furthermore, among the propulsion systems available, the case of the electric propulsion, specifically the electrospray propulsion, as a promis-

ing solution will be presented. Finally, the importance of employing specific technologies for electrospray thrusters development will be elucidated, providing a framework for the ensuing research discussion.

1.1 From large spacecrafts to CubeSats

The dawn of the space age can be traced back to the late 1950s and early 1960s, highlighted by the launches of satellites like the Soviet Union's Sputnik 1 and the American Explorer 1 [1, 2]. These pioneering satellites were not fully functional spacecraft but served as initial experiments to prove that objects could be successfully placed into orbit. In contrast to the spacecraft that succeeded, these early satellites were relatively limited in scale.

Historically, space missions have been characterized by heavily on large and sophisticated spacecraft. Such missions demanded extensive engineering teams, considerable financial resources, often provided by huge institutions such as NASA or ESA, long development times, and advanced infrastructure. They were designed for a variety of missions, minimizing the cost per kilogram of payload and to house multiple measurement instruments. However, this frequently resulted in interference among them, causing operational issues.

In the late 90s, the space industry experienced a paradigm shift. Alongside a peak in the mass of satellites launched [3], there was a growing interest in small spacecraft. Advances in technology made it possible to miniaturize satellites using low-cost and low-power Commercial Off-The-Shelf (COTS) components.

Figure 1: Satellite size classification.

This led to the standardization of the CubeSat, a unit measuring 10 cubic centimeters with

a mass around 1 kg [4–7], which directly resulted from this increasing interest. Initially, CubeSats were intended for educational purposes or scientific demonstrations that could be completed in a short period. As CubeSats became more advanced, they demonstrated their viability as cost-effective platforms with significant scientific and economic potential. Moreover, constellations of CubeSats can provide continuous global coverage, redundancy, and rapid response capabilities that are difficult to achieve with a single large spacecraft. This newfound utility drew the interest of smaller organizations. The versatility and affordability of CubeSats have made them an attractive technology, leading to a rapid increase in the number of small satellites launched in recent years (Fig. 2).

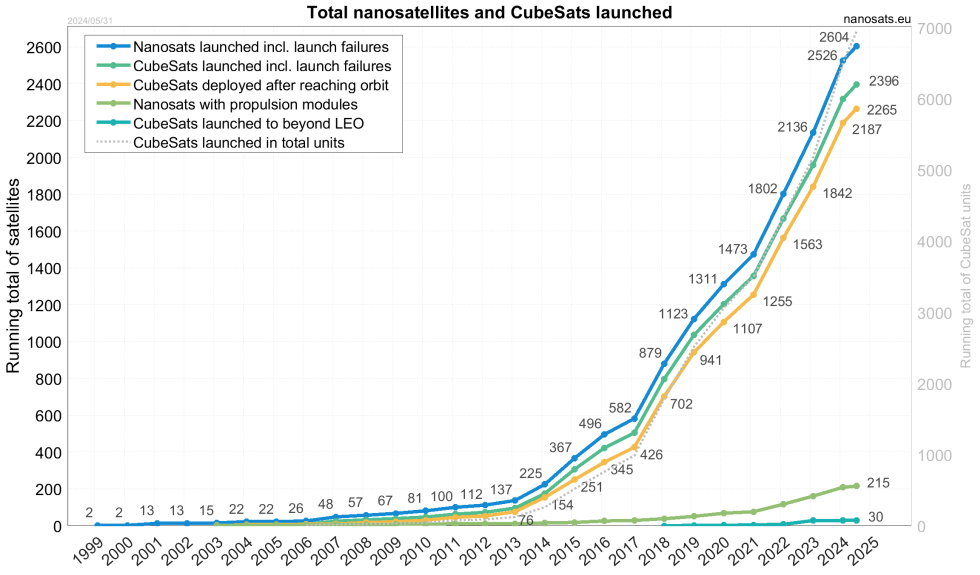

Figure 2: Total number of launched nanosatellites and CubeSats since the end of the 90s from Nanosats Database.

However, CubeSats also encounter significant challenges. Their compact size restricts their power, communication bandwidth, and payload capacity [8]. Additionally, their shorter operational lifespans, related with attitude control, and the risk of contributing to space debris are major concerns [9]. Many CubeSats lack propulsion systems, which are critical for maneuverability and deorbiting, thereby improving operational longevity and reducing space debris [10–12]. This absence limits their flexibility and potential applications, presenting a significant challenge for the future development of small satellite

technology. Ongoing advancements in CubeSat technology aim to address these issues, enhancing their capabilities and expanding their range of applications.
Despite these constraints, not all propulsion systems are suitable for use in small spacecraft. These systems must be optimized for low power consumption and compact size to be effective [12].

1.2 Basics on Space Propulsion

Propulsion systems can be highly complex, involving intricate calculations related to fluid dynamics and efficiency, among other factors. However, like many fundamental concepts in applied physics, propulsion is based on Newton's third law. When thrust is generated by expelling mass, also called propellant, the system accelerates in the opposite direction with minimal interaction due to the vacuum of space minimizing external forces. This expulsion of mass is known as thrust and is expressed as:

$$F = \frac{d}{dt}(mv) \tag{1.1}$$

Taking into account that the mass is expelled at a constant rate, we determine that $\dot{m} = -dm/dt$, and that the velocity at which it is ejected, called exhaust velocity, is v_e, we can rewrite as:

$$F = \dot{m}v_e \tag{1.2}$$

Considering that we are in vacuum, by conservation of momentum, we express the well-known classical rocket equation 1.3:

$$\frac{dp}{dt} = m\frac{dv}{dt} + v\frac{dm}{dt} + \frac{-dm}{dt}(v - v_e) = 0 \tag{1.3}$$

Isolating the terms the equation is simplified as equation 1.4:

$$\frac{dv}{v_e} = \frac{-dm}{m} \tag{1.4}$$

By integrating the equation terms 1.4, we obtain the well-known Tsiolkovsky rocket equation 1.6:

$$\int_0^{\Delta v} dv = -v_e \int_{m_0}^{m_f} \frac{dm}{m} \tag{1.5}$$

$$\frac{\Delta v}{v_e} = ln\left(\frac{m_0}{m_f}\right) \tag{1.6}$$

In Eq. 1.6, Δv term represents the total change in velocity that the rocket can achieve, m_0 is the initial mass including the entire mass of the rocket at the beginning of the propulsion, comprising both the rocket's structure and the total mass of the propellant, and m_f represents the final mass of the rocket after all the propellant has been consumed.

The properties for each space mission are unique depending on its main purposes. Therefore, Eq. 1.6 can be written in terms of the propellant required for a given Δv, resulting in Eq. 1.7. In this way, mission design and optimization is facilitated.

$$m_p = m_0\left(1 - e^{-\frac{\Delta v}{v_e}}\right) \tag{1.7}$$

Hence, it is clear that the exhaust velocity (v_e) significantly influences the efficiency of the propellant. The specific impulse (I_{sp}) measures this efficiency, as described by Eq. 1.8, in terms of the standard acceleration due to gravity, g_0.

$$I_{sp} = \frac{v_e}{g_0} \tag{1.8}$$

By isolating v_e term from Eq. 1.8 and substituting it into the mass ratio equation, 1.7, a

modified Tsiolkovsky rocket equation is derived as Eq. 1.9.

$$m_p = m_0 \left(1 - e^{-\frac{\Delta v}{I_{sp} g_0}}\right) \tag{1.9}$$

Equation 1.9 reveals that I_{sp} has a significant effect on the mass of a rocket system, particularly in how much propellant mass is required for a given mission. A higher I_{sp} means a more efficient engine, which translates to higher effective exhaust velocity as the exponent is reduced. Consequently, the initial mass m_0 decreases, meaning less propellant is needed.

Building on the previous result, the efficiency of the system is a key parameter to know the capacity to obtain a useful kinetic energy to propel the spacecraft through a power source. Propulsion efficiency (η_p) is defined in Eq. 1.10 as the ratio of the kinetic energy of the exhaust (E_k) and the power supplied by a source (P).

$$\eta_p = \frac{E_k}{P} = \frac{\frac{1}{2}\dot{m}_p v_e^2}{P} \tag{1.10}$$

The efficiency of a propulsion system is influenced by various factors, including the type of propellant, the design of the rocket nozzle, and the operational conditions of the engine. Propellants can vary widely in properties and define the mechanism that will supply a power to generate thrust.

1.2.1 Propulsion systems

Propulsion systems vary greatly based on the mechanism used to produce thrust [10–12], including chemical, nuclear, solar or electric. Chemical propulsion systems, generate thrust using chemical energy stored within propellant bonds. Through chemical reactions, energy is released by breaking those bonds. The reaction products generated are accelerated and produce thrust. These type of systems include: (i) solid propellants, which are straightforward and reliable but lack throttle control; (ii) liquid propellants, which offer higher efficiency and control at the cost of complexity; and (iii) hybrid propellants, which are safer than liquids systems but less efficient [13–16].

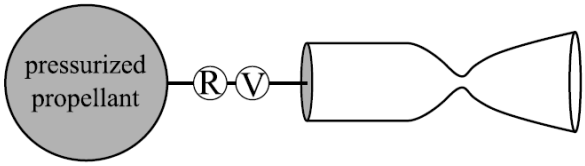

Figure 3: Chemical propulsion schematics [12].

Nuclear propulsion systems employ nuclear reactions to generate heat or electricity for thrust purposes. Nuclear thermal propulsion systems perform a high specific impulse and thrust despite the technological challenges that surround these systems. In the other hand, nuclear electric systems have a high efficiency but require a significant power and a complex technology [17–19].

In addition to conventional propulsion systems that generate thrust by accelerating products from reactions, novel propulsion model applying physical mechanisms through photons have emerged. Among those, solar sails and laser propulsion can be found. Solar sails employ the sunlight to generate thrust, which is an infinite power source. However, this technology produce very low thrust [20–22]. In the other hand, laser propulsion uses external beams to exert pressure in a sail, but requires high power laser technologies [23].

On the other hand, electric propulsion systems employ electrical energy to accelerate propellant ions. The devices designed and manufactured in this project belong to a specific type of electric propulsion systems, so they will be described more extensively in the following section.

1.3 Electric Propulsion

Although traditional propulsion systems are predominantly based on chemical propulsion, electric propulsion has emerged as a disruptive alternative technology due to its remarkable capabilities. Unlike chemical propulsion systems, electric propulsion systems obtain the necessary energy through an external source. The propellant is chosen exclusively for its mass and electric properties, and the particles are accelerated using applied electrical

power. Consequently, the thrust produced is limited by the available electrical power that the source can provide.
Despite this limitation, electric propulsion systems are extremely efficient. They can accelerate the propellant species to high exhaust velocities, resulting in higher I_{sp} values with respect to previous systems [12, 24]. This allows them to operate over a broad range of specific impulses without compromising system efficiency.

Since the supplied power is electrical, the acceleration of the propellant can be finely controlled. This contrasts with chemical thrusters, where chemical energy is fully converted into kinetic energy, with a significant portion lost as heat. Electric propulsion systems provide lower thrust over longer periods, which is ideal for gradual but precise changes in velocity. This continuous thrust capability enables spacecraft to perform fine adjustments and maintain optimal orbits with minimal propellant consumption. Efficient use of propellant directly correlates with the need for less propellant to achieve the desired Δv.

These properties make electric propulsion systems optimal for small spacecraft. The low power levels at which they can operate are compatible with those generated by small satellites. Additionally, the continuous use of small amounts of propellant makes them highly efficient without significantly impacting the satellite's payload. Furthermore, electric propulsion systems are highly scalable, meaning they can be designed to operate over a wide range of power levels. This scalability makes them suitable for small satellites, such as CubeSats, which typically have limited power budgets derived from small solar panels or batteries.

1.3.1 Types of electric propulsion systems

To fully understand the advantages of electric propulsion, it is crucial to know the different types of electric propulsion systems available. Each type employs a unique mechanism to ionize and accelerate the propellant, offering different performance characteristics suited to specific mission requirements. These systems can be classified as electrothermal, elec-

tromagnetic and electrostatic. [25].

Electrothermal systems utilize electrical energy to heat a propellant within a chamber. This heating process causes the propellant to expand into a gas, which can be either neutral or ionized. The gas then exits through a nozzle, converting thermal energy into kinetic energy to generate thrust [26]. Arcjets and resistojets are common types of electrothermal thrusters. In arcjet thrusters, a continuous electric current flows between two electrodes of opposite polarity, creating an electric arc that heats the propellant [27]. The temperatures achieved by the electric arc are significantly higher than those produced by a heating coil, resulting in a higher specific impulse compared to resistojets. Arcjets can achieve specific impulses 2 to 3 times greater than those of chemical thrusters. However, arcjets are often plagued by low efficiency and substantial heat losses, which can impact overall performance and the durability of thruster materials [28]. Resistojets, on the other hand, heat the propellant to high temperatures using electrical energy before releasing it under pressure [29]. The pressurized, heated propellant then expands through a converging-diverging nozzle, accelerating it to produce thrust. Both arcjets and resistojets face challenges related to energy losses in the form of heat, which can affect the materials used in the thrusters and the available power for propulsion.

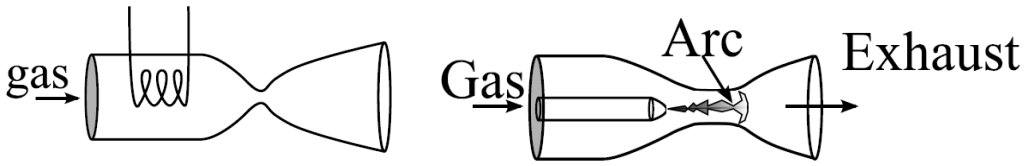

(a) Resistojet (b) Arcjet

Figure 4: Electrothermal systems schematics: a) resistojet thruster and b) arcjet thruster [12].

Electromagnetic thrusters use electromagnetic fields to ionize and accelerate the propellant, necessitating high power levels for operation [26]. This category includes pulsed plasma thrusters (PPTs) and magneto-plasma-dynamic (MPD) thrusters. Pulsed plasma thrusters generate a magnetic field between two electrodes situated in the exhaust nozzle.

Electric current pulses ignite the gas into a plasma, which is then expelled to produce thrust. MPD thrusters, considered the most powerful electric thrusters, generate a magnetic field within a coil [30]. Combined with an electric current, this setup induces a Lorentz force that directs and accelerates the plasma. Both PPT and MPD thrusters achieve high specific impulses, making them highly efficient in terms of propellant consumption. However, several drawbacks limit their application in satellite propulsion. These include high power requirements, material degradation from plasma interactions, system complexity, and lower overall efficiency compared to other types of thrusters.

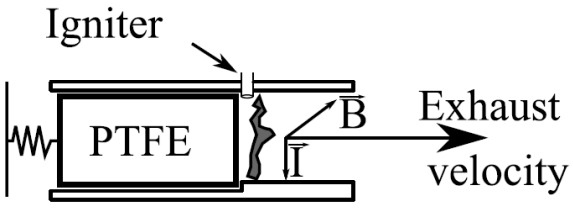

Figure 5: Electromagnetic systems schematics: Pulsed Plasma Thruster [12].

Electrostatic systems rely solely on electric power to ionize the propellant [26]. The resulting ions are then accelerated by the electric field created between two electrodes. Established systems in this category include Hall effect thrusters and Gridded Ion Thrusters (GIT), with newer technologies like Field Emission Electric Propulsion (FEEP) systems and electrospray systems also gaining recognition. Hall effect thrusters operate based on the Hall effect [31]. In these thrusters, the propellant is ionized and then accelerated to high velocities as it moves through an electric field within a channel, which is oriented perpendicular to a magnetic field. The primary function of the magnetic field is to direct the electrons and prevent them from spinning and shortening [32].

GIT systems generate ions by bombarding the propellant with an electron beam, which can be produced through direct current (DC), radio frequency (RF), or microwave methods [33]. The generated ions are then expelled through a series of grids with an applied potential difference. The ionization efficiency of these devices depends on the propellant and current used. The efficiency of Hall thrusters is generally lower than for GITs. They often produce higher thrust for a given power and require less demanding power supplies [32]. However, these systems face challenges such as the miniaturization of cath-

odes for electron supply and the difficulty in manufacturing components that are highly resistant to erosion.

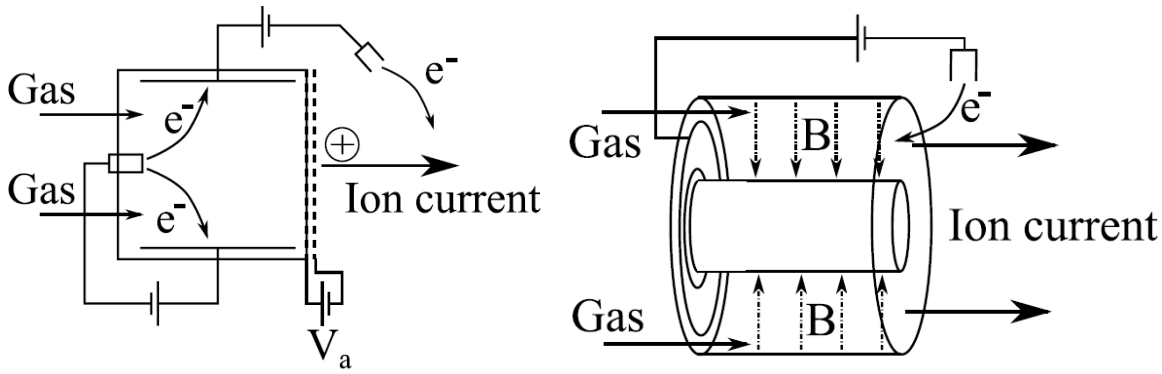

(a) Grided Ion (b) Hall

Figure 6: Electrostatic systems schematics: a) Grided Ion Thruster and b) Hall thruster [12].

FEEP and electrospray technologies share similar principles for accelerating generated species, relying on a constant electric field for this purpose. However, they differ in how they produce the charged particles. FEEP systems use liquid metals as propellant [34–36], whereas electrospray systems use ionic liquids [37]. Both technologies utilize sharp emitters to generate a strong electric field that deforms the liquid into what is known as a Taylor cone [38]. Once the electric field exceeds a certain threshold, the charged species are ejected. Due to the nature of the propellants used, these systems do not require ionization processes, making them particularly suitable for miniaturization.

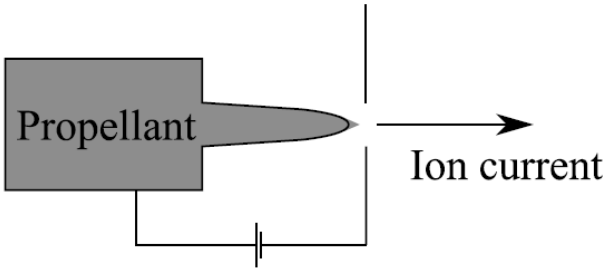

Figure 7: Electrostatic system schematics: Electrospray/FEEP [12].

1.3.2 Electrospray propulsion systems

Electrospray has emerged as a highly attractive technology in many fields, including ink-jet printing [39, 40], drug delivery [41], 3D printing [42], disinfection and air purification [43, 44], focused ion beam (FIB) and etching [45, 46], mass spectrometry [47], firefighting [48–50] or space propulsion [10–12], among others. Electrospray-based thrusters are a type of electrostatic propulsion systems that exploit electrospray physical phenomena. These emitters consist of one or several emitting structures in the micro and nanoscale, typically conical or ending in a sharp point. The primary reason for use these architectures is that electrostatic principles allow for the efficient generation of extremely strong electric fields over these small pointy surfaces.

These systems employ ionic liquids (ILs) as propellants. These liquids, also named molten salts, are organic salts that are generally liquid below 100°C. ILs demonstrate thermal stability across a wide temperature range, allowing their use in high-temperature applications. They generally decompose thermally before reaching their boiling point at elevated temperatures. In contrast to conventional molecular solvents, ionic liquids are composed entirely of ions and have a net charge of zero. Their unique properties include low vapor pressure, high electrical conductivity, low volatility, non-flammability, and a broad range of electrochemical stability, making ionic liquids exceptional candidates for various applications [51].

Electrospray emitters feature different architectures based on the method used to transport the propellant to the active zone where emission occurs. These include porous emitters, capillary emitters and externally wetted emitters.

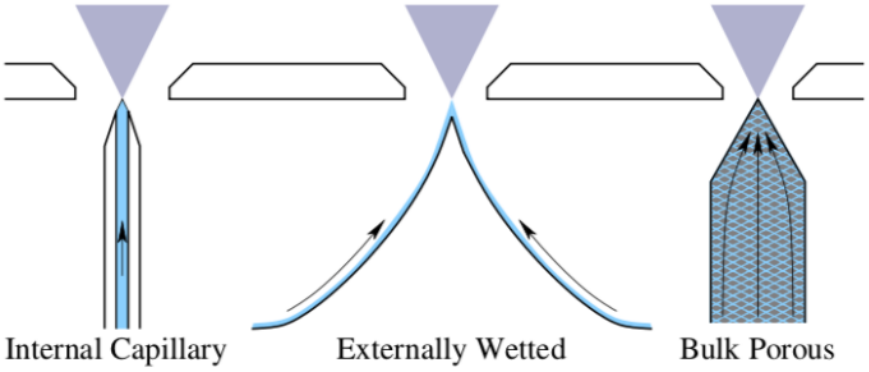

Figure 8: Electrospray emitters architectures based on propellant transport [52].

Porous emitters employ materials that include a network of fine pores that allow propellant flow through capillarity effects [53, 54]. Under a strong electric field, the ionic liquid shapes a Taylor cone in the active zone, resulting in the emission of charged particles. The pores play a key role in emission control by regulating the flow rate, so material selection is important to achieve the desired emission parameters. Common materials employed include metals such as nickel and tungsten, as well as ceramics and sintered materials. Porous systems produce stable emission maintaining a consistent flow due to capillarity effects.

Capillary-type emitters use needle-shaped or cylindrical structures with pipes made from conductive or semiconducting materials [55]. These channels allow the flow of ionic liquid to the emission region through capillarity. The channel diameter enables precise control over the propellant's flow rate, thereby regulating the emission. Such systems are preferred for their ease of manufacturing and simplicity, which make them particularly suitable for small-scale applications prioritizing precise emission control. However, these systems are prone to clogging issues.

Lastly, externally wetted emitters are characterized by tapered structures, where the propellant flow is facilitated across the surface through wicking using roughness or smaller features such as black Si or nanowires [37, 56]. Similar to capillary-type emitters, these systems are typically made of conductive or semiconducting materials. Externally wetted emitters enable larger emission surfaces and higher flow rates compared to the previous systems. The emission performance depends on the number of emitters and properties

of the features that compound the wetting solution, such as their height and diameter. These emitters offer enhanced robustness and higher thrust levels due to their engineered features, as them are not intrinsic properties of the employed material. Despite it, achieving uniform wetting and homogeneity on the emitting surface can be challenging.

Controlling the emission of charged particles is crucial for optimizing the thruster performance, depending on the specific maneuvers or functions they are designed to execute. As previously mentioned, the ejection of particles is influenced by parameters such as flow rate, applied voltages, and emitter architecture. Consequently, these parameters must be tailored to meet the desired specifications. In electrospray systems, the emission regime can be classified into three primary types based on the particles ejected: droplet, ionic, and mixed regimes. Each type offers unique characteristics suited to different applications.

Droplet emission regime involves the emission of charged liquid droplets. This occurs at lower applied potentials, where the electric field does not significantly affects the liquid's surface tension to produce ions. In this emission, a substantial thrust is generated due to the mass of the expelled droplets, making it suitable for maneuvers that require moderate thrust levels [57, 58].

In contrast, the ionic regime is composed entirely of ions. At higher voltages, the generated electric field is strong enough to extract ions directly from the liquid. Also known as Pure Ionic Regime (PIR), this type of emission is characterized by a high exhaust velocity and a high I_{sp}, leading to more efficient propellant consumption [59]. Therefore, is ideal for precise maneuvers and to maximize the duration of the propellant.

Lastly, the mixed emission regime involves both droplets and ions emissions. This intermediate regime takes place at potentials high enough to pull off ions from the liquid while still emitting droplets, enabling emissions of both species simultaneously. This adaptability makes the mixed regime especially useful, offering a balance of the benefits found in the aforementioned regimes. This regime can be tailored to suit various mission stages, delivering both moderate thrust and accurate control when required.

Electrospray thrusters offer significant advantages over other electric propulsion systems discussed earlier. As previously mentioned, their architectures and propellant transport are simpler and more straightforward compared to complex systems like Hall effect thrusters. This simplicity in design and fabrication reduces complexity and cost. Additionally, the different emission modes allow for efficient propellant control and precise thrust, making these systems suitable for a wide range of maneuvers. Their compact size and low power requirements make them particularly ideal for small spacecraft and CubeSats.

Despite these advantages, there are still challenges that must be overcome to fully exploit the potential of this technology. Electrospray thrusters lifespan is limited due to degradation and erosion caused by factors such as electrochemical reactions of the propellant, overspray or electron backscattering. Therefore, optimizing emission control, geometrical features, and the correct selection of the materials and propellants, are key for maximizing the efficiency and performance of these propulsion systems [60–62]. Furthermore, even though their design and fabrication are simpler compared to other systems, miniaturizing these devices remains a challenge that requires advanced microfabrication techniques.

1.4 Microelectromechanical systems

Microelectromechanical systems (MEMS) are miniaturized devices that incorporate both mechanical and electrical features, with sizes ranging from few centimeters to micrometers [63–65]. These devices evolve directly from micromachining technologies initially used for integrated circuits and actuators. Driven by the need to reduce size and costs, MEMS offer enhanced functionality and portability. These innovative tools bridge the gap between nanotechnology and macroscale applications, enabling local functionalities that were previously unattainable with traditional methods.

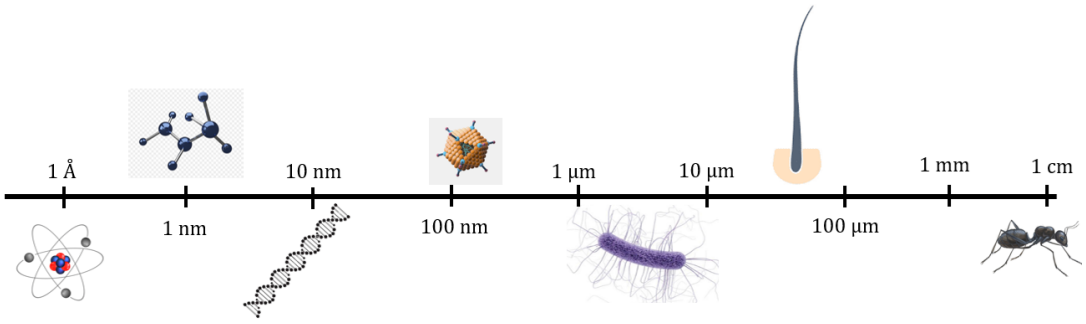

Figure 9: Scale bar for size magnitudes ranging from angstroms (Å) to centimeters (cm), illustrating the relative dimensions of atomic structures, microscopic features, and macroscopic objects.

The development of MEMS requires the use of advanced microfabrication techniques typical of semiconductor manufacturing. These techniques include, among others, photolithography, dry and wet etchings, doping, thin film deposition, and lift-off processes. Microfabrication enables the exploitation of diverse materials such as silicon, polymers, metals, and ceramics, thereby providing great versatility for applications across multiple fields [66–68]. MEMS are extensively used in sensors and actuators [69], radio frequency (RF) devices [70], biomedical applications [71, 72], and even space technologies [73–78].

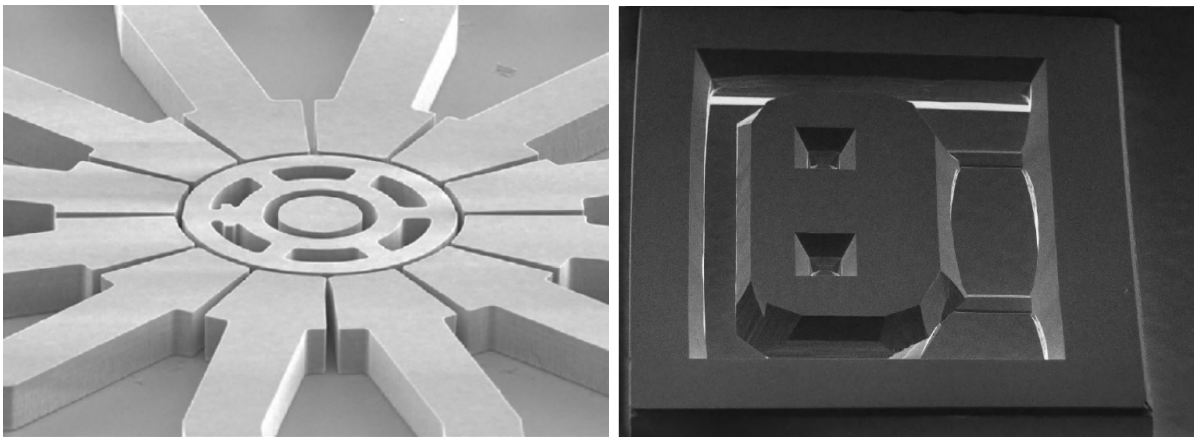

(a) Micromotor (b) Accelerometer

Figure 10: Scanning Electron Microscopy (SEM) images for MEMS devices: a) a micromotor and b) an accelerometer [67].

One of the primary advantages of MEMS is their size-related benefits, which position them as potential solutions to various technological challenges. Their capacity of miniaturization allows MEMS to be highly adaptable across many fields, as they can achieve extremely small sizes ideal for applications requiring high portability. This miniaturization also results in low energy consumption, enhancing their efficiency. The integration of electrical and mechanical components within a single device improves precision and reliability, while also enabling cost-effective mass production through microfabrication techniques. Moreover, due to the large surface area to volume ratio of MEMS, physical properties such as electromagnetics and fluid dynamics significantly influence their design at these scales.

However, MEMS also face certain disadvantages. The design and fabrication of these devices are complex, requiring careful consideration of downsizing factors, which can compromise their durability and strength. Additionally, the small size of MEMS imposes limitations on the forces and energies they can handle, restricting their application in some high-power scenarios.

This technology offers a promising solution for propulsion in small spacecraft. The characteristics of MEMS allow their efficient use with small power inputs, as their microscale properties eliminate the need for a large energy source. Furthermore, their compact size does not compromise the integrity of the satellite, ensuring that the payload remains unaffected.

Chapter 2

2 Electrospray

Electrospray technology, an innovative method of generating fine aerosols through the application of high voltage to a liquid, has found extensive applications across multiple scientific and industrial fields. Its versatility and precision have made it a valuable tool in areas ranging from mass spectrometry [47] to drug delivery [41] and materials science [39,40,42,45,46]. This section digs into the fundamental principles underlying electrospray, including the electrostatics governing the process, the formation and dynamics of Taylor cones, the mechanisms of species emissions, and the fluid mechanics involved. By exploring these core topics, this section aims to provide a comprehensive understanding of the physical phenomena driving electrospray technology and its diverse applications.

2.1 Fundamental physics

2.1.1 Electrostatics

Electrostatics explains the interaction between stationary electric charges, playing a crucial role in the operation of electrospray systems.
Coulomb's law, Eq. 2.1, is the fundamental principle that expresses this interaction between charges through the electric force generated.

$$\vec{F} = \frac{1}{4\pi\epsilon_0}\frac{\mid q_1 q_2 \mid}{\vec{r}^2} \tag{2.1}$$

In equation 2.1, F represents the force, ϵ_0 is the vacuum permittivity, q_1 and q_2 are the charges, and r the distance between them. The generated forces are responsible for the emission of charged droplets or ions from the apex of the cone. Understanding these forces is essential for optimizing electrospray performance, as they influence the stability, size distribution, and velocity of the emitted species, directly impacting the system's efficiency and effectiveness in various applications.

The interaction between charges is finite, making the mathematical understanding of

the forces complex. These forces can be described differently by assuming that each charge generates a perturbation in the space through which they interact. This perturbation is known as a field. Electric field, $\vec{E}$, is defined as the force exerted per charge unit.

$$\vec{E} = \frac{F}{\vec{q}} \tag{2.2}$$

By isolating the parameter F in equation 2.2, and substituting it into equation 2.1, $\vec{E}$ for a punctual charge can be expressed as:

$$\vec{E} = \frac{1}{4\pi\epsilon_0}\frac{q_1\vec{r}}{r^2} \tag{2.3}$$

Although these charges are considered punctual, depending on their concentration in space, is convenient to express them as continous distributions. These distributions can be linear (Eq. 2.4.1), superficial (Eq. 2.4.2) or volumetric (Eq. 2.4.3).

$$\lambda(\vec{r}) = \frac{dQ}{dl} \tag{2.4.1}$$

$$\sigma(\vec{r}) = \frac{dQ}{d\mathcal{S}} \tag{2.4.2}$$

$$\rho(\vec{r}) = \frac{dQ}{d\mathcal{V}} \tag{2.4.3}$$

So, by isolating dQ from the above equations, and replacing it in equation 2.3, the electric field for different charge distributions can be defined as:

$$\vec{E} = \frac{1}{4\pi\epsilon_0}\int_{\mathcal{L}} \lambda(\vec{r})\frac{1}{r^2}\vec{dl} \tag{2.5.1}$$

$$\vec{E} = \frac{1}{4\pi\epsilon_0}\int_{\mathcal{S}} \sigma(\vec{r})\frac{1}{r^2}\vec{d\mathcal{S}} \tag{2.5.2}$$

$$\vec{E} = \frac{1}{4\pi\epsilon_0}\int_{\mathcal{V}} \rho(\vec{r})\frac{1}{r^2}\vec{d\mathcal{V}} \tag{2.5.3}$$

In systems characterized by more intricate charge distributions, the principle of superposition is applied, establishing that the overall electric field at any given point is the vector sum of the individual electric fields produced by each point charge:

$$\vec{E_{total}} = \sum_{n=1} \vec{E}_n \tag{2.6}$$

Despite the electric field itself is intangible, its effects can be represented through the concept of electric field lines. These lines provide a representation to understand the direction and intensity of the electric field generated in the space surrounding charges. In other words, electric field lines are a conceptual tool used to visualize the behavior of the electric field upon other charges. The direction of the lines indicates the direction a positive test charge would move if placed in the field, while the density of the lines reflects the field's intensity, i.e., a greater number of lines per unit area signifies a stronger field.

The behavior of the electric field is most accurately described by Gauss's law, which expresses the electric flux through a closed surface to the charge enclosed within that surface as follows:

$$\oint_{\partial \mathcal{V}} \vec{E} d\vec{A} = \frac{Q_{total}}{\epsilon_0} \tag{2.7}$$

In equation 2.7, $\vec{E}$ denotes the electric field, $d\vec{A}$ is a vector representing an infinitesimal element of the surface area pointing outward, Q_{total} is the total charge enclosed within the volume, and ϵ_0 is the vacuum permittivity. Gauss's theorem enables the determination of electric fields for systems with significant symmetry. Equation 2.7 can also be expressed in terms of the divergence, ∇, of the field:

$$\oint_{\partial \mathcal{V}} \vec{E} d\vec{A} = \int_{\mathcal{V}} (\nabla \cdot \vec{E}) d\mathcal{V} \tag{2.8}$$

Given the equation 2.4.3, equation 2.7 can be redefined,leading to Maxwell's first law.

$$\nabla \cdot \vec{E} = \frac{\rho}{\epsilon_0} \tag{2.9}$$

According to Gauss' law, the total electric flux through a closed surface is proportional to the charge enclosed within the surface. Inside a perfect conductor material, the electric field must be zero due to charge movement to cancel it. Outside the enclosure, the electric field is non-zero and points straight out, perpendicular to the surface. Through Gauss's law, the flux outside the enclosure is $\vec{E} \cdot \vec{A}$, where $\vec{A}$ is the area of a zone at the interface of the conductor. The flux is equal to the surface charge density, ρ, divided by the vacuum permittivity, ϵ_0. Hence, the field is perpendicular and depends on the surface charge density. Otherwise, it would cause charge movement along the surface, breaking the electrostatic equilibrium.

Electric potential (ϕ) is a key parameter for generating the electric field required for emission. Understanding the potential electric field interactions helps to explain the work done by electric forces and the movement of charges within different configurations. It is defined as the work required to move a unit charge from one point to another within an electric field.

$$\phi = \frac{\mathcal{W}}{q} \tag{2.10}$$

Hence, from equations 2.2 and 2.10:

$$\phi(\vec{r}) = -\int_{\mathcal{L}} \vec{E} d\vec{L} \tag{2.11}$$

Given that the electric field is conservative, i.e., $\nabla \times \vec{E} = 0$, the work exerted by a conservative force does not depend on the trajectory. The gradient theorem allows to define then:

$$-\nabla\phi = \vec{E} \tag{2.12}$$

Equation 2.12 define that $\vec{E}$ points in the direction where the potential decreases faster, being the magnitude of the filed proportional to the change in potential. By relating equations 2.9 and 2.12, the well-known Poisson equations is obtained, relating the electric potential and the charge distribution in space.

$$\nabla^2\phi = -\frac{\rho}{\epsilon_0} \tag{2.13}$$

Electrostatically, electrospray-based thrusters can be understood as capacitors. A capacitor stores energy in the form of electrical charge on two conductive plates separated by a dielectric. In the electrospray thruster, the ions generated in the emitter can be seen as the "charge accumulation" in the emitter, similar to how the plates of a capacitor store charge. The distribution of the charges along the emitter system is a function of the distribution of the generated electric field, playing an important role in the emission of the species.

2.1.2 Taylor cone

Electrospray is a phenomenon wherein charged particles, ions and droplets, are generated and accelerated from a liquid when subjected to a sufficiently strong electric field. This emission process occurs in sharp architectures governed by the interplay of electrostatics and fluid dynamics [38]. The electric field exerts a force that deforms the liquid surface into a structure known as meniscus, counteracted by surface tension striving to maintain a spherical shape. As the electric field strength increases, the meniscus undergoes a hydrodynamic transformation, ultimately adopting a cone-like shape known as a Taylor cone [38, 79]. At this stage, the electric field force balances and eventually overcomes the surface tension, leading to the emission of charged species from the ionic liquid.

The traditional approach to understanding Taylor cone formation involves considering

a droplet within a capillary tube subjected to an electric field. However, electrospray systems can vary significantly in their propellant transport mechanisms, necessitating a broader perspective. For instance, systems with a planar liquid surface subjected to a uniform electric field—without confinement to specific geometries-are of particular interest. In such scenarios, the liquid surface interacts with the applied electric field $\vec{E}$, with the surface tension (γ) working to keep the surface flat. Simultaneously, the electric field imposes stresses on the surface, causing it to deform and potentially lead to the formation of a Taylor cone. The electric field exerts a pressure, P_E, over the surface given by:

$$P_E = \frac{\epsilon_0 E^2}{2} \tag{2.14}$$

Equation 2.14 describes the pressure due to the electric field in the normal direction. It is obtained through Maxwell stress tensor, $\vec{T} = \epsilon_0 \left(\vec{E} \otimes \vec{E} - \frac{1}{2} E^2 \vec{I} \right)$, where $\vec{E}$ is the electric field vector, E is the electric field modulus and $\vec{I}$ the identity matrix. For a uniform electric field, only the term operated by the dyadic product matters, giving $P_E = \epsilon_0 E^2$. This value represents both compressive and tensile stress components. For an electrostatic equilibrium, the surface experiences only the tensile stress, which is half of the total stress, expressed in Eq. 2.14.

Simultaneously, the exerted force due to surface tension is defined by the Young-Laplace equation:

$$P_{liquid} = \gamma \left(\frac{1}{R_1} + \frac{1}{R_2} \right) \tag{2.15}$$

where R_1 and R_2 Equation 2.15 are the principal radii of curvature of the surface. Considering a conical deformation of the surface, Eq. 2.15 can be approximated to:

$$P_{liquid} \approx \frac{2\gamma}{R} \tag{2.16}$$

Hence, in equilibrium, equations 2.14 and 2.16 are equal, balancing each other as New-

ton's third law describes:

$$\frac{\epsilon_0 E^2}{2} = \frac{2\gamma}{R} \tag{2.17}$$

From equation 2.17, the electric field term can be isolated to obtain the critical field strength (E_c) to form a Taylor cone:

$$E_c = \sqrt{\frac{4\gamma}{\epsilon_0 R}} \tag{2.18}$$

Equation 2.18 demonstrates that the electric field strength required to shape a Taylor cone increases with surface tension and decreases with the radius of curvature at the cone's tip. Therefore, the stability of the Taylor cone is influenced by various parameters, including the flow rate of the liquid, the electric field strength, and the properties of the liquid such as viscosity and conductivity.

The cone forms when the electric field overcomes the surface tension, causing the liquid to elongate and emit a jet from the cone's apex. This jet can break up into fine droplets or form a continuous stream, depending on the operating conditions. The onset voltage (V_0) is a crucial parameter that determines the initiation of the electrospray process. It is the minimum voltage required to create a sufficiently strong electric field to overcome the surface tension of the liquid, leading to the formation of a Taylor cone and the subsequent emission of ions or droplets. Establishing that for a sharp emitter, the electric field takes into account the distance D between the emitter and the counter electrode, it can be described as:

$$E \approx \frac{V_0}{R \ln\left(\frac{2D}{R}\right)} \tag{2.19}$$

From Eq. 2.17 and 2.19, the onset voltage (V_0) is expressed as:

$$V_0 = \sqrt{\frac{4\gamma R}{\epsilon_0}} \ln\left(\frac{2D}{R}\right) \tag{2.20}$$

Equation 2.20 is composed by γ as the liquid's surface tension, D as the distance between electrodes, R being the cone radius and ϵ_0 as the vacuum permittivity. This expression reveals the dependence between emitters performance and its geometrical features.

Typically, the half-angle of the Taylor cone is 49.3 degrees [38, 79]. It is derived from a balance of forces in the electrohydrodynamic equilibrium. This specific angle is a result of the interaction between the electric field and the surface tension forces. Deviations from this angle can occur due to non-ideal conditions, such as non-uniform electric fields or variations in liquid properties.

2.1.3 Species emission

Subsequent to the formation of the Taylor cone, the electric field intensity at its apex reaches a maximum, resulting in significant electric stress within the liquid. The Taylor cone sharpens the liquid to a point where the radius of curvature (R) approaches to zero. This extreme sharpening facilitates the emission of charged particles, which may manifest as either ions or droplets, depending on the specific conditions of the system.

In the droplet emission mode, the fluid generates small charged droplets. This process occurs when the Taylor cone transitions into a jet of droplets at a critical radius where charge convection within the fluid surpasses electrical conduction. The instability generated under these conditions leads to the ejection of droplets from the apex of the cone [79]. The stability of the emitted droplets can be controlled by their size. As these droplets are formed via the electrospray process, they inherently carry an amount of electric charge. The electrostatic forces arising from these charges act to elongate and destabilize the droplets, while surface tension works to maintain their equilibrium. The maximum charge (Q_R) that a droplet of radius r can sustain before becoming unstable is defined by the Rayleigh limit (Eq. 2.21). Beyond this limit, the droplet becomes susceptible to fission

due to Coulombic repulsion, leading to the breakdown of the droplet into smaller fragments.

$$Q_R = 8\pi\sqrt{\epsilon_0 \gamma r^3} \tag{2.21}$$

From equation 2.21 it can be determined that the Rayleigh limit can be found when the surface tension force and the electrostatic repulsion force are approximately equals as:

$$\gamma r \approx \frac{Q_R^2}{\epsilon_0 r^2} \tag{2.22}$$

The electrostatic forces overcome the surface tension, causing the droplet to undergo Coulomb fission. This process involves the droplet splitting into smaller droplets, each carrying a portion of the original charge, thereby reducing the electrostatic repulsion and restoring stability. The relationship between charge and stability is crucial for applications requiring precise control over droplet size and charge, such as in mass spectrometry and propulsion systems.

The ionic regime occurs under high electric field conditions, where the electric field strength at the apex of the Taylor cone is sufficiently strong to directly pull individual ions directly from the liquid surface.
This emission mode can be explained by the field evaporation model, which describes how the applied electric field reduces the energy barrier for ion evaporation. Under these high-field conditions, the energy required for ions to escape from the liquid surface is significantly lowered, allowing them to be pulled directly into the gas phase.

$$I = n_0 e^{\left(-\frac{W}{k_B T}\right)} e^{\left(\frac{\beta E_c}{k_B T}\right)} \tag{2.23}$$

In equation 2.23, n_0 is a parameter which represents the density of emission sites and the frequency of ion attempts to escape, W is the energy needed to remove an ion from the

liquid surface, β is a field enhancement factor, k_B is the Boltzmann constant and T the temperature. Under normal conditions, ions from the liquid are stabilized by solvation and surface tension. However, a sufficiently strong electric field (E_c), exerts a force on these ions, reducing the energy needed to be ejected. Ion emission takes place from a critical electric field which is usually around 1 V/nm for ionic liquids [80, 81].

Particle emission in electrospray systems—whether in droplet, ion, or mixed regimes—is strongly influenced by several key factors such as the electrical conductivity of the propellant, the strength of the electric field, and the flow rate of the system. These parameters interact in complex ways to determine the nature of the emitted particles.

The electric field plays a critical role in governing the emission regime. Higher electric fields tend to favor the ionic regime, as the intense field strength at the apex of the Taylor cone enables the direct extraction of ions from the liquid surface. The magnitude of the electric field achievable in a thruster is influenced by the applied voltages, which are in turn constrained by the design and material limitations of other components within the device, such as printed circuit boards (PCBs).

The flow rate control is equally important in determining the type of emission. In systems with low flow rates, ion emission typically dominates because the limited flow results in a Taylor cone that is highly concentrated at the apex, but insufficient to produce a continuous jet of droplets. Conversely, at higher flow rates, the propellant supply is ample enough to sustain a Taylor cone that can emit species with measurable mass, leading to the production of charged droplets.

Optimizing the performance and efficiency of electrospray-based systems hinges on several factors, including electric field strength, propellant conductivity, and flow rate. Unlike the electric field strength, which is constrained by the applied potential and the design limitations of the system, and the propellant's conductivity, which is an intrinsic property of the material, the flow rate is a variable that can be independently controlled.

This flexibility makes flow rate a crucial parameter in determining the emission regime and, consequently, the overall effectiveness of the system. The following section aims to describe the physics of fluid mechanics to optimize the flow rate, allowing precise control of the emission characteristics and improving system performance.

2.2 Fluid mechanics of externally wetted systems

Effective control of propellant transport is crucial for optimizing the performance of electrospray devices, as system efficiency is directly dependent on this parameter. The different electrospray systems, discussed in detail in Section 1.3.2, have distinct methods for managing propellant transport, tailored to the type of wetting solution employed. In porous systems, for example, the flow rate is primarily determined by the size of the pore network. Capillary emitters rely on the dimensions of the capillaries to control transport, while externally wetted systems adjust parameters such as diameter, height, or the number of structural elements used. In this project, a novel externally wetted emitter system has been designed, utilizing a network of nanowires for propellant transport. This section delves into the fluid mechanics governing the behavior of such externally wetted systems.

While several models exist to describe capillary performance and permeability in porous media and micropillar arrays [82], these models are not universally applicable to all types of propellant transport systems. The system developed in this thesis employs a nanowire network, where the spacing between nanowires varies within a certain range due to fabrication constraints, as detailed in Section 5.2. Despite this variability, the network can be approximated as a staggered pattern with hexagonal unit cells, where the nanowires are separated by a distance S. This approximation allows for the analysis and optimization of the propellant transport mechanism within the unique configuration of the designed system.

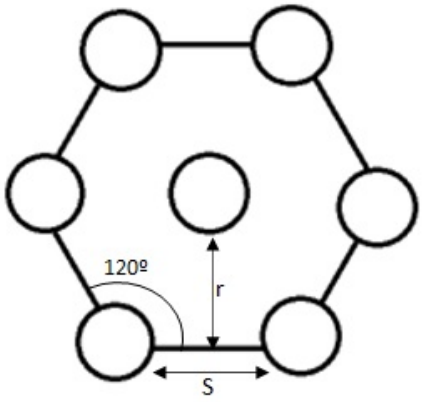

Figure 11: Schematic of the hexagonal unit cell of the nanowires network.

Figure 11 depicts the pattern and different parameters, including the radius (r) and distance between nanowires (S), that allows establishing a relation to obtain the number of particles within the unit cell. It is well known that the angle in the edges of an hexagon is 120°. So, it is clear that $\frac{1}{3}$ of nanowire per edge can be found within the unit cell. Since there is $\frac{1}{3}$ nanowire per edge plus one nanowire at the center of the pattern, the unit cell is composed of 3 nanowires.

Given that pattern, the area of the unit cell is $A = 2rS$, i.e., the area of a hexagon. Given that, $r = \frac{\sqrt{3}}{2}S$, the area of the unit cell can be determined in terms of S as:

$$A = \frac{3\sqrt{3}}{2}S^2 \tag{2.24}$$

Due to the inherent limitations of the fabrication process, achieving a perfectly ordered nanowire system is not feasible. As a result, the equation 2.24 must be correlated with an additional parameter: the density of nanowires per unit area. This density can be effectively controlled through the fabrication technique employed, which in this case is colloidal lithography [83, 84]. Colloidal lithography leverages a suspension of particles that include an amide positive radical, facilitating electrostatic interactions between the particles and the negatively charged surface. By adjusting the dilution of this suspen-

sion, the density of nanowires on the device surface can be modulated. This density is defined as the number of nanowires within a unit cell divided by the area of that unit cell. Understanding and controlling this density is crucial for optimizing the performance of the nanowire network, as it directly impacts the efficiency of propellant transport in the electrospray system.

$$\mathcal{N} = \frac{2}{\sqrt{3}S^2} \tag{2.25}$$

Nanowires are three-dimensional structures characterized by their height h and diameter d. These parameters are critical to determine the propellant transport efficiency. A greater nanowire height increases the volume of the propellant that can be transported across the surface, enhancing the system's overall capacity. Conversely, the diameter of the nanowires influences the ease with which the liquid wicks through the structure. As the diameter increases, the resistance to fluid flow also increases, making it more difficult for the propellant to move through the network. To accurately assess and optimize the transport efficiency, it is essential to consider the volume of nanowires per unit surface area. The volume of nanowires within a unit cell is defined as follows:

$$V_{NWs} = 3\pi h r^2 = 3\pi h \left(\frac{d}{2}\right)^2 = \frac{3}{4}\pi h d^2 \tag{2.26}$$

Since the unit cell is defined as a unit area, we find that its volume is defined as:

$$V_{cell} = \frac{3\sqrt{3}}{2} S^2 h \tag{2.27}$$

By means of the equations 2.26 and 2.27,the solid volume fraction (φ) is defined, representing the proportion of the total volume occupied by the nanowires within the unit cell.

$$\varphi(S) = \frac{\pi d^2}{2\sqrt{3}S^2} \tag{2.28}$$

Equation 2.28 can be rewritten in terms of the density $\mathcal{N}$ as:

$$\varphi(N) = \frac{N\pi d^2}{4} \tag{2.29}$$

The fluid transport within the emitter system developed in this thesis can be extrapolated to that of a fibrous porous media [82, 85, 86]. In fluid dynamics, the permeability (K) of a porous medium is a parameter that governs the flow of the propellant through the material. The permeability measures the medium's capacity to allow fluid passage, which depends on factors such as pore size, shape, and distribution. In the externally wetted system designed here, the spacing between two nanowires can be analogized to the pores in a fibrous medium. This analogy allows us to apply existing mathematical models to estimate the system's permeability. Specifically, the model developed by Tamayol and Bahrami for a staggered pattern in fibrous porous media provides a framework for calculating permeability [86], expressed as:

$$\frac{K}{d^2} = \frac{0,16\left[\frac{\pi}{2\sqrt{3}\varphi} - 3\sqrt{\frac{\pi}{2\sqrt{3}\varphi}} + 3 - \sqrt{\frac{2\sqrt{3}\varphi}{\pi}}\right]}{\sqrt{1-\varphi}} \tag{2.30}$$

By applying equations 2.29 and 2.30, the permeability (K) of the system an be determined as a function of the nanowire density $\mathcal{N}$. Although the overall permeability of the system can be defined, it should be noted that the system is composed of both conical and planar structures. In fluid mechanics, fluid flow through porous media is typically described by Darcy's law, Eq. 2.31, assuming homogeneous permeability in all directions. However, due to the presence of conical and planar elements with potentially different permeability characteristics, this complexity must be considered when analyzing the fluid dynamics of the system.

$$\vec{\nabla} P = -\frac{\mu}{K}\vec{q} \tag{2.31}$$

Equation 2.31 describes the physics through the volumetric flux $\vec{q}$, hydraulic gradient $\vec{\nabla} P$,

viscosity μ and permeability K. It can be redefined taking into account that $\vec{q} = Q/A$ and $\vec{\nabla} P = dP/dL$:

$$Q = \frac{KA}{\mu} \frac{dP}{dL} \tag{2.32}$$

Therefore, equation 2.32 is further described as a function of the flow rate Q and the ratio of the pressure difference as a function of distance. Given a planar surface with a nanowire array, a microchannel of path L under an initial pressure P_0 is considered. So, equation 2.32 can be integrated between the limits 0 to L and from P_0 to P:

$$\int_0^L Q \, dL = \int_{P_0}^P \frac{KA}{\mu} \, dP \tag{2.33}$$

Resulting in the same equations as 2.32 but without differential notation.

$$Q = \frac{KA}{\mu L} \Delta P \tag{2.34}$$

The correlation between an electric circuit and a fluidic circuit, as described by Ohm's law, allows the pressure difference (ΔP) to be defined as the product of the resistance to fluid flow (R) and the flow rate (Q).

$$\Delta P = QR \tag{2.35}$$

By applying Darcy's law, Eq. 2.34, and the definition of a fluidic circuit, Eq. 2.35, the hydraulic resistance can be determined as a function of the relevant parameters.

$$R = \frac{\mu L}{KA} \tag{2.36}$$

Equation 2.36 demonstrates that propellant flow resistance is inversely proportional to

permeability. Hence, higher permeability indicates easier fluid flow, whereas lower permeability suggests smaller or more constricted pores, which impede fluid movement. In an externally wetted system utilizing nanowires, fluid propagation becomes more difficult as the density or diameter of the nanowires increases.

In a three-dimensional structure such as a cone, equation 2.31 must be interpreted with specific criteria tailored to the geometry of the structure.

$$\frac{Q}{A} = -\frac{K}{\mu}\left(\frac{\partial P}{\partial x}, \frac{\partial P}{\partial y}, \frac{\partial P}{\partial z}\right) \tag{2.37}$$

Firstly, it is assumed the symmetry along the x-y plane, i.e., the system only varies along the z axis as Fig. 12 depicts.

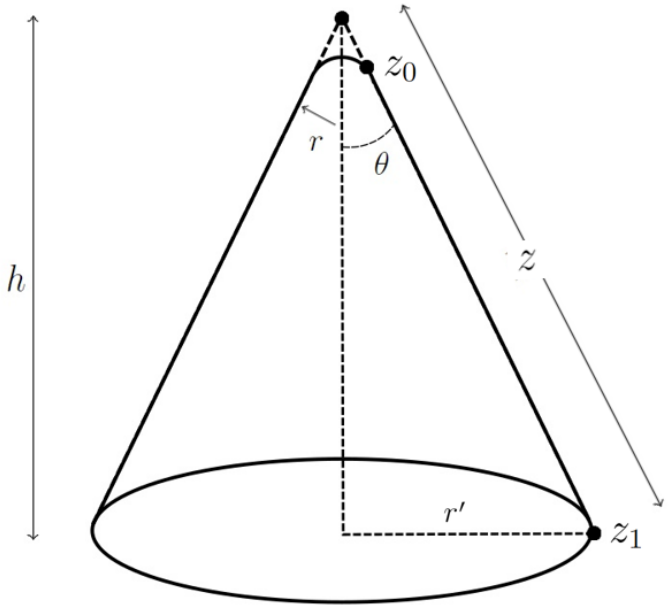

Figure 12: Externally wetted emitter reference system for microfluidics mechanics.

Hence, equation 2.37 is defined as:

$$\frac{Q}{A} = -\frac{K}{\mu}\frac{dP}{dz} \tag{2.38}$$

By isolating the pressure differential as z function and by introducing the cone surface area as height z and angle θ function it can be expressed as:

$$\frac{dP}{dz} = -\frac{\mu}{K}\frac{Q}{2\pi z \sin\theta} \tag{2.39}$$

Equation 2.39 is integrated between the limits 0 to P for dP and between z_0 and z_1 for dz, establishing z_0 as the highest point of the structure and z_1 as the lowest point. r'

$$\int_0^P dP = \frac{-\mu}{K}\frac{Q}{2\pi \sin\theta}\int_{z_0}^{z_1}\frac{1}{z}\,dz \tag{2.40}$$

$$P = \frac{\mu}{K}\frac{Q}{2\pi \sin\theta}\ln\left(\frac{z_0}{z_1}\right) \tag{2.41}$$

So, applying basic trigonometry, $z_0 = h/\cos\theta$ and $z_1 = r/\tan\theta$ can be expressed. For z_1 it can be assumed an infinitesimal tip, $dh = dz$, obtaining the previous statement by neglecting the angle functions:

$$P = \frac{\mu}{K}\frac{Q}{2\pi \sin\theta}\ln\left(\frac{h\tan\theta}{r\cos\theta}\right) \tag{2.42}$$

Hence, the expression for Darcy's Law of a conic surface can be expressed in terms of hydraulic resistance (R) employing the Ohm's Law analogy, 2.35, on Eq. 2.43.

$$R = \frac{\mu}{K2\pi \sin\theta}\ln\left(\frac{h\tan\theta}{r\cos\theta}\right) \tag{2.43}$$

As for the planar surface, equation 2.43 similarly reveals an inverse proportionality between hydraulic resistance (R) and permeability (K), indicating that higher permeability facilitates easier fluid flow. Moreover, the dynamic viscosity (μ) has a direct proportionality, implying that fluids with higher viscosity encounter greater resistance as they

flow through the medium. The area and length parameters are adjusted to reflect the conical geometry. The term $\sin(\theta)$ suggests that as θ increases, the hydraulic resistance decreases, allowing the fluid to flow more freely. However, it is important to note that the experimental case differs from the idealized model described by the equation. The microfabrication process used in this thesis cannot achieve perfect conical structures meeting the precise properties required for emission. As a result, this model should be understood as a theoretical framework rather than an exact representation of the experimental system.

Chapter 3

3 Thesis objectives

The focus of this doctoral thesis lies at the intersection of, in-space propulsion for small spacecrafts and MEMS engineering fields. This research area has attracted considerable attention due to its potential to address challenges faced by small satellites, which are increasingly used in fields such as the Internet of Things (IoT), telecommunications, weather and environmental monitoring, Earth observation, and national defense. Among these potential solutions to improve operational longevity are precise control for orbital positioning, attitude control and de-orbiting maneuvers for space debris reduction. On the other hand, MEMS technology represents a promising avenue for developing compact, reliable, and precise devices that offer low power consumption and cost-effectiveness. The versatility of MEMS devices makes them suitable for various applications, including space propulsion, where their small size and high performance are particularly advantageous.

Given the growing demand for advanced propulsion technologies, there is an urgent need to deepen our understanding of MEMS-based space propulsion systems and to innovate new techniques that can overcome the limitations of current methods. This thesis aims to contribute with novel insights at the convergence of these two fields, seeking to bridge existing knowledge gaps and push the boundaries of current technological capabilities.

The primary objective of this doctoral research is to design, fabricate, and characterize a silicon-based electrospray propulsion system for nano- and picosatellites. The research is structured into several key phases. The initial phase involves the design of the propulsion device, guided by the study of its physical properties, such as emission characteristics and propellant management, through mathematical models and simulation tools. Post-characterization analysis is then used to optimize the design. The fabrication of the device leverages well-established silicon microfabrication techniques, including photolithography, etching processes, and scanning electron microscopy (SEM) inspections. Additionally, innovative approaches such as colloidal lithography have been explored to develop the nanowire network, which plays a key role in propellant transport. Finally, a

preliminary characterization of the fabricated devices has been conducted to demonstrate their functionality. This characterization has also validated the system's physical properties, including emission behavior, the architecture of the emitting structures, and the device's durability over extended emission periods.

The outcomes of this doctoral research are expected to make several significant contributions to the fields of MEMS technology and in-space propulsion systems. These contributions include:

- Investigate electrospray-based thrusters and physics behind.
- Establishing a manufacturing process through microfabrication techniques for externally wetted emitters devices in aim to its commercialization.
- Explore alternative manufacturing methods to improve its yield.
- Characterization of externally wetted emitters to understand its behavior and its functionality.

This project has been carried out by IENAI SPACE, under the supervision of Dr. Javier Cruz, and the Institute of Microelectronics of Barcelona (IMB-CNM, CSIC), within the Nano and Microsystems department under Dr. Borja Sepúlveda supervision. Throughout this thesis, Raúl Ramos-Tomás has conducted his research, producing the aforementioned devices and a scientific article published in ACS Applied Electronic Materials.

Chapter 4

4 ATHENA Thruster

The technology developed in this thesis is related to a cutting-edge propulsion system known as ATHENA, which stands for "Adaptable THruster based on Electrospray for NAnosatellites". ATHENA represents a significant advancement in propulsion technology, specifically tailored to meet the stringent demands of nano- and picosatellite missions. The architecture of this system is being meticulously crafted with a focus on modularity, integration, and scalability, enabling it to adapt to a variety of mission requirements while maintaining high performance and reliability. The system's modular design allows for the seamless integration of various subsystems, allowing a wide range of customization based on specific mission objectives and satellite configurations. In the following section, we will delve into the detailed architecture of ATHENA, exploring each of its critical subsystems. This in-depth examination will provide a comprehensive understanding of the propulsion system's design, the manufacturing processes involved, and how these elements contribute to its overall performance.

4.1 Architecture

ATHENA is composed by interconnected systems designed to produce efficient and reliable thrust, as illustrated in Fig. 13, which shows the overall architecture of ATHENA. The core of ATHENA is the electrospray emitter device, which generates thrust by precisely controlling the emission of charged particles. This core unit is supported by several essential subsystems that work to ensure optimal performance, which include: i) the nanostructured emitters chip that controls the fluid to the emitters where the electric field is concentrated, ii) the extractor grid, which plays a crucial role in biasing the liquid and accelerating the charged particles to produce thrust; iii) the frame that enables emitters/grid alignment, provides structural integrity and avoids flooding, and iv) the propellant management unit (PMU), which enables the steady flow of propellant towards the emitters. Additionally, the system is equipped with advanced control electronics, specifically designed to maximize the thruster efficiency and responsiveness.

The primary contribution of this thesis has been focused on the design, fabrication, and optimization of the emitter device within ATHENA. Through these contributions, the work has advanced the emitter's capabilities in maintaining a stable and efficient thrust, supporting ATHENA's objectives of high performance and reliability in thrust generation.

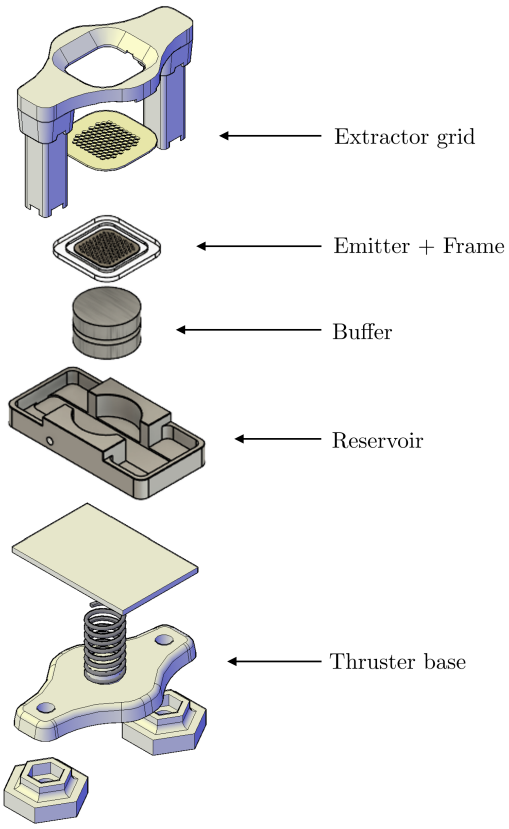

Figure 13: Exploded view of experimental ATHENA's assembly.

4.1.1 Emitters chip

The emitter device is designed as an array of silicon microneedles arranged in a hexagonal pattern, fabricated through silicon microfabrication processes. The microneedles are an efficient structure for concentrating high electric fields, as detailed in section 2.1.1, making them highly effective in inducing the emission process required in electrospray applications. This concentration of the electric field at the needle tips enables precise control over particle emission, a critical requirement for efficient electrospray thruster operation.

The surface of the system is nanostructured with an array of vertically oriented silicon nanowires, whose height, diameter, and surface density are tunable. These nanostructures significantly increase the surface area to enhance the capillary forces that drive the propellant flow, thus facilitating the spontaneous movement of the propellant towards the emitter tips, where the electric field is concentrated. The emitters are connected to the propellant reservoir through an array of feeding holes, each with a diameter of 100 μm. In the latest emitter chip model, as shown in Fig. 14, these holes are arranged in a star-like shape, a configuration specifically designed to optimize capillary action and ensure efficient propellant delivery to the emitter structures.

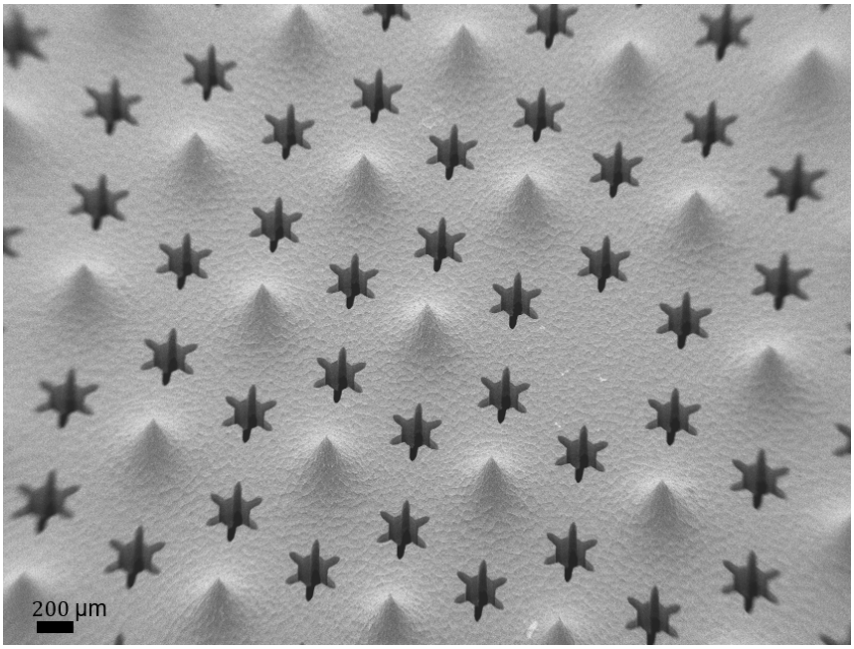

Figure 14: Top-view SEM image from an emitter array.

Within the framework of this thesis, a emitters chip prototype has been designed and developed incorporating 101 emitter microcone shape microneedles. The microcones have a height of 190 μm and exhibit an increasing towards the tip, as a result of the employed reactive ion etching technique. As we will see in Chapter 6, control of the slop is critical to ensure a correct emission pattern.

Additionally, the nanowires on the microneedles are characterized by diameters ranging between 550-600 nm, heights of approximately 3 μm and a surface density of 0.7 NW/μm^2.

These dimensions are controlled by the fabrication techniques, which will be discussed in detail in section 5.2.

Although the current configuration achieves effective performance, throughout this thesis, alternative architectures have been explored, including increasing the number of emitters, altering their geometric properties, and investigating alternative fabrication methods to further optimize performance for various propulsion requirements. This adaptability ensures that the system can be tailored to meet the specific demands of different missions.

4.1.2 Extractor grid

The extractor grid is a layer that contains an array of holes aligned with the emitter structures. Positioned in front of the emitter device, it functions as the upper electrode, applying the necessary bias to generate an electric field that initiates particle emission, and to accelerate the emitted species. Initially, the grid was fabricated from silicon wafers with a thickness of 200 μm, using a dry etching process. In the latest model, however, it is manufactured from fused silica through a Selective Laser Etching method. This grid features an array of 600 μm diameter holes, and its top surface is metalized to enable its function as the upper electrode.

The transition to silica was driven by its non-conductive properties, which eliminate the risk of short circuits caused by ionic liquid accumulation. Such accumulation, arising from overspray and off-axis emission phenomena, had been a concern in earlier designs. By using fused silica, the grid ensures a more stable and reliable operation, critical for maintaining consistent performance.

A voltage applied between the extractor grid and the ionic liquid triggers the electrospray emission and regulates the intensity of the emitted ionic current. These advances in grid design, particularly the adoption of fused silica and selective laser etching, not only improve the structural integrity and precision but also enhance the grid's compatibility with high-performance applications by mitigating operational issues linked to conductive

materials.

4.1.3 Alignment frame

The frame is an auxiliary subsystem designed to facilitate the assembly and precise alignment of the emitter within the system. It also ensures the optimum separation distance between the subsystems and prevents the propellant from spreading beyond the emitter area, which could lead to short circuits in the system. The frame is composed of a low-surface-energy, chemically, and mechanically robust polymer, ensuring stability and reliability during operation.

Currently, the frame is manufactured using EpoTek 302-3M, an epoxy known for its mechanical strength, chemical resistance, and compliance with low outgassing requirements. It is stable across the desired operational temperature range (-40 to 100 °C). The fabrication process involves replica molding from Polydimethylsiloxane (PDMS) masters, which are derived from a multi-level SU-8 wafer prepared through UV lithography technique. The frame accommodates both the emitter and grid, incorporating low-energy barriers to prevent the propellant from escaping the active area, ensuring reliable performance.

Despite its functionality, the main limitation of the frame lies in the manufacturing process. The current method is manual and, although replica molding is employed, it is time-consuming and requires meticulous attention to detail to ensure that the pieces remain free of stress and perfectly flat. This manual process poses challenges in terms of scalability and reproducibility, which may impact the overall efficiency of production in high-volume applications.

4.1.4 Propellant Management Unit

The buffer, positioned beneath the emitter, plays a critical role in the emission system by holding a small volume of propellant, sufficient for a few hours of continuous operation for emission analysis experiments. The buffer passively feeds the propellant through capillary forces to the emitter, ensuring a stable and spontaneous refill of propellant as ions are

emitted. As previously discussed in sections 1.3.2 and 2.2, the nanowires on the emitters chip surface generates stronger capillary forces, allowing the propellant to flow efficiently without active intervention. In addition to its function as a propellant reservoir, the buffer also serves as an electrode for biasing the liquid, contributing to the overall electrospray process.

The buffer is fabricated via Selective Laser Melting (SLM), a 3D metal printing technique, using aluminum. Its central section is designed to retain the ionic liquid within its channels through capillary forces, preventing unintended leakage under normal conditions. These forces contain the liquid until the applied electric field generates sufficient pressure to overcome them, pulling the propellant into the emitter system. Small 100 μm feeding holes channel the ionic liquid from behind the emitter, ensuring a controlled and consistent flow of propellant. The outer section of the buffer provides structural support and facilitates integration with the frame. As a metallic component, it also serves as a high-surface-area electrode to bias the propellant, establishing the proper electrical conditions for ion emission.

Although the buffer fulfills its intended function effectively, SLM fabrication technology presents limitations in terms of precision. The minimum feature size achievable is around 200 μm, with tolerances of several tens of microns, which restricts the ability to achieve the desired geometric precision. Since the buffer's performance is highly dependent on both material properties and geometric accuracy, alternative manufacturing technologies are being explored, such as metal photopolymerization 3D printing, which can achieve a minimum feature size of 25 μm, potentially providing the precision required to optimize the buffer's performance.

4.2 Emission

The emitter devices designed as part of this thesis are not only modular in terms of the number of structures but also allow for modifications to structural parameters, such as geometry, to influence the emission of species. As discussed in section 6.1, [87], altering

the angle of the emitter cone has a direct impact on the emitted beam profile. In other words, it affects the overall efficiency of the system. This is because we found out that the beam's divergence is a function of the microcones, and a wider tip can lead to emissions from points far from the central axis, thereby reducing the system's efficiency.

On the other hand, as highlighted in section 2.2, the hydraulic resistance of the nanostructured surface also plays a crucial role in the emission process. Proper control of the propellant flow is key for defining the specific species being emitted (i.e., ions or droplets) and can also slightly adjust the angular emission distribution, improving propulsion efficiency. These findings underscore the importance of precise geometric design in optimizing the performance of electrospray thrusters, offering valuable insights for developing advanced, high-efficiency propulsion systems for small satellites.

4.3 Propellant

The selection of propellant, particularly ionic liquids, is essential for the performance of externally wetted electrospray emitters, a key component in micro-propulsion systems. The unique properties of ionic liquids, such as their negligible vapor pressure, high electrical conductivity, low viscosity, and high surface tension, make them well-suited for space applications [88]. For externally wetted emitters, the balance between capillary and electrical forces governs the emission process. Selecting an appropriate ionic liquid is critical to maintain stable, efficient ion emission.

Different ionic liquids operate in various regimes, such as the pure ionic regime, where ion emission is highly efficient and produces a high specific impulse, and mixed regimes that may result in lower efficiency due to the presence of droplets. The performance in pure ionic regime (PIR) is favored by liquids with higher surface tension and electrical conductivity, but other factors like viscosity also play a significant role, as it affects the hydraulic resistance and flow rate of the propellant [88]. Propellants like EMI-BF_4 and EMI-DCA, are known for their high conductivity and the ability to operate efficiently in ionic regimes. However, propellants with lower viscosities, may lead to droplet formation,

which reduces efficiency. In contrast, high-viscosity ionic liquids, such as EMI-$EtOSO_3$, show potential to maintain high efficiency in externally wetted emitters due to their ability to limit droplet formation, despite having lower conductivity [88]. Therefore, the careful selection and optimization of ionic liquids are vital to achieve the best possible performance in electrospray thrusters, particularly for small satellite applications. In this thesis, EMI-Im and EMI-BF_4 have been employed mainly for different experimental analysis due to its properties as described in sections 6.1 and 6.2.

Chapter 5

5 Emitter device microfabrication

Silicon based microfabrication has been the fundamental tool for the production of the emitter devices in this Thesis, as the backbone of the thruster. Figure 15 depicts the microfabrication process step-by-step from a bare silicon wafer to the fully functional devices. The fabrication process is organized into three major sections, each corresponding to a critical part of the MEMS device: the emitter array, the wetting system, and the feeding system. Each of these components plays a vital role in the overall performance and functionality of the thruster. The subsequent sections provide a detailed description of the individual microfabrication steps involved in the creation of these structures.

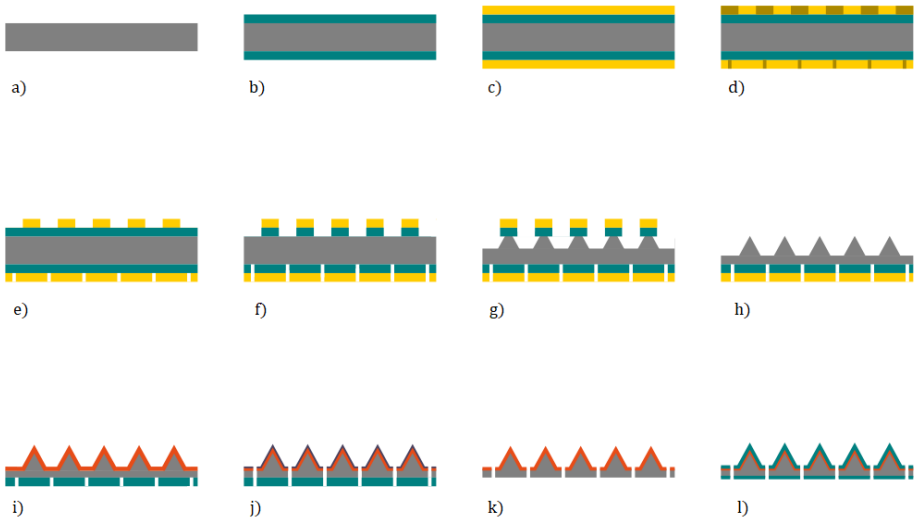

Figure 15: Microfabrication process for electrospray emitters: (a) bare Si wafer; (b) thermal oxidation; (c) photoresist spin-coating; (d) photolithography; (e) mask developing; (f) exposed oxide removal by RIE; (g) isotropic dry Si etching; (h) upper mask removal and needle sharpening; (i) photoresist removal and colloidal self-assembly; (j) anisotropic RIE etching to form nanowires and Al mask sputtering; (k) feeding holes etching and protecting Al mask removal; (l) thermal oxide protective layer growth.

5.1 Fabrication of the emitter array

The emitter array is composed of a matrix of microconical structures designed to generate the high electric fields required for particle emission. The fabrication of these structures relies on microfabrication techniques capable of transforming a planar silicon surface into precisely defined needle-like geometries. In this work, two distinct approaches were explored to achieve this transformation, each offering unique advantages and limitations: isotropic reactive ion etching (RIE) and wet chemical etching.

The isotropic RIE uses a chemically reactive plasma to etch and sculpt the silicon mironeedles. This technique has been extensively used throughout this thesis to produce functional devices, demonstrating its effectiveness in achieving sharp and well-defined structures. However, as will be discussed in this section, isotropic RIE poses challenges in maintaining homogeneity across large areas, which can impact device performance. To address these challenges, wet chemical etching using potassium hydroxide (KOH) was investigated as an alternative. Although the KOH etching method enabled the successful fabrication of emitter arrays, further refinement and optimization will be pursued in future research to fully integrate it into the device fabrication workflow.

5.1.1 Wafer conditioning

Proper wafer preparation and cleaning are critical steps before any cleanroom fabrication process. Surface contaminants, including organic residues, metal ions, and particulates, can significantly impact device performance, leading to defects, poor adhesion, and variability in processing outcomes. To ensure high-quality fabrication, wafers must undergo rigorous cleaning and conditioning procedures to remove these contaminants and prepare the surface for subsequent processing.

Before the lithography itself, the wafers undergo RCA cleaning protocol to eliminate organic, ionic, and particulate contaminants. This multi-step cleaning process includes Standard Clean 1 (SC-1), which uses a mixture of ammonia and hydrogen peroxide, Stan-

dard Clean 2 (SC-2), involving hydrochloric acid and hydrogen peroxide, and a final rinse in deionized water. After cleaning, as shown in Fig. 15b, the wafers are oxidized via a wet oxidation process in furnaces at a temperature of 1100°C for a specified duration to achieve the desired oxide thickness. For the devices produced in this work, oxide thicknesses of 1.5 μm and 2 μm were used, depending on the specific purpose, whether for RIE or KOH etching. The primary role of silicon oxide grown through the described process is to act as a hard mask, protecting the silicon substrate during etching process. This protective layer enables the precise shaping of silicon according to the desired patterns, ensuring accuracy and structural integrity throughout the fabrication process.

5.1.2 Photolithography and pattern transfer

Photolithography serves as the initial stage in the microfabrication process for emitter devices, translating designs into physical patterns on the silicon wafer. This process begins with the design of photolithography masks, which are generated using Computer-Aided Design (CAD) software. These masks, typically fabricated in quartz substrates for precision, provide the templates for pattern transfer. For prototypes or designs with less stringent tolerances, polymer masks may also be employed due to their cost-effectiveness. Due to the large size of the structures, polymer masks have been used throughout this thesis.

The photolithography process begins by coating the oxidized wafer with a light-sensitive photoresist (Fig. 15c). Prior to this, an O_2 plasma treatment is applied to the wafer surface to enhance photoresist adhesion. A positive resist, HiPR 6512, is uniformly spin-coated onto both sides of the wafer and soft-baked at 80°C in alternating steps to remove residual solvents. The process is followed by the step shown in Fig. 15d, where the wafer is placed in a FL10 Karl Süss Microtec MA6/BA6 mask aligner, shown in Fig. 16, where UV light is used to expose the resist through a carefully aligned photomask. This exposure transfers the designed pattern onto the photoresist layer.

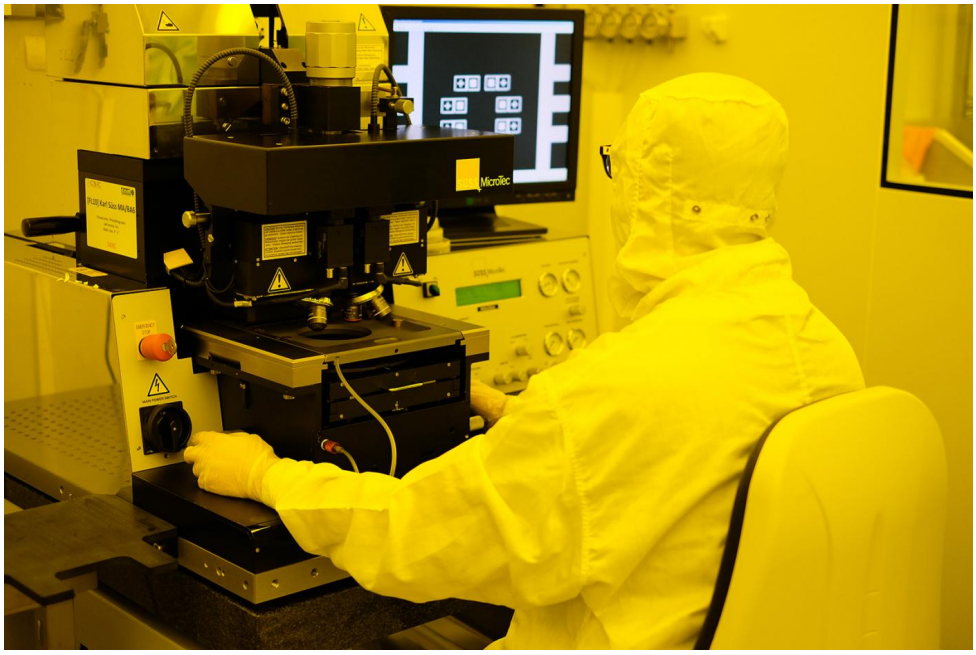

Figure 16: FL10 Karl Süss Microtec MA6/BA6 mask aligner sourced from IMB-CNM-CSIC platform.

Next to exposure, the wafer is developed using OPD4262 developer, which removes the exposed photoresist, leaving the desired pattern intact (Fig. 15e). This process is repeated for the opposite side of the wafer to expose the oxide layer on both surfaces for subsequent etching steps. To ensure the durability of the patterned photoresist during etching, a hard bake is performed at 115°C in an oven.

Next, the exposed oxide mask is etched away, exposing the underlying silicon. To do so, the wafer is immersed in a bath of Buffered Oxide Etchant (BOE) 7:1, a buffered mixture of diluted hydrofluoric acid (HF) to selectively etch silicon oxide without affecting other materials, such as photoresist. The etch rate of BOE is approximately 80 nm/min at room temperature (RT) conditions [89]. Following chemical etching, the wafer is rinsed in deionized water to remove BOE residues, leaving the silicon exposed and ready for further etching of emitter structures.

The combination of photolithography and precise pattern transfer establishes the founda-

tion for the subsequent etching processes, ensuring that the fabricated emitter structures exhibit the geometric precision required for optimal performance.

5.1.3 Basics on Reactive Ion Etching

The conical or needle-shape architecture of the emitters can be achieved through various etching techniques, each one defining a characteristic shape of the etched structures. In this thesis, a specific type of dry etching - Reactive Ion Etching (RIE) - has been extensively used as the workhorse.

Dry etching plays a pivotal role in semiconductor and MEMS fabrication due to its ability to precisely pattern silicon substrates. Among the most advanced dry etching techniques is Reactive Ion Etching (RIE), which combines chemical reactions with physical ion bombardment to achieve either isotropic or directional, high-precision material removal. The process takes place in an ultra-high vacuum (UHV) chamber, where a plasma is generated by an RF power source from a low-pressure gas. The plasma consists of ionized gas molecules that interact with the wafer surface through two synergistic mechanisms: chemical reactions between reactive species and the substrate, and physical bombardment by plasma ions.

The physical mechanism of RIE involves the acceleration of plasma ions through strong electric fields. These ions bombard the target surface, breaking chemical bonds in the material, facilitating the chemical reactions between the reactive plasma species and the substrate. The synergy between physical ion bombardment and chemical reactions allows for highly directional and precise etching. The gas composition within the plasma plays a crucial role in determining the etching characteristics, and its selection is tailored to the target material. In MEMS fabrication, three main gas types are commonly employed: SF_6, CF_4/CHF_3, and Cl_2/BCl_3. The first class of gas is primarily used for isotropic etching purposes, as it efficiently generates highly reactive fluorine radicals. Carbon-based gases, are used for etching silicon oxide and nitride due to their fluorine content. Chlorine-based gases, are typically applied for etching metals or certain dielectrics. Appropriate choice

of the gases allows for precise control over etching selectivity and profile.

RIE offers significant versatility, allowing for isotropic or anisotropic etching depending on the process parameters such as gas composition, chamber pressure, and RF power. Isotropic etching removes material uniformly in all directions, often leading to undercutting beneath the photoresist or hard masks and sloped profiles. Prolonged isotropic etching can produce rounded profiles and surfaces with a degree of inclination. Conversely, anisotropic etching achieves vertical sidewalls through directional ion bombardment, crucial for high-aspect-ratio structures like trenches and pillars. Advanced RIE processes, such as Deep Reactive Ion Etching (DRIE), enable the fabrication of these structures and are discussed further in section 5.2.

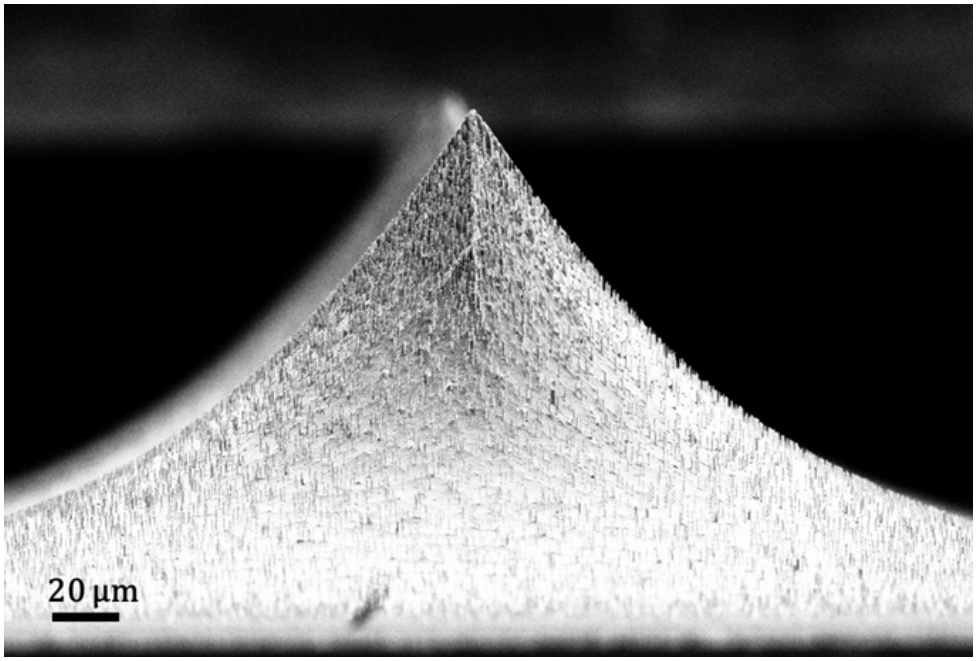

Figure 17: SEM image of a sharp microneedle showcasing a steep slope, a characteristic feature of the isotropic reactive ion etching process.

RIE holds significant potential, offering highly precise etching control through fine-tuning of process variables. Additionally, it is highly versatile, allowing the etching of various materials. However, one of the main drawbacks of RIE is the complexity of the system, as it requires meticulous control over numerous parameters to balance etch rate, selectivity,

anisotropy, and substrate integrity. Another major limitation is the uniformity of the etching process, as achieving homogeneity across large substrates can be challenging due to variations in plasma density and ion distribution. Moreover, prolonged etching can induce surface defects, which may be problematic for specific applications. Despite these challenges, RIE remains a cornerstone in modern microfabrication, offering the ability to create complex, highly precise features across a range of materials.

5.1.4 Basics on wet etching

Wet etching is another fundamental technique in silicon based microfabrication, widely used in semiconductor processing to selectively remove material from substrates. Unlike dry etching, which relies on plasma-based processes, wet etching achieves material removal through purely chemical reactions between the substrate and a liquid etchant. Similar to dry etching, wet etching can be classified into isotropic and anisotropic categories, depending on the etchant's interaction with the substrate.

In isotropic wet etching, material is removed uniformly in all directions, originating rounded or sloped profiles. While this uniformity can be advantageous for specific applications, it also leads to undercutting beneath the masking layer, limiting its suitability for high-precision fabrication. On the other hand, anisotropic wet etching selectively removes material based on the crystallographic orientation of the substrate, often resulting in highly directional etching with well-defined geometries. An example of anisotropic wet etching is the use of potassium hydroxide (KOH) as an etchant for silicon. KOH selectively etches silicon along specific crystallographic planes, enabling the formation of features such as V-shaped grooves and pyramidal pits with high precision. It is particularly effective for structuring well-defined geometries by etching (100) or (110) silicon crystallographic planes and leaving (111) planes. The etch rate along different crystal planes varies significantly, leading to directional etching with minimal undercutting and a characteristic angle of 54.7° between planes.

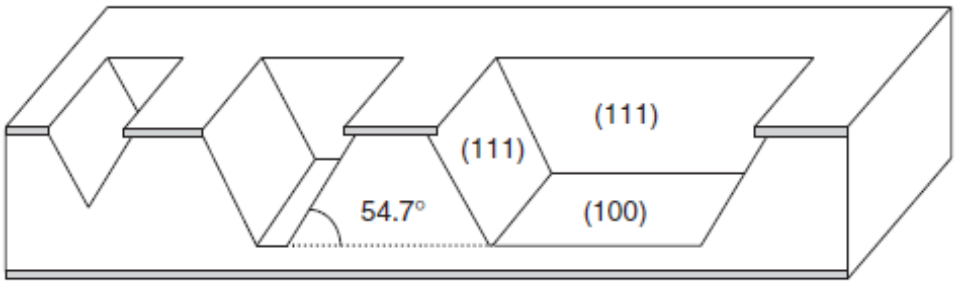

Figure 18: Anisotropic wet-etched profiles in <100> wafer. The sloped sidewalls are the slow etching (111) planes; the horizontal planes are (100). Etching will terminate if the slow etching (111) planes meet [67].

Several parameters and conditions can affect significantly the wet etching process. The selection of the etchant is critical, as it must exhibit selectivity between the material to be etched and any protective layers used to define the pattern. Common etchants include hydrofluoric acid (HF) for silicon oxide, phosphoric acid for silicon nitride, and KOH for silicon. Additionally, factors such as temperature or concentration of the etchant, along with the etching time, must be carefully controlled to achieve the desired etching depth and profile.

Wet etching offers several advantages, including simplicity, cost-effectiveness, and the ability to uniformly process large surface areas. The absence of complex equipment, such as vacuum systems required for dry etching, reduces cost and facilitates scalability. Additionally, wet etching often achieves faster material removal rates, making it ideal for high-throughput applications. However, it has limitations such as achieve the same level of precision and complexity as dry etching, particularly for high-aspect-ratio structures, due to the inherent limitation of chemicals. Isotropic wet etching lacks precision due to undercutting, and anisotropic wet etching is inherently constrained by material properties such as crystallography, limiting its versatility for non-silicon substrates or complex patterns.

To sum up, wet etching remains a valuable tool in microfabrication for its simplicity,

cost efficiency, and effectiveness in removing large volumes of material. While its limitations in precision and structural versatility often lead to a preference for dry etching in advanced applications, wet etching is indispensable for many foundational and large-scale processes in device manufacturing.

5.1.5 Microneedle fabrication based on RIE

Etching techniques often yield similar outputs, despite they differ significantly in their underlying mechanisms, as outlined earlier. In this thesis, the primary etching workhorse has been via Reactive Ion Etching (RIE), which is detailed in the following lines. Additionally, preliminary tests involving potassium hydroxide (KOH) etching are briefly introduced.

Once the SiO_2 mask is patterned, the wafer is placed in the RIE system, specifically an Alcatel AMS-110 DE, which is used in cleanroom facilities. This advanced equipment, shown in Fig. 19, is an automatic single-wafer system that can position the wafer as close as 100 mm to the plasma. It is equipped with two power sources: an Inductively Coupled Plasma (ICP) generator and a Radio Frequency (RF) generator, each serving distinct purposes. The ICP generator is responsible for generating a high-density plasma by ionizing gases, which enhances the reactivity of the species in the plasma. The RF generator, on the other hand, applies a bias to control the energy of these species, affecting both the direction and rate of etching. Typically, the RF generator is employed only for anisotropic etching processes, such as the Bosch process used for the nanowires discussed in section 5.2.2. Additionally, the wafer is placed on a temperature-controlled chuck, which maintains the desired thermal conditions through an integrated chiller system. A continuous flow of helium ensures efficient thermal contact, while the pressure is carefully regulated to optimize temperature transfer and maintain process stability.

Figure 19: Alcatel AMS-110 DE dry etcher sourced from IMB-CNM-CSIC platform.

In the isotropic etching procedure, the plasma is generated by introducing sulfur hexafluoride (SF_6) at a flow rate of 150 sccm. The plasma is formed in a chamber maintained at a pressure of 10^{-5} mbar, with 2000 W generated by the ICP power source. The wafer is positioned on the chuck 160 mm away from the plasma, with helium pressure set at 10^3 Pa and a temperature of 20°C. The plasma species isotropically etch the silicon for a duration of 1 hour, 7 minutes, and 15 seconds, forming the base of truncated conical structures with a diameter of 100 μm (Fig. 15g, 20). The structures' dimensions are measured using an electron microscope or confocal microscope, focusing on the circular patterns used as masks.

Next, the structures are sharpened to create the emitters for the device. To do so, firstly, the RIE system is used to generate an oxygen (O_2) plasma at 2500 W, with a flow rate of 600 sccm, to remove the photoresist mask and expose the oxide layer. The silicon oxide is then removed using BOE, leaving the silicon surface fully exposed.
Finally, the wafer undergoes another RIE step, Fig. 15h, under identical conditions but for a shorter duration. This second etching step transforms the truncated cones into needle-like structures, creating emitters with tunable angles. As the trunk diameter de-

creases, the etch rate in these areas increases, making etching time a crucial parameter to control. Depending on the duration of etching, the structures can have either a sharper or more obtuse angle.

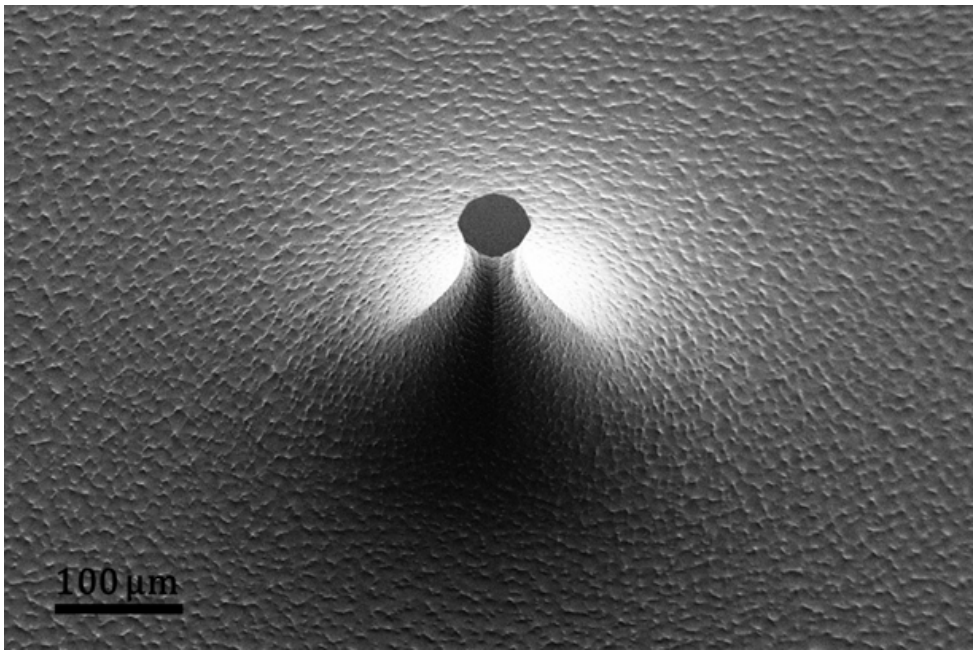

Figure 20: SEM image of a truncated microneedle prior to the sharpening process using isotropic dry etching.

The semi-angle of the microneedles is directly influenced by the etching time. Longer etching times produce less inclined surfaces (lower tip angles) and reduce the height of the structures. Conversely, shorter times yield sharper angles with taller emitters. The optimal semi-angle is key to optimize the emission parameters, and to maximize their emission efficiency. These data are analyzed in section 6.1, where the emission profile is studied as a function of the emitter angle. To study the optimization of the emitter structure geometry, different emitter angles were analyzed. This was achieved by varying the etching times during fabrication. To investigate the effects of different geometries, emitters with semi-angles of 20° and 35° were fabricated, requiring etching times of 15 minutes and 37 minutes and 30 seconds, respectively, to sharpen the microneedles. The resulting emitter heights corresponding to these angles were 215 and 180 μm, respectively.

The structures with a semi-angle of 30° have demonstrated that these parameters are optimal for ensuring proper emitter efficiency without excessively compromising the integrity of the structures, as it is shown in Chapter 6.

5.1.6 Microneedle fabrication based on KOH wet etching

The KOH etching process involves immersing the wafer in a KOH bath to anisotropically etch the crystalline planes and form cones. This type of etching has been investigated for its advantages over RIE, such as improved uniformity of the structures across the wafer and simpler fabrication of emitters due to the simpler infrastructure of the process. Additionally, since it is a bath-based technique, it allows for the fabrication of multiple wafers in a batch, reducing production costs. The uniformity of the structures across the wafer can be enhanced by adjusting the KOH solution concentration and bath temperature [90]. However, lower temperatures and concentrations result in a decreased etch rate.

The KOH etching process employed is an early-stage method for fabricating devices through wet etching. Although briefly explored in this thesis, it will be developed further in future research. The KOH etching uses a typical concentration of 30% and a temperature ranging between 45 to 60 °C, depending on the size of the pattern. A photolithographic process is used to define the silicon oxide mask, 2 μm thick with circular patterns, is designed to eliminate the need to align the mask with the crystalline planes of the wafer, simplifying the fabrication process. After pattern transfer by wet etching with BOE, the photoresist is removed to avoid contamination, and the wafer is immersed in KOH under the desired conditions. KOH etches the silicon surface while the oxide mask defines the emitter geometry.

The resulting emitter angle is determined by the silicon's crystalline structure, with characteristic 54.7° angle between the etched (111) planes. The height of the emitters is primarily limited by the initial size of the SiO_2 pattern, and the durability of the oxide mask, which etches significantly slower than silicon. Once the oxide mask is fully consumed, the emitter structure becomes sharper.

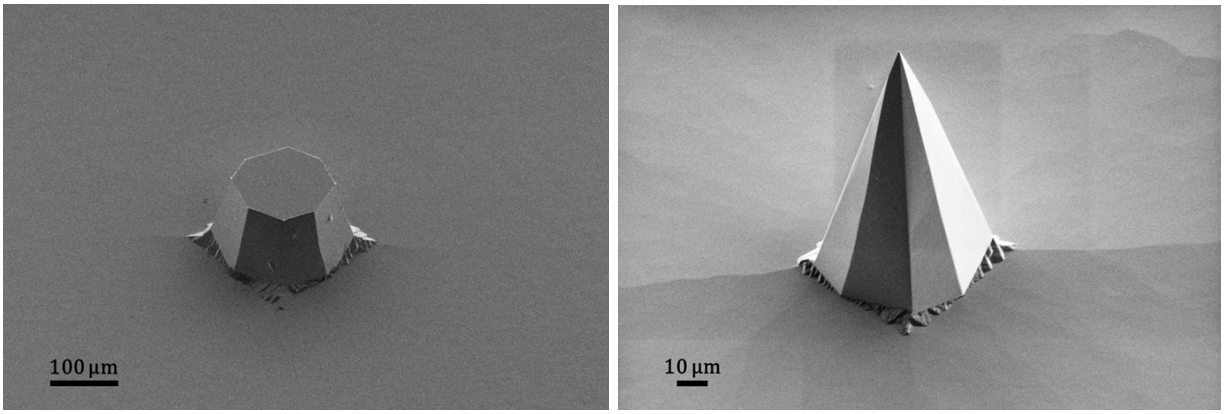

(a) Silicon truncated needle (b) KOH sharpened needle

Figure 21: SEM images of (a) a truncated microneedle during KOH wet etching and (b) a microneedle after KOH wet etching process, showcasing the characteristic crystalline plains etching.

The process concludes with a rinse in a water bath to remove excess KOH, followed by a brief immersion in hydrochloric acid (HCl) to eliminate potassium salts formed during etching.

5.2 Externally wetting system through nanowires

Following the sharpening of the emitter structures, the wafers containing the devices are ready for the integration of an array of nanowires in thw whole 3D surface, which form the propellant transport network, by colloidal lithography.

This section explores the physics and processes underlying colloidal lithography (Fig. 15i), emphasizing its suitability for patterning complex three-dimensional substrates, such as conical structures, where conventional techniques are not scalable. Colloidal lithography offers a robust and adaptable approach to achieving homogeneous nanoparticle assemblies over large areas, providing precise control over pattern density through tunable parameters such as particle concentration and deposition conditions.

The discussion focuses on positively charged amidine latex beads, chosen for their elec-

trostatic attraction to the negatively charged silicon oxide surface, and examines the key forces governing particle self-assembly, including electrostatic interactions, Van der Waals forces, and capillary effects, as well as practical considerations for optimizing pattern uniformity and reproducibility.

5.2.1 Colloidal Lithography

Colloidal lithography is a versatile and cost-effective nanofabrication technique based on the self-assembly of colloidal particles onto a substrate. By employing colloidal particles, typically nanospheres made from materials such as polystyrene or silica, this method enables the creation of nanoscale patterns over large areas without the need for expensive equipment. The particles act as a physical mask during subsequent etching or deposition processes, yielding structures with precise nanoscale features.

The colloidal lithography process begins with the preparation of a colloidal suspension, consisting of nanoparticles diluted in deionized water. In this study, 4% Amidine Latex Beads (0.5 μm diamter, ThermoFisher) were used due to their superior charge properties, uniform dispersion, and ease of removal compared to other types of beads. These particles are deposited onto the substrate through techniques such as spin-coating or drop-casting [91–94]. Once deposited, the particles electrostatically self-assemble into a monolayer, forming the pattern for further etching or deposition processes.

The stability and uniformity of the colloidal particle arrangement are governed by the electrostatic interactions between the particles and the substrate. These interactions are quantified by the zeta potential (ζ-potential), a measure of the electrostatic potential at the slipping plane, where the stationary fluid layer around a particle transitions to bulk fluid. A high ζ-potential indicates strong repulsive forces between particles, which helps prevent aggregation and ensures uniform particle distribution. In aqueous suspension, amidine latex beads acquire a positive surface charge due to the dissociation of positive functional groups on their surfaces. This charge interacts with ions in the solution, forming an electrostatic double layer around each particles [95–97]. The ζ-potential reflects

the strength of this electrostatic interaction, which can be modified by adjusting the ionic strength of the solution and the pH.

The decay of electrostatic interactions with the distance is determined by the Debye length, defined as:

$$\kappa = \sqrt{\frac{2e^2 I}{\epsilon k_B T}} \tag{5.1}$$

where e is the elementary charge, I is the ionic strength of the solution, ϵ is the permittivity of the medium, k_B is the Boltzmann constant and T the temperature. Equation 5.1 demonstrates that electrostatic interactions decay exponentially with distance, therefore the force between a particle with effective charge q and a substrate with surface potential ϕ at distance r can be approximated as:

$$F = \frac{1}{4\pi\epsilon}\frac{q\phi}{r^2} \tag{5.2}$$

In addition to electrostatic forces, Van der Waals interactions play a critical role in self-assembly processes, especially at short distances. These attractive forces arise from transient dipole interactions described for a particle of radius R interacting with a planar substrate as:

$$F_{VdW} = \frac{A}{6}\frac{R}{D^2} \tag{5.3}$$

where A is the Hamaker constant and D is the gap between the particle and the surface. This type of interaction counterbalance electrostatic repulsion, influencing the final arrangement and stability of particles on the substrate.

The self-assembly of colloidal particles onto a substrate is defined by a Brownian motion, driving particles to diffuse through the suspension. The diffusion flux of particles

towards the substrate is defined by Flick's first law as:

$$J = -D\frac{\partial c}{\partial x} \tag{5.4}$$

being D the diffusion coefficient, c the particle concentration and x the spatial coordinate. For spherical geometries in a solution, D is given by the Stokes-Einstein equation:

$$D = \frac{k_B T}{6\pi\eta R} \tag{5.5}$$

where η is the viscosity of the solution and R the radius of the particles. Hence, from equation 5.5 is possible to infer that smaller particles diffuse faster than larger ones, enabling efficient self-assembly and uniform deposition.
As discussed above and in section 2.2, optimizing the system parameters is crucial for achieving maximum performance. Various concentrations of nanoparticles were tested to identify the appropriate hydraulic resistance values for the target performance. These specific values remain confidential, as they form part of the proprietary knowledge of the company involved in this research. However, the general behavior of system efficiency as a function of hydraulic resistance is briefly covered in Section 6.1.

Colloidal particles self-assembly on a solid substrate is mainly driven by electrostatic interaction, so to enhance the attraction between positively charged amidine latex beads and the negatively charged substrate, surface activation is required. Surface activation can be achieved through either physical or chemical methods. Physical activation involves bombarding the wafer with negative oxygen ions in an oxygen plasma, charging the surface via Coulombic interactions. Chemical activation, on the other hand, employs chemical reactions to generate surface charges on the silicon surface through ionic bonds.

The colloidal self-assembly was found to be highly dependent on the activation and drying methods used. The results of various surface activations are shown in Fig. 22. Plasma activation resulted in fewer particles adhering to the surface compared to chemical activa-

tion methods, due to the weaker Coulombic interactions in plasma treatment compared to the stronger ionic bonds generated in chemical activation. Different plasma conditions, such as power and time, were tested without significant changes in particle assembly, prompting a shift towards chemical activation methods, which showed greater success.

The selected chemical activation methods were the Piranha solution, a mixture of H_2SO_4 and H_2O_2 (2:1), and Stage 1 of the RCA cleaning process, which consists of a mixture of H_2O, NH_4OH, and H_2O_2 (5:1:1) at 70°C. Both solutions oxidize the surface of the silicon and generate negative ions. The Piranha solution generates a highly aggressive, exothermic reaction that excessively oxidizes the silicon surface, limiting the formation of ionic bonds. In contrast, RCA Stage 1 produces a milder oxidation, resulting in more ionic bonds and a more effective surface activation [98].

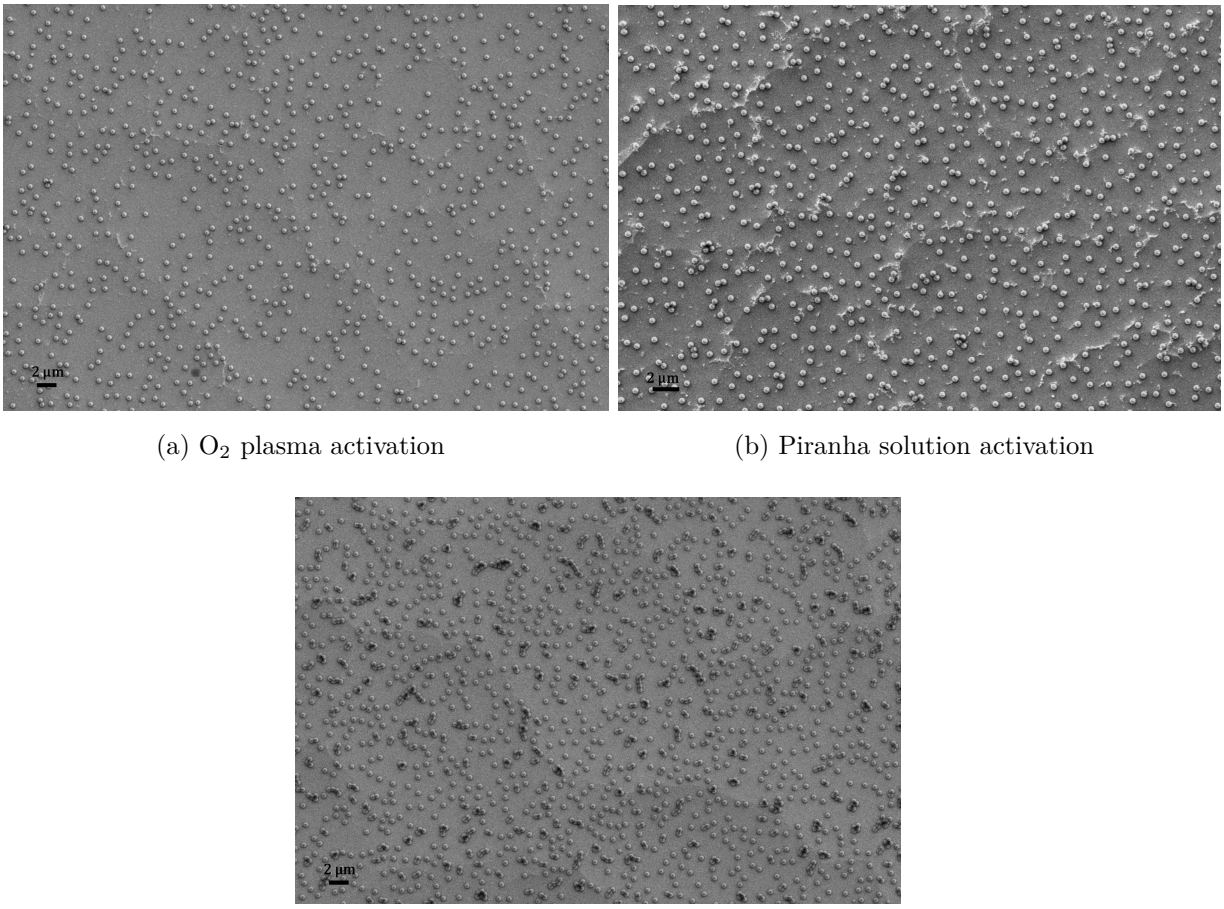

(a) O_2 plasma activation

(b) Piranha solution activation

(c) RCA SC1 activation

Figure 22: Comparison of nanoparticles density (NPs/μm^2) over silicon substrates using the same particle dilution and drying method (Room Temperature), employing different surface activation methods: (a) O_2 plasma activation (ρ = 0.37 ± 0.07), (b) Piranha solution activation (ρ = 0.62 ± 0.02) and (c) RCA SC1 mixture activation (ρ = 0.64 ± 0.02).

The RCA SC1 chemical activation process lasts for 15 minutes, followed by a 4-minute rinse in a deionized water bath. The wafer is then dried using a nitrogen gun. Once dried, the wafer is placed on a flat surface, and the nanoparticle suspension is casted onto it, covering the emitter structures. The colloidal particles are allowed to self-assemble for 20 minutes before being rinsed to remove any unassembled particles from the surface.

Once particles are deposited on the substrate, a drying process is required. This pro-

cess is critical, as it determines the final arrangement of the beads. As the liquid media evaporates, capillary forces arise due to surface tension, pulling particles closer together:

$$F_{capillary} = 4\pi\gamma R\cos(\theta) \tag{5.6}$$

where γ is the liquid surface tension R the radii of the sphere and θ is the contact angle of the liquid on the particle surface. Generally, these forces are attractive, potentially originating particle displacement or clustering under non-uniform drying conditions.

Controlled drying methods are required to mitigate such effects. Different drying methods were performed in the fabrication of these devices, such as drying under room temperature (RT) conditions and the Critical Point Dryer (CPD) technique. RT drying was extensively used and improved during the establishment of the device fabrication process. This method involves allowing the wafer to air-dry naturally after the final rinse in deionized water. Over time, improvements were made by adjusting parameters such as wafer tilt, drainage flow, and shielding with Pyrex wafers to prevent turbulence. Although homogeneous distributions were sometimes achieved, RT drying suffered from clustering and reproducibility issues between batches, making it less ideal.

On the other hand, CPD technique significantly improved reproducibility and maintained system uniformity. This equipment prevents structural irregularities caused by surface tension by eliminating the liquid-to-gas phase transition. During conventional drying, this transition creates capillary forces that pull particles together, often leading to deformation or collapse of the nanoparticle arrangement. By transitioning the liquid into a supercritical state, where there is no distinct liquid or gas phase, the critical point dryer removes these forces, preserving the integrity and uniformity of the structure. The CPD process begins by replacing the water in the sample with isopropyl alcohol (IPA), which is miscible with both water and liquid CO_2. The wafer is immersed in IPA, and liquid CO_2 is introduced to replace the IPA through multiple flushes. The system then heats and pressurizes the CO_2 beyond its critical point, where it exists as a supercritical fluid,

neither liquid nor gas, eliminating surface tension. Finally, the CO_2 is slowly vented, leaving the wafer dry and intact.

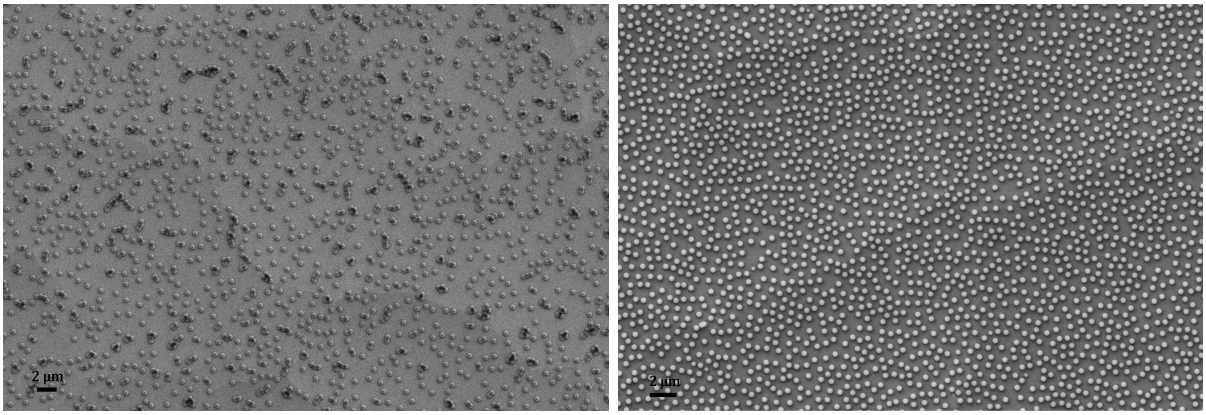

(a) Room Temperature drying (b) CPD drying

Figure 23: Comparison of silicon substrates after different drying procedures in a self-assembly process using the same particle dilution and activation through RCA SC1: (a) substrate dried at Room Temperature conditions and (b) substrate dried using Critical Point Dryer process.

Figure 23 shows the impact of the drying method on the substrate, obtaining a highly homogeneous distribution through the use of CPD drying. After the drying, wafers undergo a thermal treatment to partially melt the colloidal particles. The wafers are placed on a hot plate at 125°C for 5 minutes. This step improves adhesion of the colloids to the substrate, by increasing the contact area, and prevents disassembly and underetching during subsequent Bosch process steps.

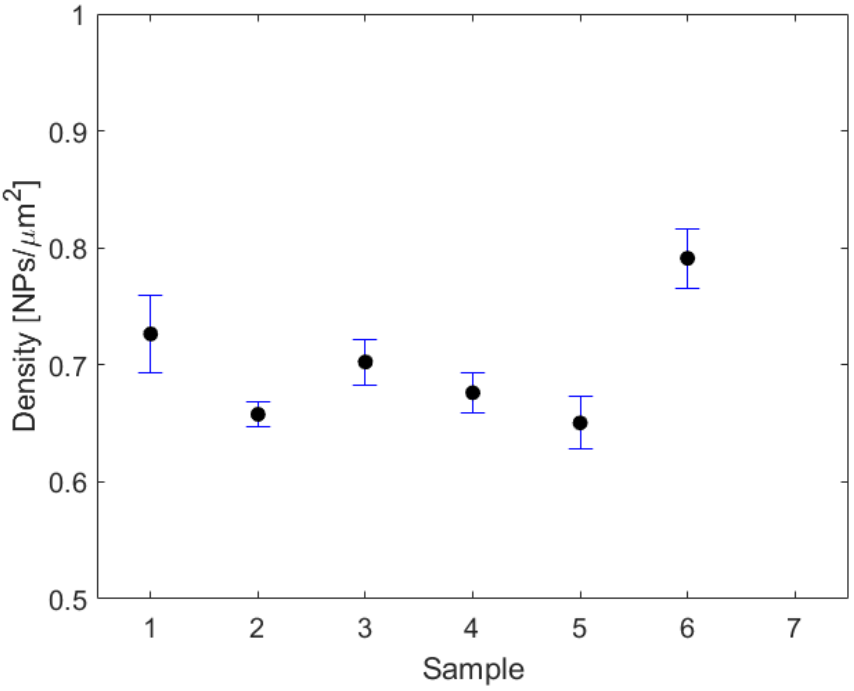

Figure 24: Nanoparticle density measurements across different samples to assess the homogeneity of the process. Each data point represents the average surface density of nanoparticles (NPs/μm^2) measured on an individual sample, with error bars indicating the standard deviation. The consistent values across samples suggest a uniform deposition process, highlighting the effectiveness of the critical point dryer in maintaining process reproducibility.

Figure 24 illustrates the density of nanoparticles, in units of NPs/μm^2 across multiple batches of wafers, with the objective of evaluating the repeatability of the nanoparticle self-assembly process. The density range for a particle dilution can be observed across the batches, suggesting a degree of variability in the process due to self-assembly challenges, such as surface activation inconsistencies and high particle concentration. The densities span from approximately 0.67 to nearly 0.8 NPs/μm^2. This analysis highlights the importance of understanding and controlling process conditions to achieve consistent nanoparticle densities, a critical factor for applications requiring precision and uniformity.

5.2.2 Fabrication of Silicon nanopillars: Bosch process

The Bosch process is a cornerstone technique in Deep Reactive Ion Etching (DRIE), essential for fabricating high-aspect-ratio microstructures in silicon (Fig 15j). It allows for the precise etching of vertical features, such as deep trenches or high pillars, which are integral to the development of intricate microdevices. The Bosch process achieves this by employing a unique cyclic methodology that alternates between two phases, isotropic etching and sidewall passivation, to produce highly anisotropic etch profiles, for creating, vertical structures with minimal lateral etching [99, 100].

The first phase of the cycle is the etching step, generating a plasma of sulfur hexafluoride (SF_6). The plasma dissociates SF_6 molecules, generating fluorine radicals, which aggressively react with the silicon surface to form volatile compounds like silicon tetrafluoride (SiF_4). This reaction predominantly etches the silicon isotropically, removing the silicon in all directions. However, without further intervention, this would lead to unwanted lateral etching, reducing the precision of the microstructures.

To mitigate this, the second phase is the passivation. A plasma of fluorocarbon gas, typically C_4F_8, is used to deposit a thin polymer layer on the exposed surfaces of the silicon. This polymer layer is crucial for protecting the sidewalls of the etched features from further lateral etching due to fluorine. The polymer coats the vertical surfaces, preventing the etching species from attacking the sidewalls while still allowing vertical etching to continue in subsequent cycles.

By alternating between these etching and passivation steps, a high anisotropic etching is achieved, where the vertical etching rate is significantly higher than the lateral etching rate. This results in the formation of deep, well-defined features with near-vertical sidewalls. The nature of the shifting process also introduces a characteristic scalloped pattern on the sidewalls, caused by the periodic deposition and removal of the passivation layer. However, the size and frequency of these scallops can be minimized through careful optimization of process parameters such as gas flow or plasma power.

The wafers coated with melted nanospheres are subjected to a Bosch process using the same etching equipment as that employed for the emitter structures. The wafer is placed on the chuck at a distance of 120 mm from the plasma, where the wafer is cooled to 0°C at helium pressure of 10^3 Pa. The chamber operates under high vacuum conditions, similar to those used during the fabrication of the previously made structures. A 2000 W power source generates the plasma. Prior to loading the sample, the chamber is conditioned by briefly introducing the gases used in the etching process.

Before the Bosch process begins, a priming step is performed, where the process gases briefly enter the chamber to stabilize the environment and ensure consistent etching conditions. Once the wafer is introduced, the Bosch process alternates between two gases, initially introducing C_4F_8 for 1 second, followed by SF_6 for 2 seconds. The C_4F_8 is introduced at a flow rate of 300 sccm and a pressure of 3 Pa, while SF_6 is supplied at 200 sccm and 5 Pa. During the Bosch process, a radio-frequency (RF) generator is employed to control the directionality of the etching. The plasma operates at a frequency of 280 kHz, with a high power setting of 80 W for 10 ms, alternating with a low power setting of 0 W for 90 ms.

The morphological characteristics of the structures are controlled by the number of cycles, with each cycle representing the total time for the gases involved. In this specific case, a complete cycle lasts 3 seconds. The structures produced for the devices have a height of 3 μm, achieved after 20 cycles, consistent with the design requirements for the propulsion system. Additionally, these structures exhibit a diameter of approximately 0.5 μm, determined by the size of the particle acting as the mask. However, slight variations in this result may occur due to underetching effects.

Throughout the development of these nanostructures, fine-tuning of different key parameters of reactive ion etching (RIE) is crucial to achieving precise and well-defined etch profiles. The gas flow rate controls the supply of reactive species, balancing chemical and

physical etching. Too much gas can cause excessive lateral etching, while too little may lead to incomplete reactions and uneven surfaces. Chamber pressure influences how ions travel within the plasma—lower pressures create highly directional ion bombardment for clean, vertical etching, while higher pressures increase collisions, making the etching more isotropic. The distance between the plasma and the wafer affects how the ions interact with the surface. A shorter distance results in higher-energy ion bombardment, increasing the etch rate but also the risk of damage, whereas a greater distance ensures more uniform etching but slows the process down. RF power, which controls the energy of the ions, is another critical factor. Higher power helps achieve sharp, vertical features but can also lead to surface roughness or unwanted heating effects. Since all these parameters are deeply interconnected, even a small adjustment can significantly change the outcome, making precise control essential to creating the desired nanostructures without defects.

The detailed process was carried out using the Alcatel AMS-110 DE. However, the etching process was also characterized and established for an alternative equipment, the Sentech Si 500, providing a backup for nanowire production. The results obtained from the Sentech Si 500 were very similar, as shown in Figure 25. Nevertheless, the Sentech Si 500 was not used for the development of the emitter structures, as access to this equipment was delayed. Although well-defined cones were produced, imperfections were observed across the wafer surface, which hindered the continuation of fabrication. Dry etching equipment is extremely sensitive, and the same protocol cannot be universally applied. The conditions in the Sentech Si 500 differ from the previous system, as parameters such as the wafer-to-plasma distance cannot be adjusted. Unlike the previous equipment, the Sentech Si 500 does not include a priming stage. The C_4F_8 is introduced for 1 second at a flow rate of 300 sccm, while SF_6 is supplied for 1.8 seconds at a flow rate of 150 sccm.

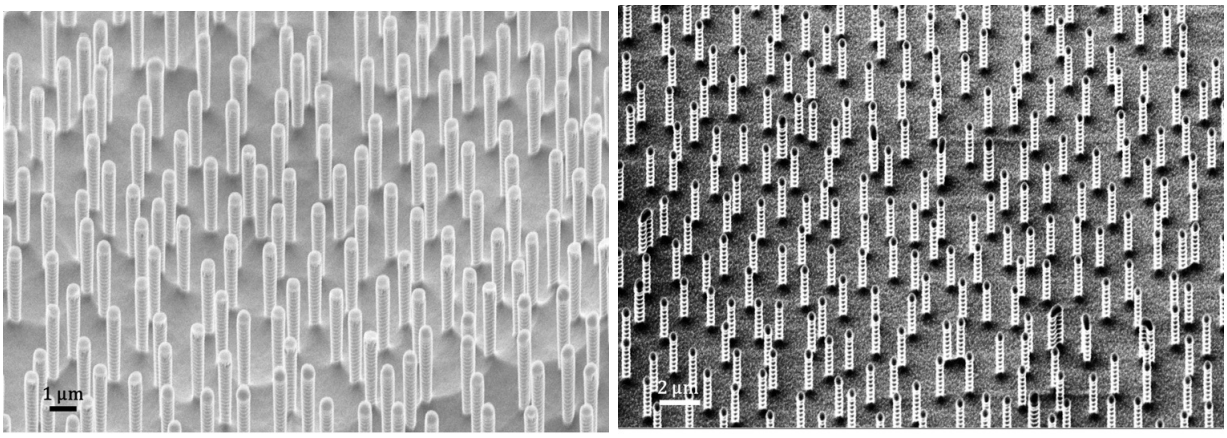

(a) Alcatel AMS-110 DE (b) Sentech Si500

Figure 25: Comparison of silicon nanowires etched using (a) Alcatel AMS-110 DE and (b) Sentech Si500 dry ecthers, employed in the propellant transport network. These nanowires were synthesized from nanoparticles assembled via colloidal lithography.

After etching the propellant transport network, the wafer is subjected to a low-power O_2 plasma. This step removes any residues deposited during the Bosch process passivation, as well as any remaining particles used as the mask.

5.3 Feeding system

At this stage, the devices are in the final phase, where the propellant channels leading to the wafer's active surface are integrated (Fig. 15k). Since the pattern to be etched is on the backside of the wafer, the side containing the previously etched structures is protected with a 1 μm layer of aluminum. Nonetheless, its main function is to serve as an etching stopper due to its selectivity.

The aluminum is deposited using a process called sputtering, a type of Physical Vapor Deposition (PVD) characterized by the use of high-energy plasma, typically composed of argon ions. These accelerated ions collide with the aluminum target, causing the ejection of aluminum atoms. The ejected atoms travel through the chamber and deposit onto the wafer surface, forming a uniform film. The uniformity of this layer depends on parameters

such as plasma power, argon pressure, and others. In the equipment used (KENOSISTEC KS800HR), plasma is generated at 1000 W to deposit 1 μm of aluminum in 15 minutes.

Following this, the wafer is reintroduced into the AMS-110 DE to etch the side of the wafer where the open-hole pattern is exposed in the oxide. The process used is the Bosch process, as it requires etching through the wafer with an anisotropic pattern. The recipe involves first introducing C4F8 at 150 sccm and 2.5 Pa for 2 seconds, followed by SF_6 at 300 sccm and 4.5 Pa for 7 seconds. The plasma, generated by Inductively Coupled Plasma (ICP), operates at 2000 W, while the RF generator uses a frequency of 310 kHz, with a high power setting of 30 W for 10 ms, alternating with a low power setting of 0 W for 90 ms. The recipe positions the wafer 160 mm from the plasma at 20°C, with helium introduced at 600 Pa. The helium pressure is reduced due to the wafer's thinness after such extensive processing, as higher pressure could risk breaking the wafer. This stage of the Bosch process lasts approximately 25 minutes, enough time to etch through the wafer.

The etching process is complete when aluminum is visible through the propellant feeding holes. At this point, the wafer is finished, although the materials used as the hard mask or etch stopper still need to be removed. To eliminate the aluminum layer, a mixture of phosphoric acid (H_3PO_4), acetic acid (CH_3COOH), nitric acid (HNO_3), and water is typically used. This reaction can occur at room temperature or between 40-50°C, with an etch rate of 50-100 nm/min. Due to the hazardous nature of these chemicals, a commercial preparation, TechniEtch Al-80, was used. This mixture was applied at 45°C for 7 minutes, ensuring the removal of the aluminum with slight overetching, as the structural integrity of the devices was not compromised. The wafer is then thoroughly rinsed with water, as the etchant is highly viscous, requiring careful removal. Before removing the remaining SiO_2 on the backside, the wafer is dried in an oven to prevent damage to the devices. The wafer is then submerged in HF to remove the oxide, followed by a rinse in deionized water and another drying step in the oven.

5.4 Protective coating

At this point, the fabrication process for the devices is complete, yielding functional emitter systems. However, a final stage is added to the process: the inclusion of a protective dielectric (Fig. 15l). The purpose of this thin layer is to shield the device architecture from degradation during emission, whether due to electrochemical processes or ion impingement, as it is discussed in section 6.2. To achieve this, the wafer is placed in a furnace (Tempress AFK TS-Series V) for thermal oxidation, growing 500 nm of SiO_2. This technique directly affects the nanowires, increasing their diameter by 30-40%, as shown in Fig. 26, due to the lower density of the oxide [101].

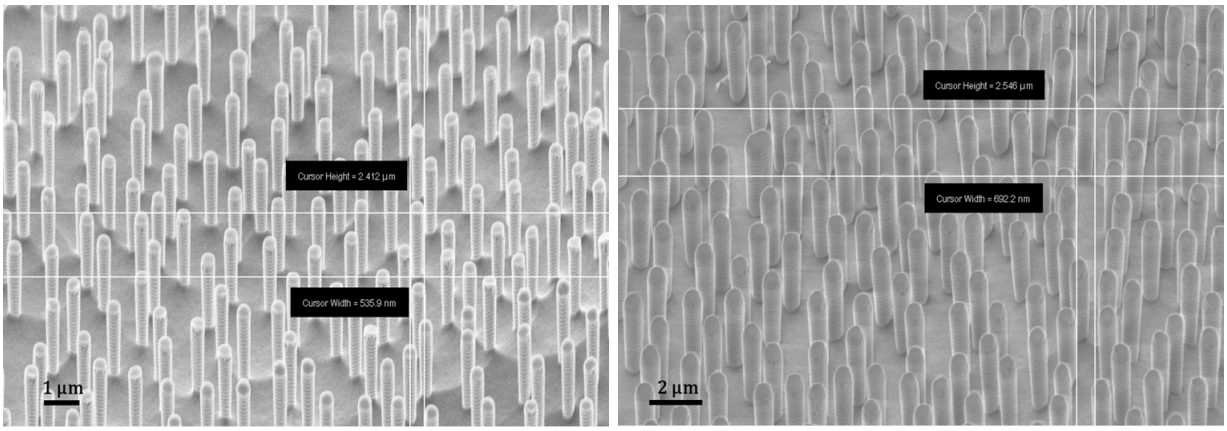

(a) Before thermal oxidation

(b) After thermal oxidation

Figure 26: Comparison of the thickness of silicon nanowires etched using the Alcatel AMS-110 DE dry etcher: (a) before the thermal oxidation process and (b) after thermal oxidation. The increase in thickness after oxidation is evident, attributed to the lower density of the grown oxide.

Chapter 6

6 Thruster perfomance

The performance of a thruster is a critical aspect in evaluating its suitability for specific space missions, encompassing metrics such as thrust, specific impulse, efficiency, and operational stability. These parameters are inherently tied to the design of the propulsion system, the properties of the propellant, and the interplay between the emitter and extractor components. Furthermore, the structural integrity of the device plays a pivotal role; any physical damage or degradation can significantly reduce the efficiency, compromise thrust precision, and shorten operational lifespan. A comprehensive assessment of thruster performance provides insights into the system's capability to achieve precise thrust control, accommodate varying mission profiles, and operate reliably under diverse conditions. In particular, the performance is strongly influenced by the emission characteristics of the ionic liquid propellant, including the regime of operation and the distribution of emitted species. This leads naturally to an exploration of the thruster's emission profile, which details how the beam of charged particles is generated and directed, as well as its impact on overall efficiency and functionality.

6.1 Emission profile

Understanding the physical behavior of the emission profile in electrospray thrusters is essential for optimizing their performance to meet specific requirements. The emission profile provides critical insights into the angular distribution and trajectory of the emitted particles, parameters that are directly related to thrust efficiency, forward momentum, and the overall performance of the device. As discussed in the following sections, deviations from the desired emission angles, such as off-axis emissions, can result in reduced propulsive efficiency, increased energy losses, and accelerated wear on device components. By analyzing this information, design improvements can be identified to mitigate undesirable effects such as overspray or excessive divergence, ensuring longer system lifetime and enhanced effectiveness.

One of the main challenges in electrospray technology is improving beam divergence to

achieve the desired thrust levels while minimizing power consumption, reducing electrode erosion, and increasing efficiency. Uncontrolled beam emission often results in a first-tier failure mechanism known as overspray. Overspray can arise from misalignment of thruster components or emitter geometry, leading to asymmetrical electric fields or non-uniform propellant flows. A common manifestation of the overspray mechanism is off-axis emission, where charged particles are emitted in directions diverging from the intended thrust direction. Minimizing off-axis emissions is therefore critical to maximizing thrust efficiency and extending device lifespan.

Section 2.1.1 has defined the physical principles governing charge emission in electrospray under sufficiently strong electric fields. The field reaches its maximum intensity at a surface with dimensions on the order of tens of nanometers, resulting in highly concentrated field lines at these points. The electric field required to produce emission is achieved through the onset voltage (V_0), expressed in equation 2.20. This parameter, which determines the initiation of the electrospray process, demonstrates that the emitter system performance is significantly influenced by its geometric characteristics and the properties of the propellant.

Electrostatic field equations suggest the use of highly sharp and pointy architectures to reduce the required voltage and maximize particle emission. However, as detailed in Section 6.1.1, these sharp structures can lead to unstable off-axis emissions, resulting in broad emission beams that compromise the efficiency of the device. This section explores the impact of modifying the geometric properties of the emitters, specifically the apex angle, to control and optimize beam behavior. Similarly, the equations presented in Section 2.2 described the behavior of the fluid in relation to the nanowire network across the emitter's surface. Related to this, section 6.1.2 introduces an initial analysis of the beam behavior as a function of the resistance that these nanostructures impose on the flow of the propellant.

6.1.1 Beam angular profile as tip angle function

From physics perspective, sharp microneedles generate electrostatic fields more efficiently by concentrating the field intensity at their tips, thereby significantly reducing the voltage required to initiate emission. However, we hypothesize that in externally wetted structures with very sharp tips, undesirable off-axis emissions could take place even at relatively moderate applied voltages if the emission is produced before the propellant reaches the tip apex, thereby significantly reducing the efficiency.

This hypothesis is based on the extremely high electric field strength concentrated at the tips and the perpendicular alignment of the field lines relative to the conductive surface. As a result, at sufficiently high voltages, emission could be triggered at lower points away from the tip. In such case, field lines would accelerate charges nearly perpendicular to the emitter surface, resulting in wider beams. Furthermore, this hypothesis implies that for a determined high voltage, structures with less steep slopes, characterized by larger apex angles, would produce narrower beams.

To validate this hypothesis, a theoretical model was developed using COMSOL Multiphysics software to analyze the beam emission angle as a function of the emitter angle and the emission point's distance from the apex. This model assumes a perfectly axisymmetric cone with a height of 200 μm and an extractor grid positioned 100 μm away, featuring an aperture radius of 300 μm. The cone's apex angle was varied incrementally from 20° to 40° in 5° steps to observe the trends. For this theoretical analysis, a voltage of 1.6 kV was applied between the emitter and the grid, contributing solely to the particle velocity during the emission.

Potential off-axis emissions were simulated by tracking the trajectories of charged particles ejected from various points along the emitter surface, ranging from 0.5 μm to 5 μm from the tip. Figure 27a illustrates the simulation model for a cone with a specific apex angle emitting from defined points along its surface. The resulting beam behavior is presented in figure 27b, showing the beam divergence (ρ) as a function of the cone's semi-angle for

different emission points from the apex.

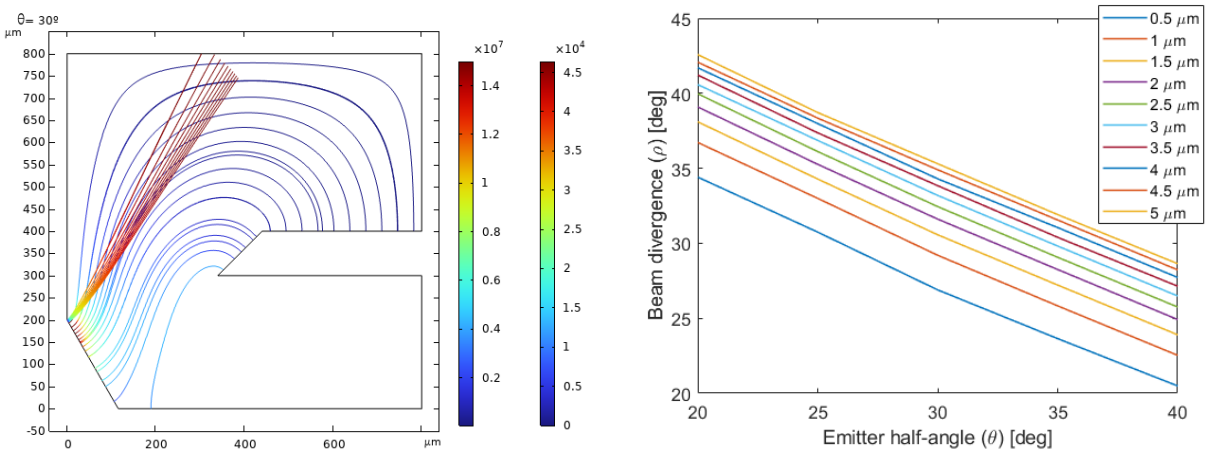

(a) Axisymmetric model

(b) Particle trajectory

Figure 27: (a) Axisymmetric COMSOL model of a 30° half-angle emitter, assuming a voltage difference of 1.6 kV with respect to the grid, showing the field lines perpendicular to the cone surface and the trajectories of the particles that are emitted at different distances from the tip. (b) Angle with respect to the forward direction of the particle trajectory as a function of the cone half-angle and for emission at different distances from the tip.

The trends reveal that for a fixed cone angle, the trajectories of emitted charges exhibit greater divergence as the emission point moves farther from the tip. This increase in the trajectory angle is more pronounced for emission points near the tip and tends to saturate at distances around 5 μm from the apex. Conversely, for a fixed emission point, the beam divergence increases linearly with the emitter's apex angle.

Thus, in very sharp microneedles, the intense electric fields near the tip could prematurely trigger the emission of charged particles before they reach the tip, following trajectories nearly perpendicular to the emitter surface, as hypothesized. Since the electric field intensity is directly influenced by the applied voltage, both the emission position and the particle trajectory angle can be adjusted by varying the voltage, enabling the emission angular pattern fine-tuning. To mitigate these effects, emitters with larger apex

angles are a potential solution. These structures exhibit lower field intensities and lower surface slopes, reducing the risk of premature off-axis emission and enhancing the overall efficiency and stability of the system.

To analyze the off-axis emission phenomenon in electrospray thrusters, arrays with different apex angles were fabricated according to the procedures outlined in section 5. Figure 28 illustrates emitters with apex angles of 35°, 30° and 20°, enabling experimental measurement of beam divergence and comparison with theoretical models. These structures were manufactured with a consistent nanowire density baseline, resulting in a uniform hydraulic resistance of $6{\cdot}10^{16}$ Pa·s/m across all configurations.

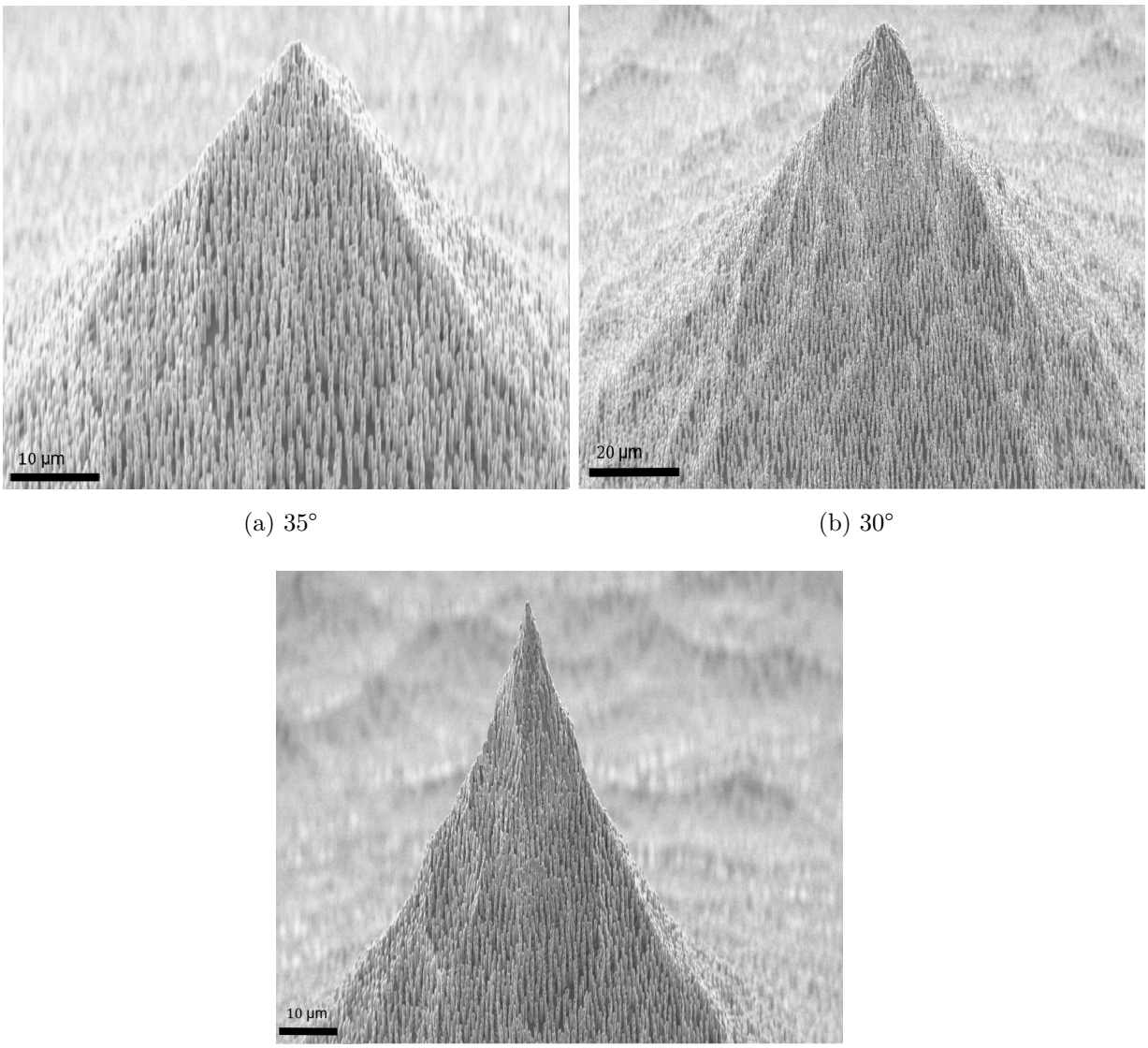

(a) 35°

(b) 30°

(c) 20°

Figure 28: SEM images of the nanostructured microneedles with (a) 35°, (b) 30°, and (c) 20° tip half-angle.

The emitter device was integrated into the modular thruster unit depicted in Fig. 13 and subjected to emission analysis using a Faraday Cup probe. This analysis was conducted in a vacuum chamber featuring a cubic structure with sides of 290 mm and a central extension tube measuring 775 mm in length and 97 mm in inner diameter. The chamber pressure was established below 10^{-5} mbar using an Edwards turbo-molecular pump with an 85 L/s capacity. A cup-shaped electrode, known as the Faraday Cup, was integrated

into the vacuum chamber to measure the angular divergence of the emitted beam. This electrode detects the electric current generated by the emitted species upon colliding its inner collector. Beam divergence data were acquired by placing the Faraday Cup on a rotary stage, enabling its precise positioning at different angles. The current collected at each position provided a spatial distribution of the particle stream and facilitated the analysis of the emission dispersion.

The thrusters were operated over a voltage range, from near onset to breakdown, for both positive and negative polarities. Emitters with larger half-angles, 30° and 35°, were evaluated at applied voltages ranging from 0.8 to 1.8 kV in 0.2 kV increments. In contrast, the emitter with the smallest half-angle, 20°, was tested over a narrower range of 0.6 and 1.3 kV in 0.1 kV steps to enhance accuracy in identifying the onset of off-axis emission. The applied voltage followed a trapezoidal waveform with a 1 s period. Although the voltage waveform was symmetric for both polarities, the positive half-cycle duration was fixed while the negative half-cycle was adjusted in real time to ensure balanced and opposite total charge emission in each cycle, thereby avoiding propellant overcharging.

The measurements were conducted at a controlled temperature of 25°C using 1-ethyl-3-methylimidazolium bis(trifluoromethylsulfonyl)imide (EMI-Im) as the propellant. This setup enabled a detailed analysis into the impact of apex angle and voltage parameters on off-axis emission behavior and angular beam divergence.

The experimental measurements are presented in the set of graphs in Figure 29. The I/V curves for emitters with different tip angles are presented in Figure 29a. Consistent with theoretical predictions regarding electric field concentration understanding, emitters with smaller half-angles exhibit significantly lower onset voltages and substantially higher currents. However, these sharper emitters are prone to electrical short-circuiting at voltages near 1.3 kV. In contrast, emitters with larger half-angles present a stable operation at voltages up to 1.8 kV.

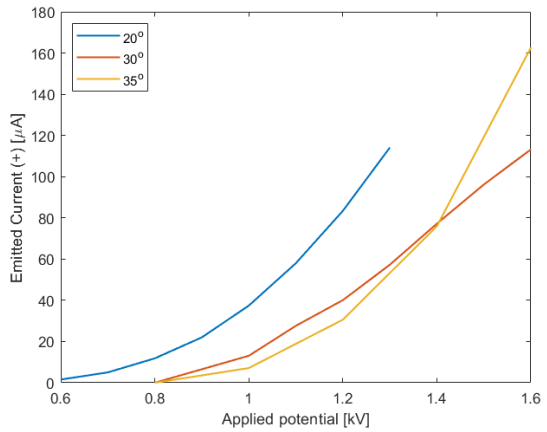

(a) Emitted current as applied potential function

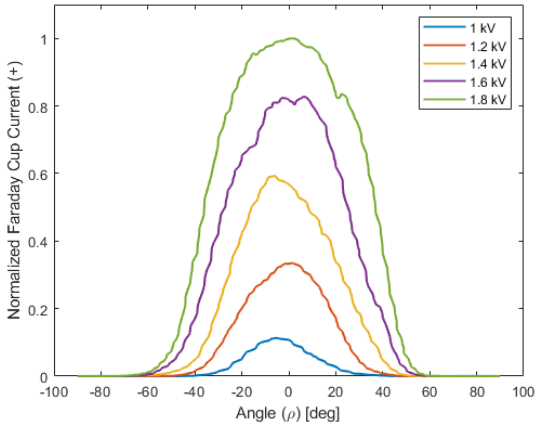

(b) Normalized collected current for 35° emitters

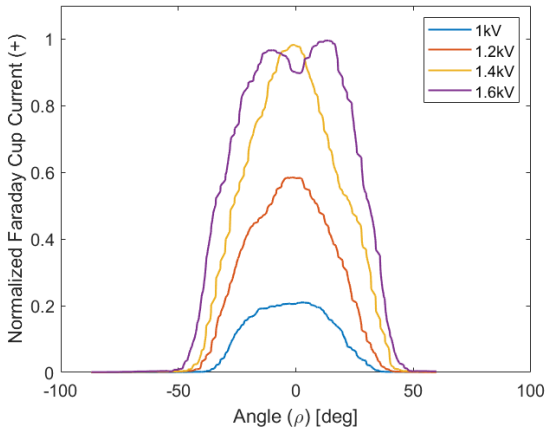

(c) Normalized collected current for 30° emitters

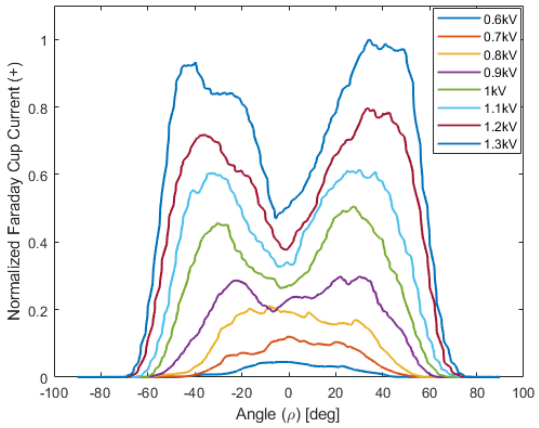

(d) Normalized collected current for 20° emitters

Figure 29: Graphics depicting emitters emitted current behavior as angle function under a positive polarity. (a) Emitted current as applied potential function for each structure. (b-d) Normalized collected current as a function of the collecting angle for emitters with half-angles (b) 35°, (c) 30°, and (d) 20° for different applied voltages.

The angular current distributions measured by the Faraday Cup for positive polarity are shown in Figures 29b–29d, providing detailed insights into the influence of emitter geometry on the emission profile behavior. Similarly, the plume dispersion for negative polarity is displayed in a separate set of graphs in Figure 30.

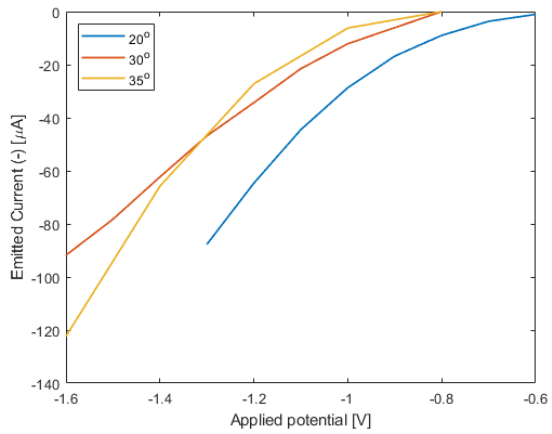

(a) Emitted current as applied potential function

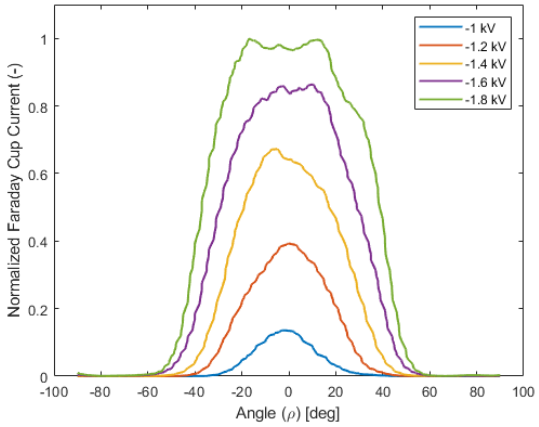

(b) Normalized collected current for 35° emitters

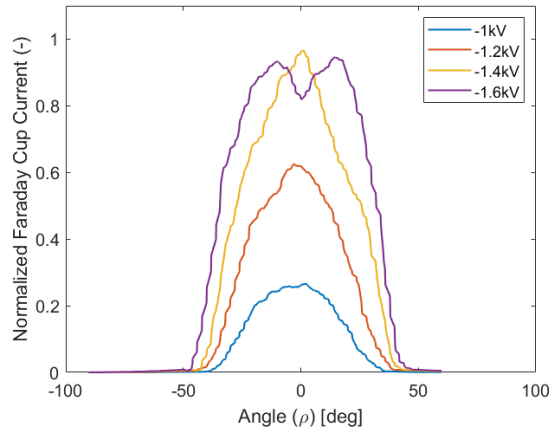

(c) Normalized collected current for 30° emitters

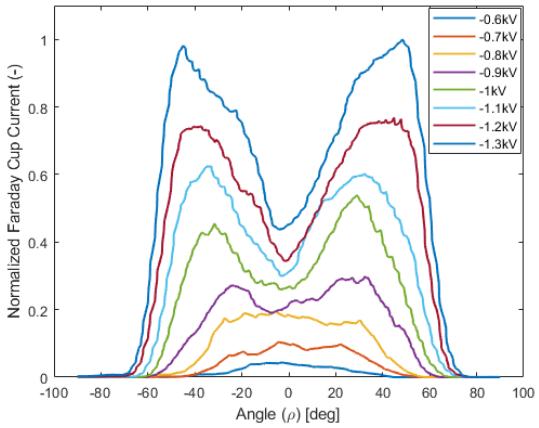

(d) Normalized collected current for 20° emitters

Figure 30: Graphics depicting emitters emitted current behavior as angle function under a negative polarity. (a) Emitted current as applied potential function for each structure. (b-d) Normalized collected current as a function of the collecting angle for emitters with half-angles (b) 35°, (c) 30°, and (d) 20° for different applied voltages.

Emitters with the sharpest tips (i.e., lower half-angles) produce emission profiles resembling Gaussian-like distributions, characterized by broad Full Width Half-Maximum (FWHM), which are similar for both polarities (Figures 29b and 30b). The increase in beam divergence observed at higher voltages is attributed to enhanced interactions, which broaden the emission profile as current levels rise. Similarly, Gaussian patterns are evident in Figures 29c and 30c, extending to voltages of up to 1.6 kV. Beyond this threshold,

a distinct anomaly emerges characterized by two pronounced current maxima appearing at angles of ±20°, indicating the onset of off-axis emission. Emitters with smaller half-angles (20°), as shown in Figures 29d and 30d, exhibit this off-axis behavior even at lower voltages near 0.8 kV, with current peaks at ±20°. Increasing the voltage significantly shifts the maximum angular position to ±45°, corresponding to the highest measured currents prior to short-circuiting. These findings suggest that as the emitter angle decreases, off-axis emission becomes increasingly dominant in the emission pattern.

The distinct I/V curves observed across emitters are a direct consequence of their geometric differences. To ensure meaningful comparisons, emission profiles were analyzed at equivalent current levels. Figures 31a and 31b display emission profiles for currents of 35 μA and 75 μA, respectively. Similarly, Figures 32a and 32b illustrate the results for negative polarity. Even at comparable current levels, sharper emitters exhibit significantly distorted and broadened annular beam shapes, exacerbated by increased current levels that amplify peak emission values and FWHM. Conversely, emitters with larger angles maintain Gaussian-like profiles at both current levels, with broader beam patterns only appearing as current increases.

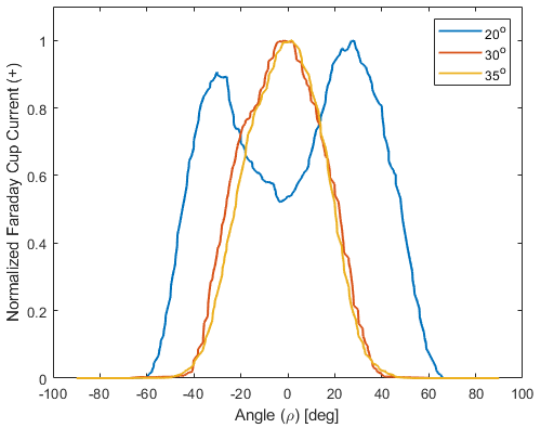

(a) Normalized collected current at 35 μA

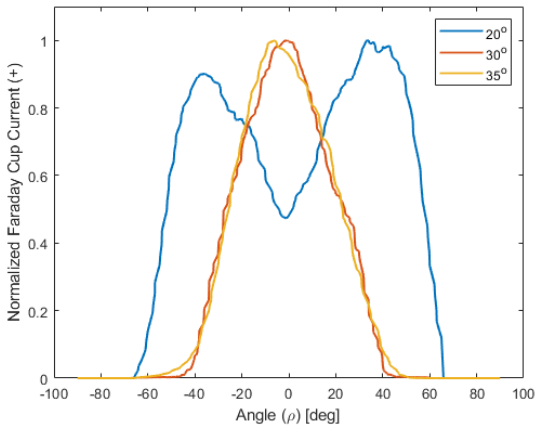

(b) Normalized collected current at 75 μA

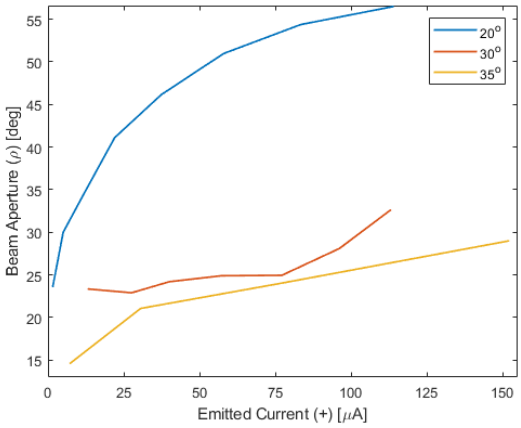

(c) Beam aperture evolution

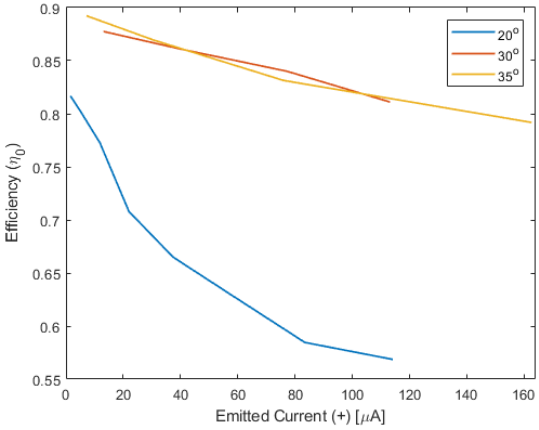

(d) Angular efficiency

Figure 31: Comparison of normalized collected current as a function of beam aperture under a positive polarity for emitters with half-angles of 35°, 30°, and 20° for emission currents near (a) 35 μA and (b) 75 μA. (c) Beam aperture angle evolution as a function of emitted current. (d) Angular efficiency of the emitters as a function of the emitted current.

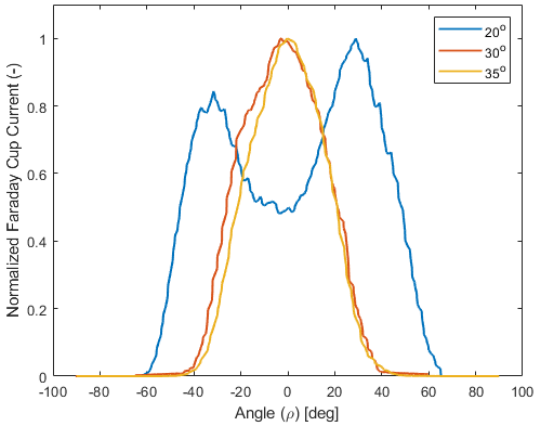

(a) Normalized collected current at -35 μA

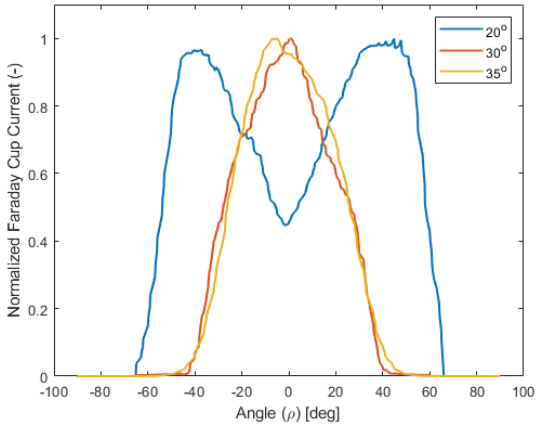

(b) Normalized collected current at -75 μA

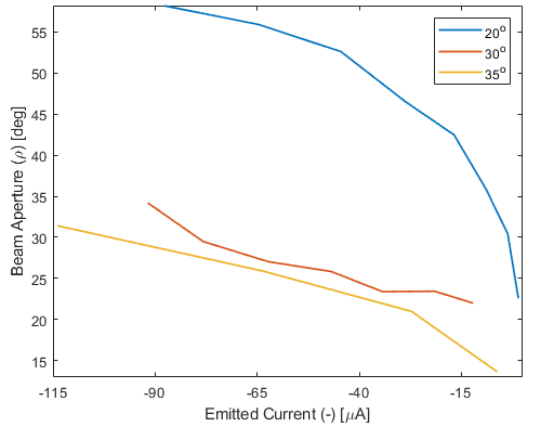

(c) Beam aperture evolution

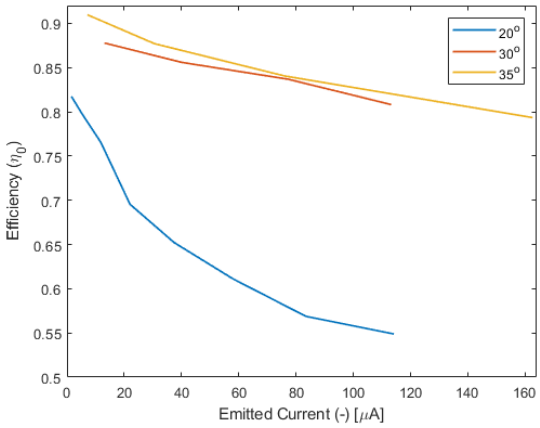

(d) Angular efficiency

Figure 32: Comparison of normalized collected current as a function of beam aperture under a negative polarity for emitters with half-angles of 35°, 30°, and 20° for emission currents near (a) -35 μA and (b) -75 μA. (c) Beam aperture angle evolution as a function of emitted current. (d) Angular efficiency of the emitters as a function of the emitted current.

These observations support the hypothesis that ionic emission may occur prematurely, before the propellant fully wets the apex of the emitter. Simulations shown in Figure 27b estimate the distances at which these emissions arise. In the 30° emitter operating at 1.8 kV, the emission appears to dominate at distances between 200 and 300 nm from the apex. For the 20° emitter, emissions may occur as far as 5 μm from the apex at

a threshold of 1.3 kV, resulting in the broad annular profiles that eventually cause device short-circuiting. The difficulty of achieving well-defined nanowire coverage near very sharp tips, due to steep surface slopes, likely hampers propellant flow to the apex. Consequently, ionic emission is triggered by intense electric fields several microns away from the tip, producing nearly perpendicular particle trajectories to the emitter surface. Figure 31c shows that off-axis emission in the 20° emitters is highly tunable with the applied voltage, as demonstrated by consistent results for both positive and negative polarities, confirming the symmetry of the emission process.

Off-axis emission is highly detrimental to thruster efficiency, as it significantly reduces the forward momentum of emitted particles. The forward emission efficiency, defined as:

$$\eta_0 = \left(\frac{\int_0^{\pi/2} \hat{I_{fc}}(\theta) \cos\theta \sin\theta \, d\theta}{\int_0^{\pi/2} \hat{I_{fc}}(\theta) \sin\theta \, d\theta} \right)^2 \tag{6.1}$$

quantifies the impact of off-axis emission, where θ is the angle relative to the emitter central axis and $\hat{I_{fc}}$ is the normalized collected current [102]. Figures 31d and 32d depict the evolution of angular efficiency with emitted current for emitters of varying geometries. Emitters with larger angles show a slight decrease in angular efficiency as applied voltage and emitted current increase, maintaining efficiencies above 80%. In contrast, smaller-angle emitters exhibit a more severe efficiency drop, falling to values as low as 55% at the highest emission currents due to the formation of broad annular patterns.

6.1.2 Beam angular profile as hydraulic resistance function

The emission behavior of ionic species can also be influenced by the transport of propellant along the emitter array. As demonstrated in section 6.1.1, premature ejection of the propellant can lead to off-axis emission. Similarly, it is reasonable to expect that suboptimal transport toward the active emitter region will result in reduced emission performance. To investigate this phenomenon, two emitter systems with identical geometries, 30° conical structures, were compared. These systems were distinguished by their hydraulic resistance values of $6{\cdot}10^{16}$ and $2{\cdot}10^{17}$ Pa·s/m^3.

Figure sets 33 and 34 illustrate the impact of hydraulic resistance on the performance of electrospray emitters, particularly its influence on critical parameters such as emitted current and beam divergence, in positive and negative polarities. As anticipated, an increase in hydraulic resistance results in a modest reduction in emitted current (Figures 33a and 34a), attributable to the restricted flow of ionic liquid towards the emitter tips.

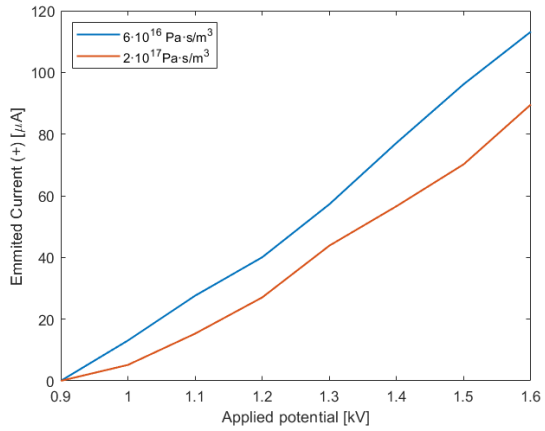

(a) Emitted current as applied potential function

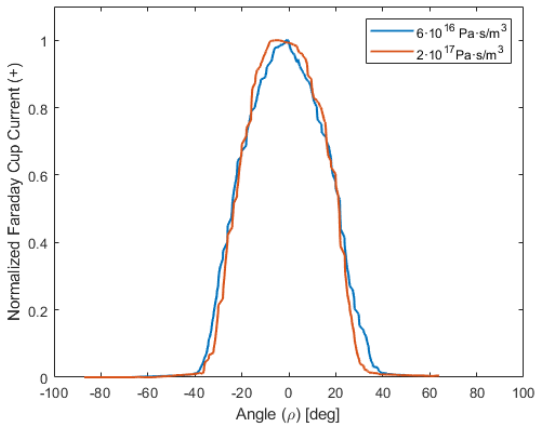

(b) Normalized collected current at 35 μA

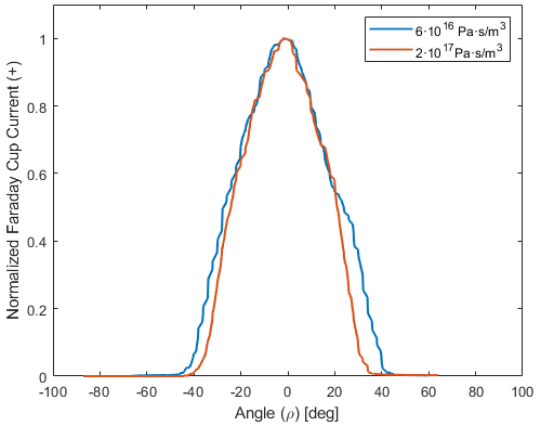

(c) Normalized collected current at 75 μA

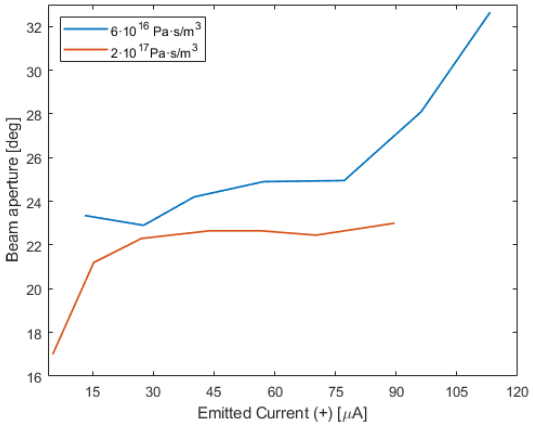

(d) Beam aperture

Figure 33: Comparison of 30° half-angle emitters with different hydraulic resistance for (a) emitted current evolution as a function of applied potential. Normalized collected current as a function of beam aperture for emitters at (b) 35 μA and (c) 75 μA. (d) Beam aperture angle evolution as a function of emitted current.

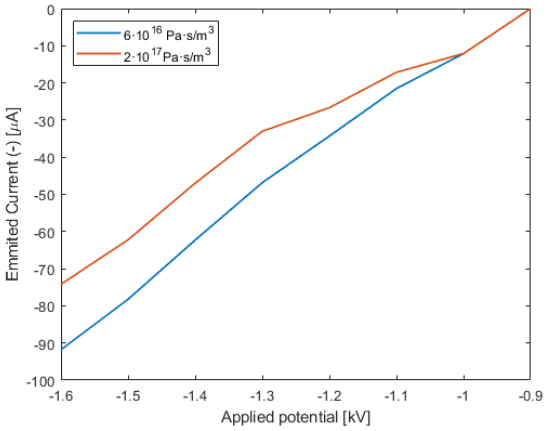

(a) Emitted current as applied potential function

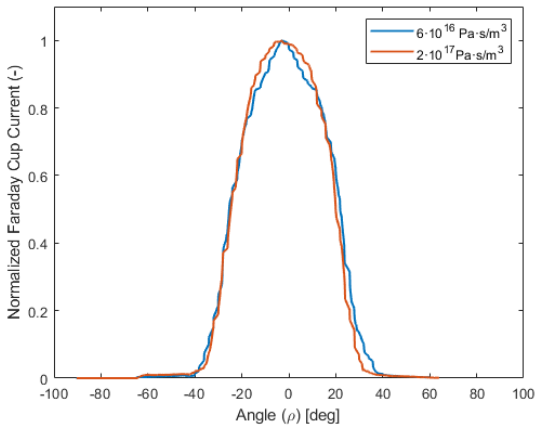

(b) Normalized collected current at -35 μA

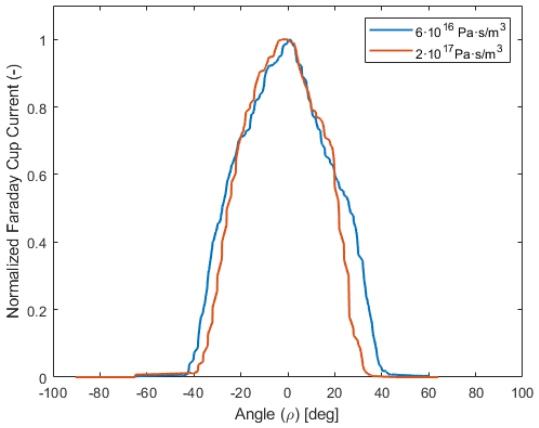

(c) Normalized collected current at -75 μA

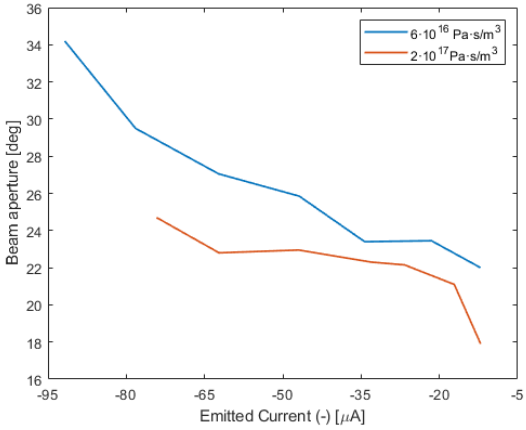

(d) Beam aperture

Figure 34: Comparison of 30° half-angle emitters with different hydraulic resistance for (a) emitted current evolution as a function of applied potential. Normalized collected current as a function of beam aperture for emitters at (b) -35 μA and (c) -75 μA. (d) Beam aperture angle evolution as a function of emitted current.

The angular current distribution patterns provide valuable insights into how emission characteristics evolve with increased hydraulic resistance. At lower emitted currents, the angular profiles exhibit Gaussian distributions, with emitters featuring higher impedance displaying slightly narrower Full Width at Half-Maximum (FWHM) values (Figures 33b and 34b). However, at higher current levels (Figures 33c and 33d), the differences between the devices become more pronounced. The FWHM narrows significantly for emitters with

greater hydraulic resistance. This reduction is likely due to the higher voltages required in high-resistance emitters to achieve comparable current levels. Regardless of the applied polarity (Figure 34c), these higher voltages increase the kinetic energy of the emitted particles, compensating for their reduced number by diminishing repulsive inter-particle forces. Consequently, the angular divergence of the beam is reduced.

This reduction in beam divergence has a notable effect on forward emission efficiency. Figures 35a and 35b depict the relationship between efficiency and emitted current for devices with varying hydraulic resistances. Emitters with lower hydraulic resistance exhibit a clear decline in efficiency as the emitted current increases. In contrast, high-resistance emitters maintain efficiencies above 88% across the entire current range. This demonstrates that optimizing hydraulic resistance provides a practical means to achieve more focused emission beams, enhancing the overall efficiency of electrospray devices.

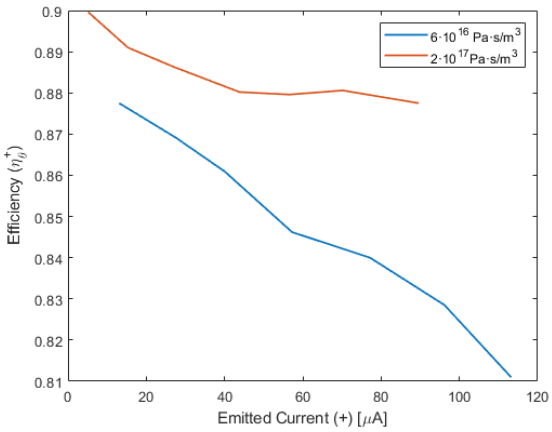

(a) Emission efficiency for positive polarity

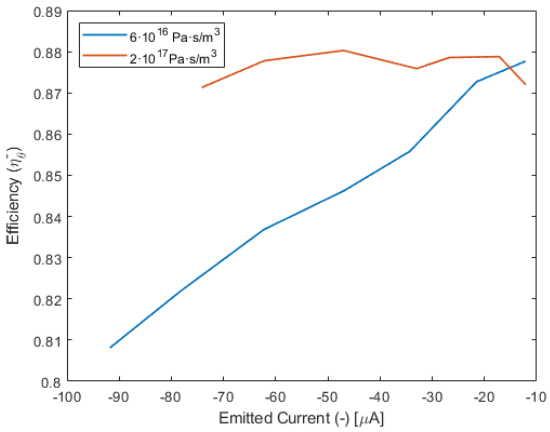

(b) Emission efficiency for negative polarity

Figure 35: Comparison of forward emission efficiency as a function of the emitted current for the emitters with different hydraulic resistance at (a) positive polarity and (b) negative polarity.

By managing hydraulic resistance effectively, the interplay between ionic liquid flow, emission current, and beam divergence can be fine-tuned, offering an additional pathway to improve the performance of electrospray systems for applications demanding high preci-

sion and efficiency.

6.2 Emitters degradation and Lifetime

6.2.1 Degradation mechanisms

As the optimization of emitter geometry successfully mitigates off-axis emission caused by overspray, addressing long-term operational stability remains a crucial challenge due to another potential failure mechanism: structural degradation during degradation. Over extended operation, emitter structures are subjected to a range of physical and chemical processes that can progressively deteriorate their integrity. This degradation not only alters the emission characteristics but may also lead to severe performance losses, including short-circuiting, unstable beam profiles, and eventual device failure. Understanding these mechanisms is essential for designing more robust and durable electrospray thrusters.

Structural degradation can originate from multiple sources. One primary cause is the redeposition of emitted species onto the emitter surface. In cases where charged particles follow trajectories that do not completely escape the vicinity of the emitter array, they can accumulate on the structure, modifying its shape and surface properties. Over time, this accumulation alters the local electric field distribution, leading to emission instabilities and potential electrical breakdowns. This effect is particularly pronounced in configurations with high off-axis emission, where a significant fraction of the emitted particles may be deflected back toward the emitter surface.

Beyond physical deposition, electrochemical reactions occurring during emission play a crucial role in structural deterioration. Electrospray thrusters operate by extracting and accelerating charged species, using ionic liquids as propellants. The high electric fields at the emitter tips can induce unintended electrochemical interactions between the liquid propellant and the emitter material. These reactions may lead to oxidation, corrosion, or other forms of chemical alteration that progressively weaken the emitter structure. In extreme cases, such modifications can compromise mechanical stability, increase electri-

cal leakage, and disrupt the uniformity of the emission process. The interplay between redeposition effects and electrochemical degradation presents a significant challenge in ensuring the longevity of electrospray devices. As material accumulation and chemical reactions reshape the emitter surface, local variations in the field strength can emerge, further amplifying non-uniform emission patterns and accelerating structural failure. These effects may become particularly severe when operating at high emission currents or under extended duty cycles, where prolonged exposure exacerbates material wear.

In the following sections, we explore the key mechanisms underlying emitter degradation, analyzing their impact on performance and failure modes. We also examine potential strategies to mitigate these effects, including material engineering approaches, surface treatments, and operational techniques aimed at preserving emitter integrity over extended operational lifetimes. By addressing these challenges, future electrospray thruster designs could achieve greater reliability, stability, and efficiency, ensuring their viability for long-duration space missions and advanced propulsion applications.

Early electrospray systems operated under constant polarity, often exceeding the electrochemical window and triggering degradation reactions. One of the most notable examples is the electrospray thruster aboard the Pathfinder mission, which functioned under these conditions. However, no significant degradation was reported, likely due to the specific ionic liquid used in the system [58, 103]. The challenges related with the electrochemical instability were later studied by Lozano through the use of EMI-BF_4 propellant in combination with different conductive emitter materials. To counteract charge accumulation within the electrochemical double layer and prevent saturation, a polarity-switching technique was introduced, periodically reversing the electrode potential to discharge the accumulated charge [104].

Despite this approach reduced the electrochemical effects, a rapid current decay was still observed within a few minutes of operation. This decay was attributed to the violation of the electrochemical window within the confined spatial dimensions of individual

pores, necessitating polarity switching at kilohertz frequencies, an impractical solution. To further address this limitation, the implementation of the upstream distal electrode, a configuration designed to protect the micro-tip emitters from degradation by redistributing electrochemical reactions away from the emission site, was proposed. In addition, conductive emitters were replaced altogether to suppress faradic reactions, thereby minimizing degradation effects [105]. However, this modification introduced a trade-off, as electrochemical attack was instead transferred to the distal electrode, acting as a sacrificial component to preserve the longevity and stability of the emitter tips.

6.2.2 Degradation protection analysis in the fabricated externally wetted emitters

Given that existing approaches have not successfully suppressed structural deterioration, in this thesis, the use of protective thin films is evaluated as an alternative to current degradation mitigation strategies. These coatings serve as a shielding layer to completely eliminate issues related to direct electrochemical reactions during emission or related to ion bombardment from charged species. Such degradation mechanisms arise from various factors, including component misalignment, fabrication defects, or improper emission, all of which exacerbate structural damage and can ultimately lead to system failure.

The most suitable materials for this protective role must: i) enable charge transport without interfering with emission, ii) exhibit high chemical resistance, and iii) possess a high breakdown voltage to withstand the intense electric fields experienced by the device. Based on these criteria and their deposition methodologies, silicon dioxide (SiO_2) [106, 107], aluminum oxide (Al_2O_3) [108], and silicon nitride (Si_3N_4), [109–111] were selected, including their advantageous properties and compatibility with the microfabrication process. These materials were deposited at the final stage of fabrication using different techniques: silicon dioxide via thermal oxidation or Plasma-Enhanced Chemical Vapor Deposition (PECVD), aluminum oxide through Atomic Layer Deposition (ALD), and silicon nitride using PECVD. ALD technique is a highly controlled deposition technique that ensures uniform and conformal thin films through sequential, self-limiting surface reactions of precursor gases, making it ideal for high-quality, nanometer-scale coatings.

PECVD, on the other hand, enhances the chemical vapor deposition process by utilizing plasma to activate precursor gases, enabling lower deposition temperatures and improved film properties. Initially, thermal oxidation was not employed for SiO_2 deposition due to facility limitations with the available equipment. Instead, for comparative analysis of layer degradation, SiO_2 was deposited using PECVD to maintain consistency across the different materials. However, for lifetime studies, thermal oxidation was later adopted due to its superior uniformity, as it grows the oxide layer from the silicon substrate rather than depositing it externally. This method results in a more stable and homogeneous protective film, providing enhanced durability and resistance under operational conditions.

To thoroughly investigate the behavior of different materials under electrospray operation, a systematic study was conducted to assess their resistance to prolonged electrochemical reactions exposure. Thin films of 200 nm were deposited on silicon substrates, ensuring uniform coverage to analyze their resistance to degradation. A physical characterization was performed using Scanning Electron Microscopy (SEM), comparing coated and uncoated silicon wafers, before and after emission, to determine the effectiveness of the protective layers. The analysis provided insights into material stability and guided the selection of the most suitable coatings for long-term operation.

The samples were analyzed in a high-vacuum chamber featuring a cubic structure with 290 mm sides and a central extension tube measuring 775 mm in length and 97 mm in inner diameter. The chamber pressure was maintained below 10^{-5} mbar, ensured by an Edwards turbo-molecular pump with an 85 L/s capacity to provide a controlled environment for testing. Each sample was subjected to a 1.6 kV voltage applied in both polarities, following a trapezoidal waveform with a 1-second period. While the voltage waveform was symmetric in amplitude, the positive half-cycle duration was kept constant, whereas the negative half-cycle was dynamically adjusted in real time. This adaptive control balanced the total emitted charge per cycle, effectively preventing overcharging of the propellant, which is a critical factor in long-term emitter performance. EMI-BF_4 [104,112] was selected as propellant due to its highly aggressive nature, ensuring that any mate-

rial vulnerabilities would be revealed under extreme operational conditions. Comparative SEM imaging before and after emission tests allowed for the identification of structural and morphological degradation. The samples were exposed to these conditions for four hours to determine which materials exhibited the highest resistance to electrochemical corrosion and ion bombardment effects. Figure 36 shows a bare silicon emitter structure before the emission. The structures exhibit poorly defined nanowires, as the coating analysis was conducted at an early stage of the microfabrication process development. Additionally, pre-emission images of the coated samples are not shown, as Fig. 36 serves as a representative case for all conditions. Furthermore, dielectric-coated devices tend to accumulate charge during SEM inspections, making their observation more challenging.

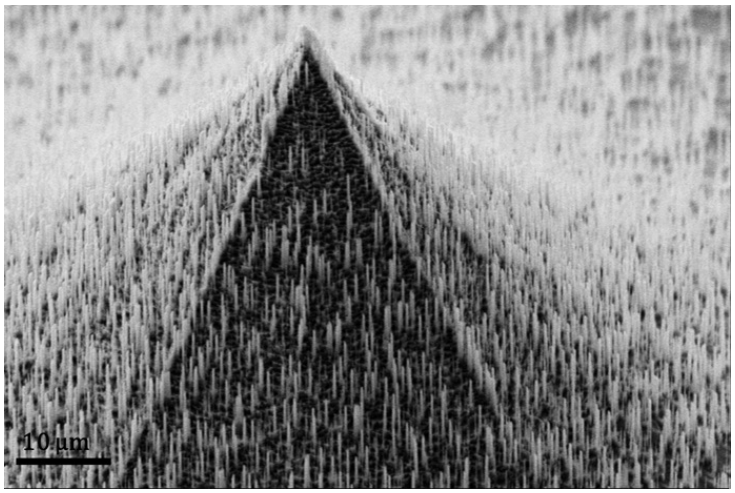

Figure 36: SEM image of a bare silicon microneedle before electrochemical degradation analysis using EMI-BF_4.

Fig. 37 provides a detailed comparison of the SEM images for the different coatings after the test, offering insight into the degradation mechanisms affecting each protective coating.

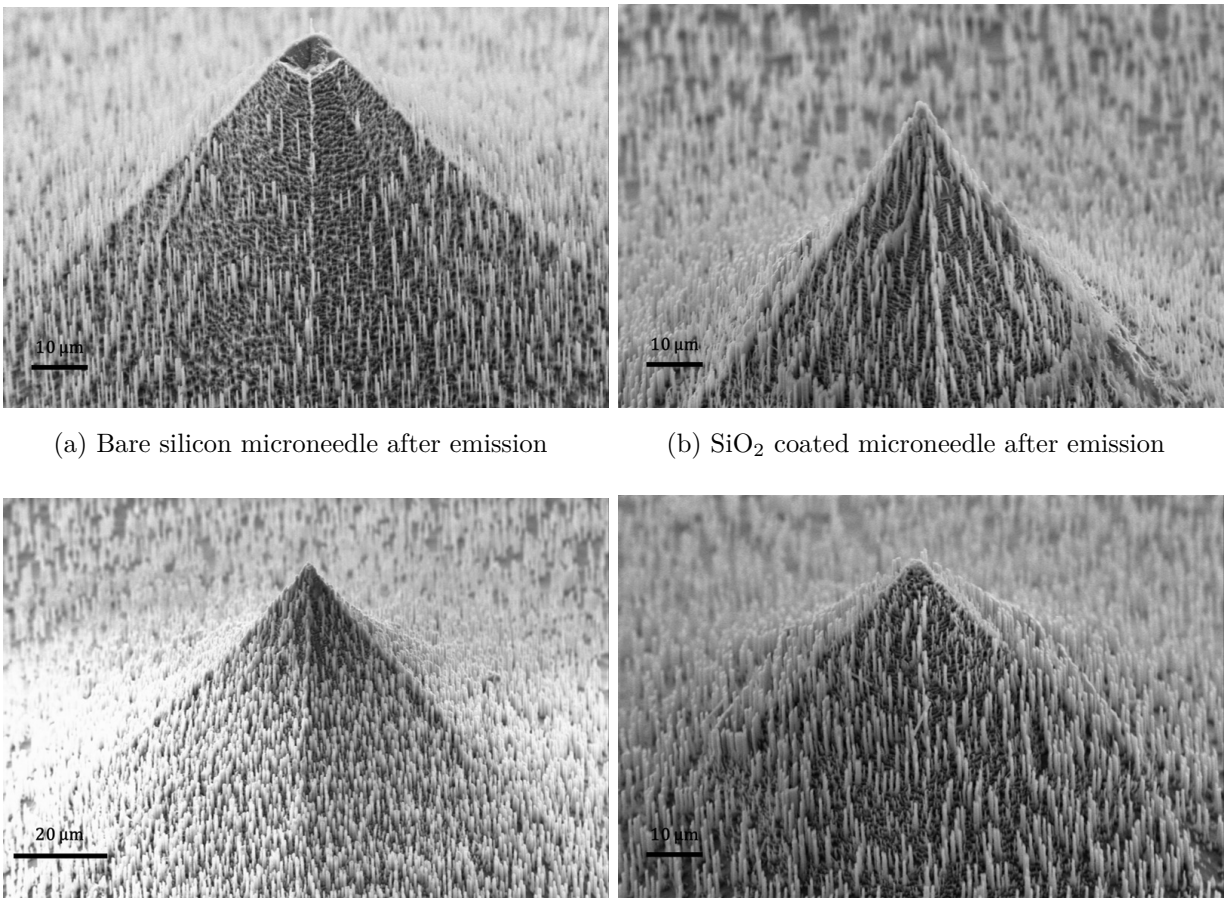

(a) Bare silicon microneedle after emission

(b) SiO_2 coated microneedle after emission

(c) Al_2O_3 coated microneedle after emission

(d) Si_3N_4 coated microneedle after emission

Figure 37: SEM images of (a) a bare silicon, (b) SiO_2 coated, (c) Al_2O_3 coated and (d) Si_3N_4 coated microneedle after electrochemical degradation analysis using EMI-BF_4.

The SEM images shown in Fig. 37 illustrate the overall behavior of the emitter system for each analyzed sample. Consistent with the findings of Lozano *et al.* [104], degradation of the emitters was observed when EMI-BF_4 was used and the bias was directly applied to the silicon emitter, even under alternating polarity conditions. The tips of the microneedles became blunt within minutes of operation, a result that aligns with the well-documented electrochemical etching effect of EMI-BF_4 on silicon [112].

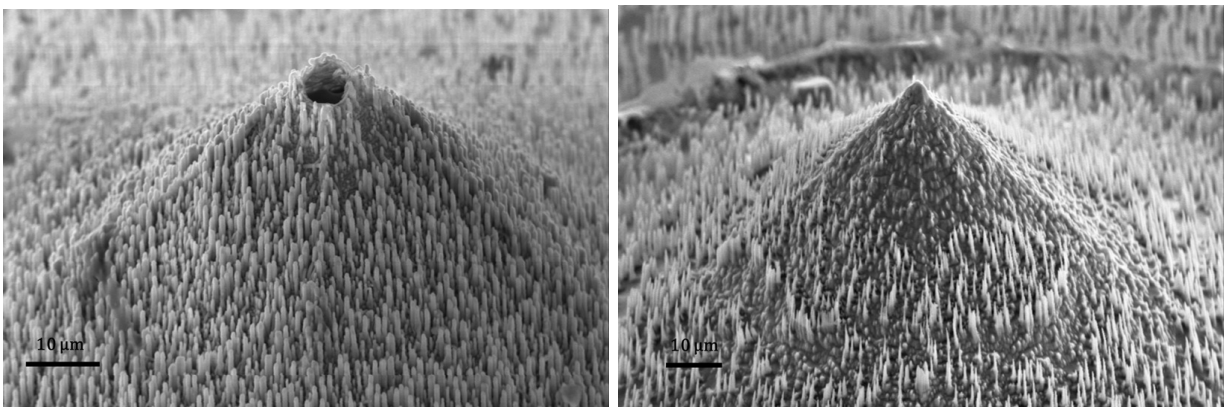

(a) Al_2O_3 hollowed coating (b) Dried propellant layer

Figure 38: SEM images of microneedles with (a) Al_2O_3 hollowed coating and (b) dried propellant after electrochemical degradation analysis using EMI-BF_4.

On the other hand, the results indicate a seemingly similar degradation pattern under identical conditions for the different protective coatings tested. While all coatings demonstrated significant chemical resistance, localized structural degradation was observed. Specifically, in the case of Al_2O_3 and SiO_2 coatings, 4 and 9 out of the 101 protected microneedles, respectively, exhibited a hollowing effect. In these instances, the protective layer remained intact, but the underlying silicon was etched away, forming crater-like structures (Fig. 38a). This phenomenon can be attributed to deposition-related defects, either due to inherent irregularities in the silicon substrate or limitations of the coating deposition techniques. While atomic layer deposition (ALD) offers exceptional precision at the atomic scale, plasma-enhanced chemical vapor deposition (PECVD) is generally less uniform and can introduce pinhole defects in thin layers. In the studied systems, since the material is deposited, the coating thickness could not exceed 200 nm without compromising the structural integrity of the microneedles, which would, in turn, negatively affect emission performance. Moreover, a dried propellant layer seems to cover the emitter surface and its structures (Fig. 38b). Nevertheless, it only can be proven by an EDX.

Although longer-duration tests would be required to fully assess the long-term stabil-

ity of these coatings, the preliminary results suggest that the three analyzed materials are strong candidates for mitigating electrochemical degradation. Furthermore, the final target propellant for practical implementation is EMI-Im, which is inherently less aggressive than EMI-BF_4, potentially reducing the severity of material degradation.

Following the chemical resistance analysis of the protective thin films, extended operational test were conducted using EMI-Im as propellant. In addition, thermal SiO_2-coated samples, 500 nm thick, were use to maximize the chemical. This coating was chosen over the others due to its unique formation process: unlike deposited layers, thermal oxide grows on the silicon substrate, thereby significantly reducing the structural impact on the microneedles, and minimizes the potential pinholes, provided that oxidation conditions are carefully controlled. The protected emitters were subjected to 100 hours of continuous electrospray operation to assess long-term material stability. The tested device maintained the same structural configuration as in previous studies from this thesis, ensuring consistency in the evaluation methodology. To further investigate material stability, elemental composition variations were examined using Energy Dispersive X-ray Spectroscopy (EDX). This SEM-integrated technique enables the quantification of elemental distribution and helps identify potential degradation mechanisms by detecting compositional changes in key regions of the emitters.

The following SEM images (Fig. 39a,b) provide a physical analysis of the devices after 100 hours of continuous emission. The structures have fully maintained their integrity, showing no visible signs of tip rounding or damage to the nanostructures. Prior to SEM inspection, the emitter devices were cleaned using isopropanol, in which they were submerged overnight to dissolve any remaining EMI-Im—a highly stable ionic liquid containing organic radicals. Despite effectively removing most residues, traces of dried propellant can still be observed around the emitter tips.

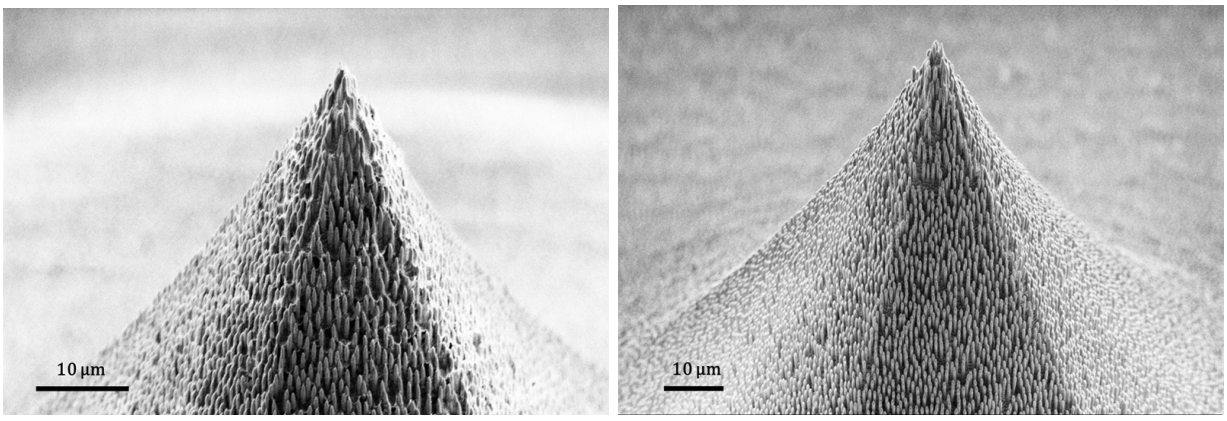

(a) Emitter with dried EMI-Im (b) Emitter without dried EMI-Im

Figure 39: SEM images of thermal SiO_2-coated microneedles (a) with and (b) without dried propellant after 100 hours of electrochemical degradation analysis using EMI-Im.

To assess the chemical integrity of both the protective coating and residual dried propellant layers, figure 40 presents SEM images of the device surface along, illustrating the spatial distribution of key elements. This analysis provides a detailed evaluation of the material's long-term stability under continuous electrospray operation. Additionally, Fig. 41 displays the frequency spectra of the various chemical elements detected across different regions of the device after 100 hours of uninterrupted emission. The peaks in the EDX spectrum represent K_α emissions, which are characteristic X-ray emissions that occur when an electron from the K-shell (the innermost electron shell) is ejected, and an electron from the L-shell drops down to fill the vacancy. This transition releases energy in the form of X-rays, and each element has a unique K_α peak at a specific energy. In the given spectrum, the highest peak corresponds to silicon (Si), with its K_α emission at 1.74 keV. The smaller peaks at lower energies correspond to carbon (C, $K_\alpha = 0.277$ keV) and oxygen (O, $K_\alpha = 0.525$ keV), which are commonly found in silicon-based materials, such as silicon dioxide (SiO2). Moreover, a small peak can be observed in the two last graphics, representing sulfur (S) with a peak at approximately 2.31 keV. Oxygen and silicon are key elements present both in the deposited oxide coating, which serves as a protective layer, and in the underlying substrate. In contrast, sulfur and carbon originate from the fundamental molecular structure of EMI-Im, appearing as residual traces

of the ionic liquid following emission. These results confirm that the protective layer's chemical components remain uniformly distributed across the surface, demonstrating its resilience against degradation induced by EMI-Im. Furthermore, traces of dried propellant are observed in specific areas of the structure. However, it is important to note that the propellant residue appears to have remained chemically inert, showing no signs of reaction with the device despite its embedded presence. This staged approach ensured a comprehensive understanding of material behavior, from initial resistance assessment to long-term performance validation.

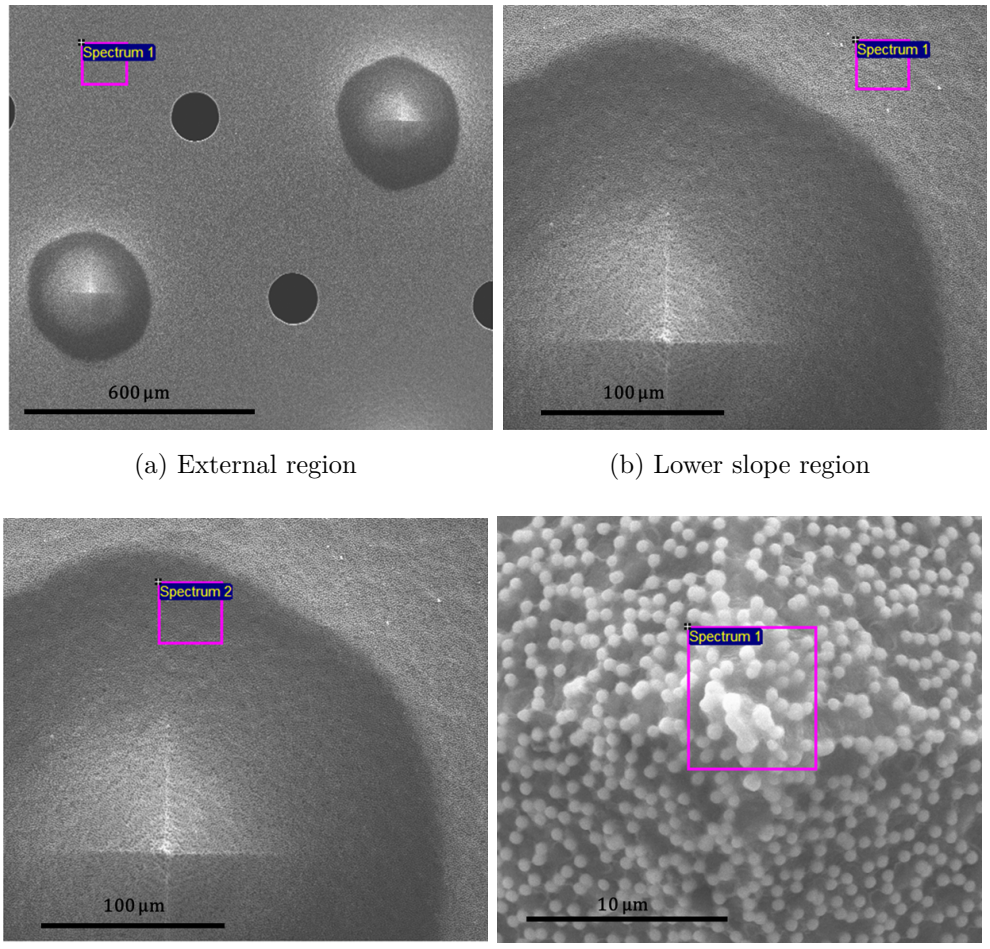

(a) External region

(b) Lower slope region

(c) Mid-slope region

(d) Tip region

Figure 40: SEM images of different regions of the emitter device coated with 500 nm of thermal SiO_2 during EDX measurements: (a) external region of the emitter, (b) lower slope of the emitter, (c) mid-slope of the emitter and (d) emitter tip region. The squares indicate the locations of EDX spectra measurements.

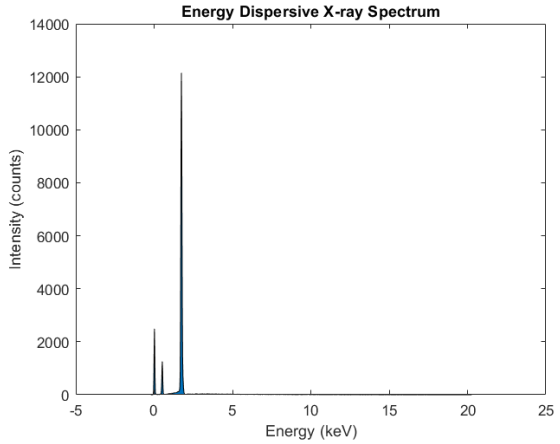

(a) External region spectrum

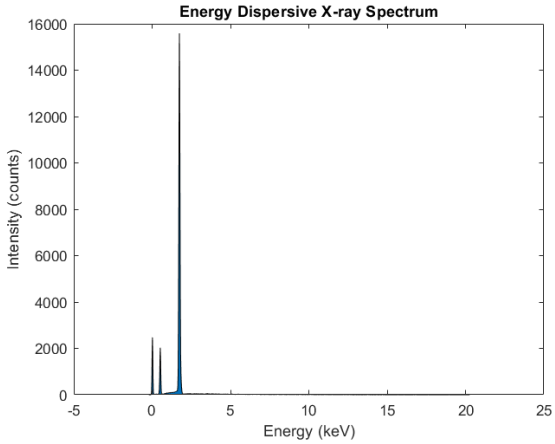

(b) Lower slope region spectrum

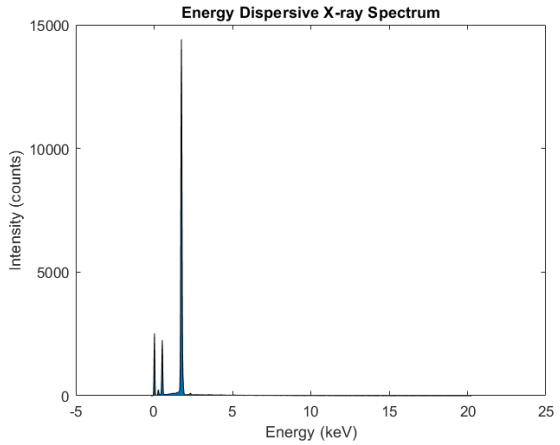

(c) Mid-slope region spectrum

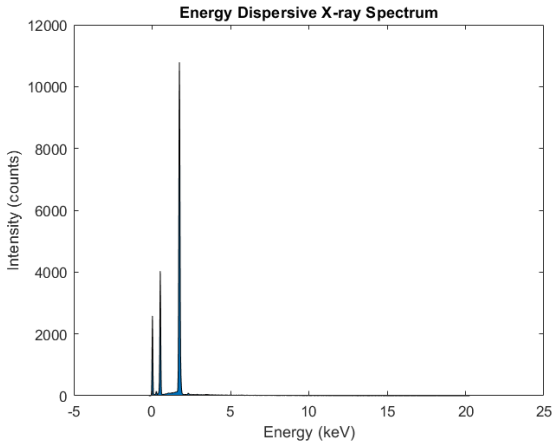

(d) Tip region spectrum

Figure 41: Energy-dispersive X-ray (EDX) spectra corresponding to different regions of the emitter device coated with 500 nm of thermal SiO_2. (a) Spectrum from outter region, (b) Spectrum from the lower slope of the emitter, (c) Spectrum from the mid-slope of the emitter. (d) Spectrum from the emitter tip. The highest peak in each spectrum corresponds to silicon (Si, K$\alpha = 1.74$ keV), while smaller peaks at lower energies correspond to carbon (C, K$\alpha = 0.277$ keV) and oxygen (O, $K_\alpha = 0.525$ keV). Additionally, a small peak at approximately 2.31 keV in (c) and (d) represents sulfur (S). These results confirm the uniform distribution of the protective oxide layer and the presence of residual traces of EMI-Im, which remained chemically inert after emission.

Chapter 7

7 Future perspectives

The results presented in this thesis have established a solid foundation for the development of externally wetted electrospray propulsion systems. However, several aspects require further exploration to enhance the performance, reliability, and scalability of these thrusters. Future research efforts should address the following areas:

- Optimize the self-assembly process to improve the uniformity and reproducibility of the colloidal lithography technique, allowing more homogeneous distributions to be achieved, leading to better propellant control.
- Delve deeper into the use of KOH-based wet etching techniques to establish an alternative fabrication route, enhancing structural uniformity and enabling batch manufacturing of multiple wafers, including larger-scale production.
- Refine manufacturing processes to enable large-scale production.
- Conduct more comprehensive analyses incorporating long-duration I-V measurements to monitor real-time degradation dynamics and assess emitter performance over extended operation.
- Evaluate device behavior under space-relevant conditions, including thermal cycling, vibrations, radiation exposure, and other environmental factors, to validate emitter performance in actual mission scenarios.
- Perform long-term emission studies exceeding 500 hours across multiple device batches to rigorously assess the operational stability and durability of the propulsion system.
- Research and understand the different control mechanisms capabilities of the externally wetted emitters to properly define the dynamic switch between droplet and ionic regimes, optimizing thrust levels.

Chapter 8

8 Conclusions

The research presented in this Thesis provides an in-depth exploration of microelectromechanical systems based on the electrospray phenomenon for small spacecraft propulsion. It spans fundamental principles, emission dynamics, propellant transport mechanisms, and long-term operational stability, advancing both the understanding and optimization of these devices. The findings contribute to bridging the gap between fundamental electrospray physics and its practical implementation in space propulsion, fostering the development of efficient, long-lifetime propulsion systems.

A central focus of this thesis has been the establishment of a standardized, repeatable, and industrially scalable fabrication method to develop functional electrospray emitters using silicon as the primary material. By leveraging advanced semiconductor microfabrication techniques in cleanroom environments, alongside disruptive approaches such as colloidal lithography, the capability to manufacture emitter arrays with micro- and nanoscale patterning has been successfully demonstrated. These emitters exhibit stable operation, validating the feasibility of this fabrication approach.

The characterization of these devices has focused on several critical aspects of the technology, including the influence of emitter geometry on beam angular distribution and thrust efficiency. The results confirm that tuning the emitter apex angle provides control over emission divergence, enabling optimization of the thrust-to-power ratio while maintaining emission stability. A quantitative correlation between emitter sharpness and local electric field enhancement has been established, revealing an optimal design range that minimizes undesired off-axis particle dispersion. Sharper emitters generate stronger local electric fields, reducing onset voltages but increasing the likelihood of off-axis emissions due to premature emission of the propellant before reaching the tip of the microneedles. Conversely, larger apex angles mitigate undesirable beam broadening by ensuring a more controlled acceleration of charged species along the intended thrust direction, resulting on greater angular efficiencies. These insights provide essential design guidelines for future

electrospray emitters, striking a balance between field enhancement and stable emission.

In addition, this research has provided significant insights into propellant wetting dynamics through the implementation of nanostructured surfaces. The development of nanowire-based externally wetted architectures has been shown to effectively regulate propellant transport along the surface, ensuring consistent wetting and minimizing flow instabilities that could lead to operational inefficiencies or system failure. Furthermore, the confirmation of hydraulic resistance as a governing parameter during electrospray emission highlights its potential as a tunable factor for optimizing thruster performance, and therefore, enabling greater angular emission efficiencies.

Material stability, a key limiting factor in prolonged electrospray operation, has been another major area of investigation in this work. The evaluation of various materials as protective coatings under the chemically aggressive conditions of EMI-BF_4 has demonstrated that silicon dioxide (SiO_2), aluminum oxide (Al_2O_3), and silicon nitride (Si_3N_4) exhibit high resistance to chemical degradation. However, the deposition method significantly impacts the effectiveness of the protective layer, influencing both its uniformity and thickness without compromising the emitter structures. Extensive long-term endurance testing has confirmed that thermally grown SiO_2 coatings substantially extend emitter lifespan by minimizing degradation from electrochemical reactions and ion bombardment. These coatings maintain structural integrity, preventing surface irregularities that could otherwise disrupt emission characteristics. Additionally, Energy Dispersive X-ray Spectroscopy (EDX) analysis has further confirmed that minimal compositional variations occur in SiO_2-coated emitters, reinforcing their suitability for extended mission scenarios.

From a broader perspective, the findings of this Thesis represent a significant advancement in the state of the art for electric propulsion systems designed for small satellite platforms. The demonstrated ability to control emission profiles and enhance material resilience lays a strong foundation for further improvements in the operational lifespan and thrust efficiency of electrospray-based spacecraft propulsion systems, highlighting the

critical role of precise emitter design and fabrication.

While this research has addressed fundamental challenges associated with externally wetted electrospray propulsion, further investigations are necessary to refine and extend these findings. Device fabrication should focus on improving structural uniformity and reproducibility, particularly regarding the propellant transport network, even at larger scales. Additionally, exploring alternative fabrication techniques will be essential to reduce process complexity and enhance industrial scalability. Furthermore, mission-scenario testing in relevant space environments is necessary to validate the long-term viability of these devices under real operational conditions, including launch phase conditions that could impact device integrity.

In conclusion, this thesis presents a comprehensive framework for electrospray propulsion systems, contributing both theoretical advancements and experimental validations. By addressing key limitations in emitter design, material degradation, and propellant dynamics, this research paves the way for the next generation of high-performance micropropulsion technologies, supporting the evolving landscape of small satellite missions.

References

References

[1] Bille, M. and Lishock, E. The first space race: Launching the world's first satellites. *Texas A&M University Press*, **2004**.

[2] Kuznetsov, V. D.; Sinelnikov, V. M. and Alpert, S. N. Yakov Alpert: Sputnik-1 and the first satellite ionospheric experiment. *Advances in Space Research*, 55, 2833-2839, **2015**. doi:10.1016/j.asr.2015.02.033.

[3] Poghosyan, A. and Golkar, A. Cubesat evolution: Analyzing cubesat capabilities for conducting science. *Progress in Aerospace Sciences*, 88, 59–83, **2017**. doi:10.1016/j.paerosci.2016.11.002.

[4] Puig-Suari, J.; Turner, C. and Twiggs, R. CubeSat: The Development and Launch Support Infrastructure for Eighteen Different Satellite Customers on One Launch. *15th AIAA/USU Conference on Small Satellites*, **2001**.

[5] Bouwmeester, J. and Guo, J. Survey of worldwide pico- and nanosatellite missions, distributions and subsystem technology. *Acta Astronaut.*, 67, 854-862, **2010**. doi:10.1016/j.actaastro.2010.06.004.

[6] Toorian, A.; Diaz, K. and Lee, S. The CubeSat approach to space access. *IEEE Aerospace Conference Proceedings*, **2008**. doi:10.1109/aero.2008.4526293

[7] Woellert, K.; Ehrenfreund, P.; Ricco, A. J.; Hertzfeld, H. Cubesats: Cost-effective science and technology platforms for emerging and developing nations. *Adv. Space Res.*, 47, 663-684, **2011**.

[8] Saeed, N.; Elzanaty, A.; Almorad, H.; Dahrouj, H.; Al-Naffouri, T. Y. and Alouini, M. S. CubeSat Communicatons: Recent Advances and Future Challenges. *IEEE Communications Surveys & Tutorials*, 22, 3, 1839-1862, **2020**. doi:10.1109/comst.2020.2990499.

[9] Radtke, J.; Stoll, E.; Lewis, H. and Bastida-Virgili, B. The impact of the increase in small satellite launch traffic on the long-term evolution of the space debris environment. *7th European Conference on Space Debris*, 7, **2017**.

[10] Tummala, A. R. and Dutta, A. An Overview of Cube-Satellite Propulsion Technologies and Trends. *Aerospace*, 4, 58, **2017**. doi:10.3390/aerospace4040058.

[11] Lemmer, K. Propulsion for CubeSats.*Acta Astronautica*, 134, 231-243, **2017**. doi:10.1016/j.actaastro.2017.01.048.

[12] Krejci, D. and Lozano, P. Space propulsion technology for small spacecraft. *Proceedings of the IEEE*, 106, 3, **2018**. doi:10.1109/jproc.2017.2778747

[13] Tajmar, M. Chemical Propulsion Systems. In: Advanced Space Propulsion Systems. *Springer, Vienna*, 23-42, **2003**. ISBN: 978-3-211-83862-4.

[14] Liou, L. Advanced Chemical Propulsion for Science Missions. *IEEE Aerospace Conference*, **2008**. doi: 10.1109/AERO.2008.4526549.

[15] Reed, B. D. On-Board Chemical Propulsion Technology. *NASA Glenn Research Center Cleveland*, **2004**.

[16] Mori, O.; Kushiki, K.; Sawai, S.; Shida, M.; Maru, Y.; Michigami, K.; Kagawa, H., Nagata, T.; Nakatsuka, J.; Goto, D.; Furukawa, K.; Takami, T.; Uramachi, H.; Mimasu, Y.; Terui, F.; Ogawa, N.; Ono, G. and Yoshikawa, K. Hayabusa2 Asteroid Sample Return Mission. *Technological Innovation Advances*, 433-452, **2022**. doi:10.1016/B978-0-323-99731-7.00022-2

[17] Tajmar, M. Nuclear Propulsion Systems. In: Advanced Space Propulsion Systems. *Springer, Vienna*, 57-72, **2003**. ISBN: 978-3-211-83862-4.

[18] Gabrielli, R. A. and Herdrich, G. Review of Nuclear Thermal Propulsion Systems. *Progress in Aerospace Sciences*, 79, 92-113, **2015**. doi:10.1016/j.paerosci.2015.09.001.

[19] Koroteev, A. S.; Oshev, Y. A.; Popov, S. A.; Karevsky, A. V.; Solodukhin, A. Y.; Zakharenkov, L. E. and Semenkin, A. V. Nuclear power propulsion system for spacecraft. *Thermal Engineering*, 62, 971-980, **2015**. doi:10.1134/S0040601515130078.

[20] Tsuda, Y. Flight status of IKAROS deep space solar sail demonstrator. **Acta Astronautica**, 69, 833-840, **2011**. doi:10.1016/j.actaastro.2011.06.005.

[21] Johnson, L.; Whorton, M.; Heaton, R. P.; Laue, G. and Adams, C. NanoSail-D: A solar sail demonstration mission. *Acta Astronautica*, 68, 571-575, **2011**. doi:10.1016/j.actaastro.2010.02.008.

[22] Fu, B.; Sperber, E. and Eke, F. Solar sail technology - A state of the art review. *Progress in Aerospace Sciences*, 86, **2016**. doi:10.1016/j.paerosci.2016.07.001.

[23] Fernando, B. Planning our first interstellar journey. *Astron. Geophys.*, 58, **2017**.

[24] Esho, A. O.; Iluyomade, T. D.; Olatunde, T. M. and Igbinenikaro, O. P. Electrical propulsion systems for satellites: a review of current technologies and future prospects. *International Journal of Frontiers in Engineering and Technology Research*, 6, 35-44, **2024**. doi:10.53294/ijfetr.2024.6.2.0034.

[25] O'Reilly, D.; Herdrich, G. and Kavanagh, D. F. Electric Propulsion Methods for Small Satellites: A Review. *Aerospace*, 8, 22, **2021**. doi:10.3390/aerospace8010022.

[26] Mazouffre, S. Electric propulsion for satellites and spacecraft: Established technologies and novel approaches. *Plasma Sources Sci. Technol*, 25, **2016**. doi:10.1088/0963-0252/25/3/033002.

[27] Blinov, V.; Vavilov, I.S.; Fedynin, V.V.; Shalay, V.V.; Yachmenev, P.S.; Ruban, V.I. Experimental investigations of nitrogen arcjet thruster with control unit for small spacecrafts. *J. Phys.*, 1210, **2019**. doi:10.1088/1742-6596/1210/1/012019.

[28] Vavilov, I.; Fedynin, V.V.; Yachmenev, P.S.; Zharikov, K.I.; Lukyanchik, A.I.; Stepen, P.V. Review of electric thrusters with low consumption power for corrective propulsion system of small space vehicles. *J. Phys.*, 1546, 1–10, **2020**. doi:10.1088/1742-6596/1546/1/012071.

[29] Mirtich, M. J. Resistojet propulsion for large spacecraft systems. *NASA Glenn Research Center Cleveland*, **1982**.

[30] LaPointe, M. R. and Mikellides, P. G. High Power MPD Thrusters Development at the NASA Glenn Research Center.*37th Joint Propulsion Conference and Exhibit AIAA/ASME/SAE/ASEE*, **2001**.

[31] Hall, E. On a new action of the magnet on electric currents. *Am. J. Math.*, 2, 287–292, **1879**. doi:10.2307/2369245.

[32] Goebel, D.M. and Katz, I. Fundamentals of Electric propulsion: Ion and Hall Thrusters. *John Wiley & Sons Publishing*, **2008**.

[33] Akhmetzhanov, R.; Bogatyi, A.V.; Kashirin, D.A.; Obukhov, V.A.; Popov, G.A.; Svotina, V.V. and Khartov, S. A. Low-Power Ion Thrusters. State of Development at Research Institute of Applied Mechanics and Electrodynamics, MAI. *Mater. Sci. Eng.*, 927, 1-5, **2020**. doi:10.1088/1757-899X/927/1/012075.

[34] Tajmar, M.; Vasiljevich, I. and Grienauer, W. High current liquid metal ion source using porous tungsten multiemitters. *Ultramicroscopy*, 111, 1-4, **2010**. doi:10.1016/j.ultramic.2010.09.005.

[35] Bock, D.; Bethge, M. and Tajmar, M. Highly miniaturized FEEP thrusters for CubeSat applications. *Proceedings of the 4th Spacecraft Propulsion Conference*, **2014**.

[36] Bock, D. and Tajmar, M. Highly miniaturized FEEP propulsion system (NanoFEEP) for attitude and orbit control of CubeSats. *Acta Astronautica*, 144, 422-428, **2018**. doi:10.1016/j.actaastro.2018.01.012.

[37] Lozano, P. and Martínez-Sánchez, M. Ionic liquid sources: Characterization of externally wetted emitters. *J. Colloid. Interface Sci.*, 282, 2, 415-421, **2005**. doi:10.1016/j.jcis.2004.08.132

[38] Taylor, G. Disintegration of water drops in an electric field. *Proc. R. Soc. Lond. A. Math. Phys. Sci.*, vol. 280, no. 1382, pp. 383–397, **1964**. doi:10.1098/rspa.1964.0151.

[39] Chen, F.; Lin, L.; Zhang, J.; He, Z.; Uchiyama, K. and Lin, J. M. Single-Cell Analysis Using Drop-on-Demand Inkjet Printing and Probe Electrospray Ionization Mass Spectrometry. *Anal. Chem.*, vol. 88, no. 8, pp. 4354–4360, **2016**. doi:10.1021/acs.analchem.5b04749.

[40] Choi, J.; Kim, Y. J.; Lee, S.; Son, S. U.; Ko, H. S.; Nguyen, V. D. and Byun, D. Drop-on-demand printing of conductive ink by electrostatic field induced inkjet head. *Appl. Phys. Lett.*, vol. 93, no. 19, p. 193508, **2008**. doi:10.1063/1.3020719/336481.

[41] Steipel, R. T.; Gallovic, M. D.; Batty, C. J.; Bachelder, E. M. and Ainslie, K. M. Electrospray for generation of drug delivery and vaccine particles applied in vitro and in vivo. *Materials Science and Engineering: C*, vol. 105, p. 110070, **2019**. doi:10.1016/j.msec.2019.110070.

[42] Huang, C.; Jian, G.; De Lisio, J. B.; Wang, H. and Zachariah, M. R. Electrospray Deposition of Energetic Polymer Nanocomposites with High Mass Particle Loadings: A Prelude to 3D Printing of Rocket Motors. *Adv. Eng. Mater.*, vol. 17, no. 1, pp. 95–101, **2015**. doi:10.1002/adem.201400151.

[43] Cadnum, J. L.; Jencson, A. L.; Livingston, S. H.; Li, D.; Redmond, S. N.; Pearlmutter, B.; Wilson, B. M. and Donskey, C. J. Evaluation of an electrostatic spray disinfectant technology for rapid decontamination of portable equipment and large open areas in the era of SARS-CoV-2. *Am. J. Infect. Control*, vol. 48, no. 8, pp. 951–954, **2020**. doi:10.1016/j.ajic.2020.06.002.

[44] Krupa, A.; Jaworek, A.; Sobczyk, A. T.; Marchewicz, A.; Szudyga, M. and Antes, T. Charged spray generation for gas cleaning applications. *J. Electrostat.*, vol. 71, no. 3, pp. 260–264, **2013**. doi:10.1016/j.elstat.2012.11.022.

[45] Kizilyaprak, C.; Daraspe, J. and Humbel, B. M. Focused ion beam scanning electron microscopy in biology. *J. Microsc.*, vol. 254, no. 3, pp. 109–114, **2014**. doi:10.1111/jmi.12127.

[46] Orloff, J.; Utlaut, M. and Swanson, L. Applications of Focused Ion Beams. *High Resolution Focused Ion Beams: FIB and its Applications*, Springer, Boston, MA. **2003**. doi:10.1007/978-1-4615-0765-9_7.

[47] Yamashita, M. and Fenn, J. B. Electrospray ion source: Another variation on the free-jet theme. *Journal of Physical Chemistry*, vol. 88, no. 20, pp. 4451–4459, **1984**. doi.org/10.1021/j150664a002.

[48] Inculet, I. I.; Castle, G. S. P. and Ting, J. Electrostatic dissipation of smoke using evaporating charged water spray. *Conference Record - IAS Annual Meeting (IEEE Industry Applications Society)*, vol. 2, pp. 2144–2147, **1989**. doi:10.1109/ias.1989.96936.

[49] Kinsey, J. and Pendleton, F. J. Evaluation of Charged Fog for Smoke Clearing Shipboard Fires. *Defense Technical Information Center*, **2023**.

[50] Okuda, H. and Kelly, A. J. Electrostatic atomization—Experiment, theory and industrial applications. *Phys. Plasmas*, vol. 3, no. 5, pp. 2191–2196, **1996**. doi:10.1063/1.871674.

[51] Prince, B. D.; Fritz, B. A. and Chiu, Y. H. Ionic liquids in electrospray propulsion systems. *ACS Symposium Series*, 1117, 27-49, **2012**. doi:10.1021/bk-2012-1117.ch002.

[52] Gassend, B.; Velásquez-García, F.; Akinwande, A. I. and Martínez-Sánchez, M. Fabrication of a fully integrated electrospray array with application to space propulsion. *IEEE 21st International Conference on Micro ElectroMechanical Systems*, 976-979, **2008**. doi:10.1109/memsys.2008.4443821.

[53] Courtney, D.; Li, H.; Lozano, P.; Gomez-Maqueo, P. and Fedkiw, T. On the Validation of Porous Nickel as Substrate Material for Electrospray Ion Propulsion. *American Institute of Aeronautics and Astronautics 46th AIAA/ASME/SAE/ASEE Joint Propulsion Conference & Exhibit*, **2010**. doi:10.2514/6.2010-7020.

[54] Ma, C.; Messina, V.; Ryan, C.; Rovey, J. L.; Putnam, Z. R.; Lembeck, M. F. and Berg, S. P. Emission characterization of porous electrospray thrusters with actively controlled flow rate. *37th International Electric Propulsion Conference*, **2022**.

[55] Cisquella-Serra, A.; Galobardes-Esteban, M. and Gamero-Castaño, M. Scalable Microfabrication of Multi-Emitter Arrays in Silicon for a Compact Microfluidic Electro-

spray Propulsion System. *ACS Appl. Mater. Interfaces*, vol. 14, no. 38, pp. 43527–43537, **2022**. doi:10.1021/acsami.2c12716.

[56] Villegas-Prados, D.; Cruz, J.; Wijnen, M.; Correyero, S.; Fajardo, P. and Navarro-Cavallé, J. Impact of propellant temperature on the emission regime of an externally wetted electrospray system using time-of-flight mass spectrometry. *Acta Astronautica*, vol. 213, pp. 145–155, **2023**. doi:10.1016/j.actaastro.2023.08.045.

[57] Fenn, J.; Mann, M.; Meng, C.; Wong, S. and Whitehouse, C. Electrospray ionization for mass spectrometry of large biomolecules. *Science*, 246, 64–71, **1989**. doi:10.1126/science.2675315.

[58] Wirz, R. E. Electrospray Thruster Performance and Lifetime Investigation for the LISA Mission. *AIAA Propulsion and Energy Forum*, **2019**. doi:10.2514/6.2019-3816.

[59] Romero-Sanz, I.; Bocanegra, R.; Fernández de la Mora, J. and Gamero-Castaño, M. Source of heavy molecular ions based on Taylor cones of ionic liquids operating in the pure ion evaporation regime. *J. Appl. Phys.*, 94, 3599-3605, **2003**. doi:10.1063/1.1598281.

[60] Thuppul, A.; Wright, P. L.; Collins, A. L.; Ziemer, J. K. and Wirz, R. E. Lifetime Considerations for Electrospray Thrusters. *Aerospace*, 7, 108, **2020**. doi:10.3390/aerospace7080108.

[61] Tsuda, T.; Nohira, T.; Amezawa, K.; Hachiya, K,; Hagiwara, R.; Raz, O. and Ein-Eli, Y. Anodic electrode reaction of p-type silicon in 1-ethyl-3-methylimidazolium flurohydrogenate room-temperature ionic liquid. *Electrochimica Acta 53*, **2008**, 3650-3655.

[62] Seki, S.; Serizawa, N.; Hayamizu, K.; Tsuzuki, S.; Umebayashi, Y.; Takei K. and Miyashiro, H. Physicochemical and Electrochemical Properties of 1-Ethyl-3-Methylimidazolium Tris(pentafluoroethyl)trifluorophosphate and 1-Ethyl-3-Methylimidazolium Tetracyanoborate. *Journal of The Electrochemical Society*, **159**(7), **2012**.

[63] Choudhary, V. and Iniewski, K. MEMS: fundamental technology and applications. *Taylor & Francis Group*, **2013**.

[64] Gad-el-Hal, M. MEMS: Design and Fabrication. *Taylor & Francis Group*, **2006**.

[65] Judy, J. W. Microelectromechanical systems (MEMS): fabrication, design and applications. *Smart Mater. Struct.*, 10, 1115-1134, **2001**. doi:10.1088/0964-1726/10/6/301.

[66] Senturia, S. D. Microsystem design. *Kluwer Academic Publishers*, **2001**. ISBN: 0-7923-7246-8

[67] Franssila, S. Introduction to Microfabrication. *John Wiley & Sons, Ltd.*, **2010**. ISBN: 978-0-470-74983-8.

[68] Plummer, J. D.; Deal, M. D. and Griffin, P. B. Silicon VLSI Technology. *Prentice Hall, Inc.*, **2000**. ISBN: 0-13-085037-3.

[69] Bell, D. J.; Lu, T. J.; Fleck, N. A. and Spearing, S. M. MEMS actuators and sensors: observations on their performance and selection purpose. *J. Micromech. Microeng.*, 15, **2005**. doi:10.1088/0960-1317/15/7/022.

[70] Varadan, V. K.; Vinoy, K. J. and Jose, K. A. RF MEMS and their applications. *John Wiley & Sons, Ltd.*, **2003**. ISBN: 0-470-84308-X.

[71] Chircov, C. and Grumezescu, A. M. Microelectromechanical Systems (MEMS) for Biomedical Applications. *Micromachines*, 13, 164, **2022**. doi:10.3390/mi13020164.

[72] Khoshnoud, F. and de Silva, C. W. Recent advances in MEMS sensor technology - biomedical applications. *IEEE Instrumentation & Measurements Magazine*, 15, 1, 8-14, **2012**. doi:10.1109/MIM.2012.6145254.

[73] Dandavino, S.; Ataman, C.; Shea, H.; Ryan C.; and Stark, J. Microfabrication of Capillary Electrospray Emitters and ToF Characterization of the Emitted Beam. *32nd International Electric Propulsion Conference*, **2011**, 131.

[74] Dandavino, S.; Ataman, C.; Chakraborty, S.; Shea, H.; Ryan, C. and Stark, J. Design and fabrication of the thruster heads for the MicroThrust MEMS electrospray propulsion system. *33rd International Electric Propulsion Conference*, **2013**, 127.

[75] Dandavino, S.; Ataman, C.; Ryan, C.N.; Chakraborty, S.; Courtney, D.; Stark, J.P.W. and Shea, H. Microfabricated electrospray emitter arrays with integrated extractor and accelerator electrodes for the propulsion of small spacecraft. *J. Micromech. Microeng.*, 24, **2014**. doi:10.1088/0960-1317/24/7/075011.

[76] Nakagawa, K.; Tsuchiya, T. and Takao, Y. Microfabricated emitter array for an ionic liquid electrospray thruster. *Jpn. J. Appl. Phys.*, 56, **2017**. doi:10.7567/jjap.56.06gn18.

[77] Melo Máximo, D.V. and Velásquez-García, L.F. Additively manufactured electrohydrodynamic ionic liquid pure-ion sources for nanosatellite propulsion. *Additive Manufacturing 36*, **2020**. doi:10.1016/j.addma.2020.101719.

[78] Tachibana, F.; Tsuchiya, T. and Takao, Y. Uniform needle-emitter arrays for ionic liquid electrospray thruster with precise thrust control. *Jpn. J. Appl. Phys. 60*, **2021**. doi:10.35848/1347-4065/abe997.

[79] Fernández de la Mora, J. The fluid dynamics of Taylor Cones. *Annu. Rev. Fluid Mech.*, vol. 39, pp. 217–243, **2007**. doi:10.1146/annurev.fluid.39.050905.110159.

[80] Ganero-Castaño, M. and Fernández de la Mora, J. Direct measurement of ion evaporation kinetics from electrified liquid surfaces. *J. Chem. Phys.*, 113, 815-832, **2000**. doi:10.1063/1.481857.

[81] Xiong, J.; Zhou, Z.; Ye, X.; Wang, X. and Feng, Y. Research on electric breakdown problems of a micro-colloid thruster. *Sensors and Actuators A*, 108, 134-137, **2003**. doi:10.1016/j.sna.2003.07.013.

[82] Cho, S.; Tummala, R. and Joshi, Y. Capillary performance of micropillar arrays in different arrangements. *Nanoscale and microscale thermophysical engineering*, 22, 2, 97-113, **2018**. doi:10.1080/15567265.2018.1431749.

[83] Zhao, Y.; Descamps, J.; al Hoda Al Bast, Nour.; Duque, M.; Esteve, J, Sepúlveda, B.; Loget, G. and Sojic, N. All-Optical Electrochemiluminescence. *J. Am. Chem. Soc.*, **2023**, 145, 31, 17420–17426. doi:10.1021/jacs.3c05856

[84] Serrà, A.; Gómez, E.; al Hoda Al Bast, N.; Zhang, Y.; Duque, M.; Esplandiu, M.J.; Esteve, J.; Nogués, J. and Sepúlveda, B. Wireless pulsed nanophotoelectrochemical cell for the ultrafast degradation of organic pollutants. *Chemical Engineering Journal*, **2024**. doi:10.1016/j.cej.2024.150663

[85] Tamayol, A. and Bahrami, M. Transverse permeability of fibrous porous media. *Physical Review E*, 83, **2011**. doi:10.1103/PhysRevE.83.046314.

[86] Kumar-Gunda, N. S.; Joseph, J.; Tamayol, A; Akbari, M. and Mitra, S. K. Measurement of pressure drop and flow resistance in microchannels with integrated micropillars. *Microfluid Nanofluid*, 14, 711-721, **2013**. doi:10.1007/s10404-012-1089-1.

[87] Ramos-Tomás, R.; Villegas-Prados, D.; de Saavedra, B.; Cruz, J. and Sepúlveda, B. Impact of Tip Angle on the Divergence and Efficiency of Electrospray Thrusters. *ACS Appl. Electron. Mater.*, **2024**. doi:10.1021/acsaelm.4c01224.

[88] Villegas-Prados, D.; Cruz, J.; Wijnen, M.; Fajardo, P. and Navarro-Cavallé, J. Emission and performance characterization of ionic liquids for an externally wetted electrospray thruster. *Acta Astronautica*, 219, 97-107, **2024**. doi:10.1016/j.actaastro.2024.03.013.

[89] Wolf, S. and Tauber, R. Silicon Processing for the VLSI Era: Process Technology, Vol. 1, **Lattice Press**, **1986**.

[90] Seidel, H.; Csepregi, L., Heuberger, A. and Baumgärtel, H. Anisotropic etching of crystalline silicon in alkaline solutions. *J. Electrochem. Soc.*, 137, 11, **1990**.

[91] Ai, B.; Möhwald, H.; Wang, D. and Zhang, G. Advanced Colloidal lithography beyond surface patterning. *Adv. Mater. Interfaces*, 4, **2017**.

[92] Yang, S.; Jang, S.; Choi, D.; Kim, S. and Yu, H. Nanomachining by colloidal lithography. *Small*, 2, 4, **2006**.

[93] Chen, K.; Rajeeva, B.; Wu, Z.; Rukavina, M.; Dao, T.; Ishii, S.; Aono, M.; Nagao, T. and Zheng, Y. Moiré Nanosphere Lithography. *ACS Nano*, 9, 6, **2015**.

[94] Guo, Y. and Kegel, W. Fabrication of floating colloidal crystal monolayers by convective deposition. *Journal of Colloid and Interface Science*, 587, **2021**.

[95] Qamhieh, K. Effect of dielectric constant on the theta potential of spherical electric double layers. *Molecules*, 29, 11, **2024**. doi: 10.3390/molecules29112484.

[96] Attard, P. Recent advances in the electric double layer in colloid sciences. *Current Opinion in Colloid & Interface Science*, 6, **2001**.

[97] Rao, S.R. Electrical Characteristics of Interfaces. Electrical Double Layer and Zeta Potential. In: Surface Chemistry of Froth Flotation. *Springer*, Boston, MA, pp. 209-255, **2004**. doi:10.1007/978-1-4757-4302-9_5.

[98] Du, C.; Zhao, Y. and Li, Y. Effect of Surface Cleaning Process on the Wafer Bonding of Silicon and Pyrex Glass. *J Inorg Organomet Polym*, 33, 673-679, **2023**. doi:10.1007/s10904-022-02510-x.

[99] Jefimovs, K.; Romano, L.; Vila-Comamala, J.; Kagias, M.; Wang, Z.; Wang, L.; Dais, C.; Solak, H. and Stampanoni, M. High-aspect ratio silicon structures by displacement Talbot lithography and Bosch etching. *Proc. SPIE 10146, Advances in Patterning Materials and Processes XXXIV*, **2017**. doi:10.1117/12.2258007.

[100] Gerlt, M. S.; Läubli, N. F.; Manser, M.; Nelson, B. J. and Dual, J. Reduced etch lag and high aspect ratios by deep reactive ion etching (DRIE). *Micromachines*, 12, 542, **2021**. doi:10.3390/mi12050542.

[101] Cao, H.; Li, X.; Zhou, B.; Chen, T.; Shi, T.; Zheng, J.; Liu, G. and Wang, Y. On-Demand Fabrication of Si/SiO_2 Nanowire Arrays by Nanosphere Lithography and Subsequent Thermal Oxidation. *Nanoscale Res Lett*, 12, **2017**. doi:10.1186/s11671-017-1883-5.

[102] Petro, E.; Bruno, A.; Lozano, P.; Perna, L. E. and Freeman, D. Characterization of the TILE Electrospray Emitters. *AIAA Propulsion and Energy 2020 Forum*, 2020.

[103] Uchizono, N.M.; Collins, A.L.; Marrese-Reading, C.; Arestie, S.M.; Ziemer, J.K. and Wirz, R.E. The role of secondary species emission in vacuum facility effects for electrospray thrusters. *J. Appl. Phys. 130*, **2021**. doi:10.1063/5.0063476.

[104] Lozano, P.C. and Martínez-Sánchez, M. Ionic liquid ion sources: supression of electrochemical reactions using voltage alternation. *Journal of Colloid and Interface Science 280*, **2004**, 149-154. doi:0.1016/j.jcis.2004.07.037.

[105] Brikner, N. and Lozano, P.C. The role of upstream distal electrodes in mitigating electrochemical degradation of ionic liquid ion sources. *Appl. Phys. Lett. 101*. **2012**. doi:10.1063/1.4766293.

[106] Usui, T.; Donnelly, C. A.; Logar, M.; Sinclair, R.; Schoonman, J. and Prinz, F. B. Approaching the limits of dielectric breakdown for SiO2 films deposited by plasma-enhanced atomic layer deposition. *Acta Materialia*. **2013**, 7660-7670. doi:10.1016/j.actamat.2013.09.003

[107] Qin, F.; Jiang, L.; Long, P.; Xu, S.; Ling, Y.; Yu, Y. and Wei, G. Effect of Deposition Potential on Preparation and Corrosion Resistance of SiO_2 Film on Copper. *International Journal of Electrochemical Science*. **2020**, 6478-6487. doi:10.20964/2020.07.49

[108] Ovchinnikov, S. and Kalashnikov, M. Structure and tribological properties of gradient-layered coatings (Ti, Al, Si, Cr, Mo, S) O, N. *Surface & Coatings Technology 408*, **2021**, 126807.

[109] Quian, H.; Chen, S.; Wang, T.; Cheng, G.; Chen, X.; Xu, Z.; Zeng, Q.; Liu, Y. and Yan, D. Silicon nitride modified enamel coatings enable high thermal shock and corrosion resistances for steel protection. *Surface & Coatings Technology 421*, **2021**.

[110] Zhao, Y.; Dong, S.; Hu, P.; Zhao, Z. and Hong, C. Recent progress in synthesis, growth mechanisms, properties, and application of silicon nitride nanowires. *Ceramics International 47*, **2021**, 14944-14965.

[111] Gao, F.; Lewes-Malandrakis, G.; Wolfer, M.T.; Müller-Sebert, W.; Gentile, P.; Aradilla, D.; Schubert, T. and Nebel, C.E. Diamond-coated silicon wires for supercapacitor applications in ionic liquids. *Diamond & Related Materials 51*, **2015**.

[112] Xu, T.; Tao, Z. and Lozano, P.C. Etching of glass, silicon, and silicon dioxide using negative ionic liquid ion sources. *J. Vac. Sci. Technol. B 36(5)*, **2018**. doi:10.1116/1.5034131.